

PREFACE	<i>Jesús Alberto Toalá Sanz, Martín Antonio Guerrero Roncel, and Guillermo Miguel Garcia-Segura</i>	v
LIST OF PARTICIPANTS		vii
GROUP PHOTOGRAPH		ix
DUST-GAS DYNAMICS AND PLANETESIMAL FORMATION IN PROTO- PLANETARY DISKS	<i>C.-C. Yang</i>	1
VERY MASSIVE STARS IN NGC 3125-A1 ( $Z \sim 0$ ) AND CDFS131717 ( $Z \sim 3$ )	<i>A. Wofford, A. Sixtos, G. Bruzual, S. Charlot, F. Cullen, L. Smith, &amp; S. Hernández</i>	4
STELLAR WINDS FROM MASSIVE STARS	<i>S. J. Arthur</i>	8
MASSIVE STARS HERE AND THERE, ALWAYS WITH SOME IMPACT	<i>Y. Nazé, B. Lim, &amp; G. Rauw</i>	13
WIND-BLOWN NEBULAE FROM MASSIVE STARS	<i>J. Mackey</i>	16
IMPLEMENTATION OF MULTI-ION CHEMICAL KINETICS FOR CIRCUM- STELLAR NEBULAE	<i>A. Mathew &amp; J. Mackey</i>	19
SMALL BUBBLES AROUND BIG STARS	<i>K. Weis</i>	22
MIXED MORPHOLOGY SUPERNOVA REMNANTS AND THE CONTRIBU- TION OF MARGARITA ROSADO TO THE DETECTION OF EXTENDED X-RAY EMISSION FROM SUPERBUBBLES	<i>M. Rosado, J. Reyes-Iturbide, P. Ambrocio-Cruz, L. Arias-Montaña, R. Gabbasov, I. Ramirez-Ballinas, &amp; A. Llamas-Bugarin</i>	25
FEEDBACK FROM MASSIVE STAR WINDS	<i>J. M. Pittard, M. M. Kupilas, C. J. Wareing, &amp; S. A. E. G. Falle</i>	27

## CONTENTS

MULTI-WAVELENGTH OBSERVATIONS OF GALACTIC WINDS <i style="text-align: right;">D. J. Bomans</i>	30
THE INFLUENCE OF STELLAR CLUSTERS ON PAHS: THE POWER OF JOINT HST/JWST OBSERVATIONS IN NEARBY GALAXIES <i style="text-align: right;">D. A. Dale &amp; PHANGS Team</i>	33
PLANETARY NEBULA IN THE BINARY ERA <i style="text-align: right;">G. Garcia-Segura, R. E. Taam, &amp; P. M. Ricker</i>	36
COMMON ENVELOPE SHAPING OF PLANETARY NEBULAE <i style="text-align: right;">S.-J. Rau &amp; P. M. Ricker</i>	39
THE EXTREMELY YOUNG PLANETARY NEBULA M3-27 <i style="text-align: right;">F. Ruiz-Escobedo, M. Peña, &amp; A. V. Beltrán-Sánchez</i>	42
THE DECAM MAGELLANIC CLOUDS EMISSION-LINE SURVEYS <i style="text-align: right;">S. D. Points, K. S. Long, W. P. Blair, P. F. Winkler, R. M. Williams, &amp; Y.-H. Chu</i>	45
SUPERNOVA REMNANT SIGNATURES IN EMISSION-LINE SURVEYS OF THE MAGELLANIC CLOUDS WITH NOIRLAB'S DECAM <i style="text-align: right;">R. N. M. Williams, S. D. Points, K. S. Long, W. P. Blair, &amp; P. F. Winkler</i>	48
DETECTING $\gamma$ -RAYS FROM THE ANCORA SUPERNOVA REMNANT <i style="text-align: right;">C. Burger-Scheidlin, R. Brose, J. Mackey, M. D. Filipović, P. Goswami, E. Mestre Guillen, E. de Oña Wilhelmi, &amp; I. Sushch</i>	51
ACROSS THE TYPE IA SUPERNOVA-VERSE: FROM TYPE IA SUPER- NOVA REMNANTS TO BINARY LOVE STORIES IN THEIR PREVIOUS LIFE <i style="text-align: right;">C.-J. Li &amp; Y.-H. Chu</i>	54
CONFERENCE SUMMARY: STELLAR FEEDBACK IN THE ISM: CELE- BRATING THE LIFE AND WORK OF YOU-HUA CHU <i style="text-align: right;">M.-M. Mac Low</i>	57
AUTHOR INDEX	65

## PREFACE

The meeting “Stellar Feedback in the ISM, Conference Celebrating the life and work of You-Hua Chu” was held on 10th to 14th December 2023 at Ensenada, Baja California, Mexico.

The theme of this conference was to celebrate the lifetime work of You-Hua Chu and her contributions to astronomy. You-Hua’s scientific interests have spanned a broad range of topics in studying the contributions of stellar feedback in various forms to the interstellar medium. Her work with her colleagues, students, and collaborators over the years has spanned the range from studies of young massive stars and their clusters, HII regions and stellar-wind bubbles, to the end of star life in planetary nebulae and supernova remnants, larger interstellar structures, and other drivers of stellar feedback in the Milky Way, the Magellanic Clouds, and galaxies beyond. The goal of this meeting was to bring together collaborators and researchers to present the most recent developments in all of these areas, discuss key questions in the current field, and encourage discussion and collaboration on these questions and possible approaches to address.

Topics covered at this meeting included:

*Young Stars, Star Clusters, and HII Regions.* You-Hua has studied the large star-formation region 30 Doradus in the Large Magellanic Cloud, as well as similar regions, and other drivers of feedback in HII regions. We expanded this topic to finding young stars and defining their properties; links between massive star formation and its molecular environment; the collective input from young star clusters; and dust-gas dynamics in circumstellar disks.

*Massive Stellar-Wind Bubbles.* You-Hua’s work has studied massive stars such as luminous blue variables and Wolf-Rayet stars, and we discussed the impact of these bubbles singularly and collectively. In particular, we discussed both the hot and cool gas in nebulae.

*Stellar Clusters and Superbubbles – Feedback to the ISM.* Much of the modeling of stellar feedback into the interstellar medium includes observations of existing superbubbles. We discussed current observations of such superbubbles; models of superbubble formation and shaping of the regional interstellar medium; and their large-scale input into galactic outflows and winds in high-mass galaxies.

*Planetary Nebulae.* We examined planetary nebulae at all wavelengths. In particular, we examined the hot interiors of planetary nebulae as seen in X-rays.

*Supernova Progenitors and Supernova Remnants.* You-Hua and her collaborators have greatly extended the study of supernova remnants and their progenitors in the Magellanic Clouds, and we reviewed the new in that field. We also discussed the implications of Type Ia Supernova Remnants being shaped by their binary progenitors.

This conference included invited and contributed talks, and poster presentations. A hybrid format was allowed for participants to choose to attend in-person or remotely on a virtual platform. Talk slots were preferentially given to those who attended in person, since this was an event to celebrate with You-Hua Chu. 58 registred astronomers assisted to the meeting, where 40 of them attended in-person. The meeting was open to the staff and students of the Instituto de Astronomía-UNAM, so on average 80 attendees were present during the 4 days of conference. The scientific sessions were held the first four days (11th – 14th December), while the fifth day was an excursion out to the TAOS2 site at the San Pedro Mártir Observatory. The meeting took place in the facilities of the Instituto de Astronomía-UNAM (Ensenada) who partially funded the conference.

## PREFACE

The Scientific Organizing Committee was: Dominik Bomans, Wolfgang Brandner, Rosie Chen, Bryan Dunne, Guillermo García-Segura, Eva Grebel, Martín A. Guerrero, Shin-Ping Lai, Chuan-Jui Li, Mordecai-Mark Mac Low, Yaël Nazé, Sean Points, Kate Su, Jesús Toalá, Rosa Williams, Kerstin Weis, Chao-Chin Yang.

The Local Organizing Committee from Instituto de Astronomía-UNAM (Ensenada) was : Urania Ceseña, Ma. Eugenia García, Teresa García Díaz, Guillermo García-Segura, Carlos Román, Aida Wofford.

Jesús Toalá , Martín A. Guerrero, and Guillermo García-Segura  
Editors of the proceedings

## LIST OF PARTICIPANTS

<b>Jane Arthur</b> , Instituto de Radioastronomía y Astrofísica, UNAM,	México
<b>Dominik Bomans</b> , Astronomical Insitute - Ruhr University Bochum,	Germany
<b>Christopher Burger-Scheidlin</b> , Dublin Institute for Advanced Studies DIAS,	Ireland
<b>Rosie Chen</b> , MPIfR, Bonn,	Germany
<b>You-Hua Chu</b> , ASIAA,	Taiwan
<b>Daniel Dale</b> , U. Wyoming,	USA
<b>Sandino Estrada-Dorado</b> , Instituto de Radioastronomía y Astrofísica, UNAM,	México
<b>Xuan Fang</b> , National Astronomical Observatories, Chinese Academy of Sciences (NAOC),	China
<b>Guillermo Garcia-Segura</b> , Instituto de Astronomía, Ensenada, UNAM,	México
<b>Eva Grebel</b> , Heidelberg University,	Germany
<b>Konstantin Grishunin</b> , Max Planck Institute for Radio Astronomy (MPIfR),	Germany
<b>Martin A. Guerrero</b> , IAA-CSIC,	Spain
<b>Frank Haberl</b> , Max Planck Institute for extraterrestrial Physics,	Germany
<b>Palmira Jimenez Hernandez</b> , Dublin Institute for Advanced Studies,	Ireland
<b>Sungeun Kim</b> , Sejong University, Department of Physics and Astronomy,	Korea
<b>Shih-Ping Lai</b> , National Tsing Hua University,	Taiwan
<b>Chuan-Jui Li</b> , ASIAA,	Taiwan
<b>Knox Long</b> , STScI,	USA
<b>Leslie Looney</b> , University of Illinois,	USA
<b>Alejandra Zaavik Lugo Aranda</b> , Instituto de Astronomía, UNAM,	México
<b>Mordecai-Mark Mac Low</b> , American Museum of Natural History,	USA
<b>Jonathan Mackey</b> , Dublin Institute for Advanced Studies,	Ireland
<b>Raul Felipe Maldonado</b> , Instituto de Radioastronomía y Astrofísica,	México
<b>Daniel Maschmann</b> , Steward Observatory,	USA
<b>Arun Mathew</b> , Dublin Institute for Advanced Studies,	Ireland
<b>Shazrene Mohamed</b> , University of Virginia,	USA
<b>Borja Montoro-Molina</b> , IAA-CSIC,	Spain
<b>Yael Naze</b> , FNRS/ULiege,	Belgique
<b>Sally Oey</b> , University of Michigan,	USA
<b>Alejandro Olvera</b> , Arizona State University,	USA
<b>Rogelio Orozco</b> , Instituto de Astronomía, UNAM,	México
<b>Kuo-Chuan Pan</b> , National Tsing Hua University,	Taiwan
<b>Julian Pittard</b> , The University of Leeds,	UK
<b>Sean Points</b> , CTIO/NOIRLab,	USA
<b>Jesús Toalá</b> , Instituto de Radioastronomía y Astrofísica,	México
<b>Shiau-Jie Rau</b> , University of Illinois at Urbana-Champaign,	USA
<b>Michael Richer</b> , Instituto de Astronomía, UNAM,	México
<b>Paul Ricker</b> , University of Illinois,	USA
<b>Janis Rodríguez</b> , Instituto de Radioastronomía y Astrofísica,	México
<b>Jennifer Rodríguez</b> , The Ohio State University,	USA

## LIST OF PARTICIPANTS

<b>Jimena Rodriguez</b> , University of Arizona,	USA
<b>Francisco Ruiz-Escobedo</b> , Instituto de Astronomía, UNAM,	México
<b>Sebastian Sanchez</b> , Instituto de Astronomía, UNAM,	México
<b>Edgar Santamaría</b> , Instituto de Radioastronomía y Astrofísica,	México
<b>Manami Sasaki</b> , Friedrich-Alexander-University Erlangen-Nürnberg,	Germany
<b>Dominique Segura-Cox</b> , The University of Texas at Austin,	USA
<b>Ekta Sharma</b> , National Astronomical Observatories of China, Beijing,	China
<b>Linda Smith</b> , Space Telescope Science Institute,	USA
<b>Ian Stephens</b> , Worcester State University,	USA
<b>Kate Su</b> , University of Arizona,	USA
<b>Enrique Vázquez-Semadeni</b> , Instituto de Radioastronomía y Astrofísica,	México
<b>Daniel Wang</b> , University of Massachusetts,	USA
<b>Kerstin Weis</b> , Astronomical Institute - Ruhr University Bochum,	Germany
<b>Rosa Williams</b> , Columbus State University,	USA
<b>Aida Wofford</b> , Instituto de Astronomía, UNAM,	México
<b>Chao-Chin Yang</b> , The University of Alabama,	USA
<b>Hsiang-Yi Karen Yang</b> , National Tsing Hua University,	Taiwan
<b>Jian-wen Zhou</b> , Max-Planck-Institut für Radioastronomie,	Germany

GROUP PHOTOGRAPH



Stellar Feedback in the ISM. Conference Celebrating the life and work of You-Hua Chu (December 11-14, 2023)  
Editors: Jesús Tolá, Martín A. Guerrero, and Guillermo M. García-Segura

## DUST-GAS DYNAMICS AND PLANETESIMAL FORMATION IN PROTOPLANETARY DISKS

Chao-Chin Yang<sup>1</sup>

### RESUMEN

Aunque se han detectado miles de sistemas planetarios extrasolares, aún queda por trazar un panorama completo de cómo se forman los planetas a partir de sus discos protoplanetarios natales. Una de las etapas más desafiantes es la formación de planetesimales a escala kilométrica a partir de partículas de polvo de tamaño centimétrico o milimétrico en el disco. Estas partículas sufren de derivas internas problemáticamente rápidas y de una baja eficiencia de adherencia debido a la fragmentación y el rebote en las colisiones. Este artículo revisa brevemente nuestro conocimiento actual de la dinámica del polvo y el gas en los discos protoplanetarios y sus consecuencias en la formación de planetesimales. Específicamente, se examina cómo y bajo qué condiciones las partículas de polvo pueden concentrarse activamente a una alta densidad para que se formen planetesimales, la función de masa inicial de los planetesimales y los efectos de la turbulencia.

### ABSTRACT

Even though thousands of extrasolar planetary systems have been detected, a comprehensive picture of how planets are formed from their natal protoplanetary disks remains to be drawn. One of the most challenging stages is the formation of kilometer-scale planetesimals from centi-/milli-meter-sized dust particles in the disk. These particles suffer from problematically rapid inward drifts and poor sticking efficiencies due to fragmentation and bouncing at collisions. This article briefly reviews our current understanding of the dust-gas dynamics in protoplanetary disks and its consequences on planetesimal formation. Specifically, how and under what conditions dust particles can actively concentrate themselves to high density for planetesimals to form, the initial mass function of planetesimals, and the effects of turbulence are examined.

*Key Words:* Hydrodynamics — Instabilities — Magnetohydrodynamics (MHD) — Planets and Satellites: Formation — Protoplanetary Disks — Turbulence

### 1. INTRODUCTION

As of this writing, more than 5,600 extrasolar planets have been detected outside of our own Solar System.<sup>2</sup> Statistically speaking, for about every ten and two Sun-like stars, one should find one giant planet and one Earth-sized planet, respectively (Winn & Fabrycky 2015). This ubiquity of extrasolar planets implies that planet formation should readily proceed around young stellar objects. However, a comprehensive theoretical picture of how planets are formed from their natal protoplanetary disks (a.k.a. circumstellar disks) remains to be drawn. From interstellar dust grains to newborn planets, planet formation spans 30 orders of magnitude in mass and 13 orders of magnitude in size. It involves intricate interactions between the solid materials, the gaseous medium, the stellar ir-

radiation, and the magnetic field, resulting in complicated dynamics in protoplanetary disks (see, e.g., Lesur et al. 2023, and references therein).

In the core accretion scenario of planet formation, dust coagulation proceeds via mutual collisions and electrostatic forces, but the maximum size this process can reach is limited by two physical barriers. First, a natural negative radial pressure gradient in the gaseous disk exists, so the gas moves around the central star at a slightly slower speed than Keplerian. On the other hand, the dust particles move at the Keplerian speed and hence experience constant headwind from the gas drag. As the dust particles grow, this results in their radial drift towards the central star in a significantly short timescale compared with the disk lifetime (Adachi, Hayashi, & Nakazawa 1976; Weidenschilling 1977; Youdin 2010). Second, dust particles may not necessarily stick at collisions; they may fragment each other at high collision speeds or just bounce off each other at moderate speeds (e.g., Zsom et al. 2010). In general, dust growth is limited by fragmentation or bouncing bar-

<sup>1</sup>Department of Physics and Astronomy, The University of Alabama, Box 870324, Tuscaloosa, AL 35487-0324, U.S.A. (ccyang@ua.edu).

<sup>2</sup>For the latest census, see, e.g., <https://science.nasa.gov/exoplanets/discoveries-dashboard/>.

rier in the inner region ( $\lesssim 10$  au) of the disk and by radial-drift barrier in the outer region ( $\gtrsim 10$  au) (e.g., Birnstiel, Fang, & Johansen 2016).

These barriers pose a stringent obstacle to the formation of kilometer-sized planetesimals. Numerous mechanisms have been proposed to overcome these barriers, and most of which center around the potential to drive local concentration of solid materials to high density such that planetesimals can form via direct gravitational collapse. In this concise review, we focus on one such mechanism, the so-called “streaming instability”, which became popular as it is the only mechanism that the dust particles can actively assist themselves to concentrate, instead of passively relying on the gas dynamics.

## 2. THE STREAMING INSTABILITY

The streaming instability was originally discovered as a linear instability (Youdin & Goodman 2005). The essential ingredient for this instability is the back reaction of the dust particles to the gas drag, albeit the solid abundance is small at the percentage level. As a linear instability, small perturbations exponentially amplify with time, and these perturbations must saturate nonlinearly into some kind of turbulent or stochastic flow (Johansen & Youdin 2007). The local dust density concentration in this saturation state does not appear to be sufficiently high to trigger gravitational collapse. Instead, this state induces turbulent diffusion which should balance vertical sedimentation of the dust particles to maintain a finite thickness of the dust layer (Yang & Zhu 2021; Baronett, Yang, & Zhu 2024).

To trigger gravitational collapse to form planetesimals within a sedimented layer of dust particles, sufficiently high solid loading is required. When the dust layer has a solid abundance  $Z$ —defined as the dust-to-gas *column* density ratio  $\Sigma_d/\Sigma_g$ —above a certain threshold  $Z_c$ , strong radial concentration of dust particles appear in the mid-plane of the disk (Johansen, Youdin, & Mac Low 2009), forming roughly axisymmetric, dense dusty filaments (Yang & Johansen 2014). The process could be interpreted as traffic jams, as a local clump of dust particles drifts radially at a slower rate than isolated particles, secularly accretes these particles from upstream, and hence the drift speed of the clump is further reduced. Depending on the size of the particles,  $Z_c$  appears to be on the order of 1% (Yang, Johansen, & Carrera 2017; Li & Youdin 2021). Moreover, the higher the solid abundance  $Z$  above  $Z_c$ , the smaller the radial separations between adjacent dusty filaments are (Yang & Johansen 2014; Yang, Johansen, & Carrera 2017; Yang, Mac Low, & Johansen 2018).

Naively, hydrodynamical or MHD turbulence already operating in the gaseous disk should inhibit dust particles from concentrating and hence forming planetesimals. However, this effect does not appear to be as strong as one expects. Yang et al. (2018) conducted the first non-ideal MHD simulations of this kind, focusing on a layered accretion disk model dominated by Ohmic diffusion, and found that  $Z \sim 2\%$  is sufficient to trigger strong concentrations of solids. Similar results were found by Xu & Bai (2022) with a non-ideal MHD disk model regulated by ambipolar diffusion. The hydrodynamical turbulence driven by vertical shear instability (VSI) could even trigger more concentrations of solids than without VSI (Schäfer, Johansen, & Banerjee 2020; Schäfer & Johansen 2022). In all these models, the dust layers are significantly thicker than those supported by pure streaming turbulence, while the critical solid abundance  $Z_c$  does not appear to be proportionately increased. This indicates that the conventional criterion of the local dust-to-gas *volume* density ratio  $\rho_d/\rho_g \gtrsim 1$  for planetesimal formation may not be an accurate one (see also Li & Youdin 2021).

## 3. PLANETESIMAL FORMATION

As described above, the back reaction of the dust particles in the mid-plane of the disk creates traffic jams to concentrate the particles to high density. As soon as the density reaches above the Hill density, numerous local clumps of particles in the dense dusty filaments should gravitationally collapse into planetesimals (Johansen et al. 2015; Simon et al. 2016). With high-resolution computer simulations, the number of collapsed clumps is large enough such that the resulting mass function of planetesimals has become statistically meaningful. It is generally observed that the mass function is top-heavy to the extent the majority of the total mass is shared by a few large planetesimals, while the less massive the planetesimals, the more numerous they are.

Continuing the simulation model of the largest local shearing box at the time by Yang & Johansen (2014), Schäfer, Yang, & Johansen (2017) conducted simulations of planetesimal formation and analyzed the mass distribution of the newborn planetesimals. It appears that the high-mass end of the cumulative distribution is not a sharp cutoff, but a shallower exponential taper (see also Li, Youdin, & Simon 2019). The mass where this taper occurs determines the characteristic mass of planetesimals, which was found to be correlated with the mass reservoir in the dusty filaments. This shallow exponential taper was

nicely reproduced by Kavelaars et al. (2021) using a meta-analysis of the observed cold classical Kuiper Belt objects—which are believed to be the least disturbed left-over planetesimals from the formation of the Solar System.

Moreover, it appears that the characteristic mass of the collapsed products could reach sub-earth masses in the outer regions ( $\gtrsim 20$  au) of some systems. One is in a turbulent disk driven by gravitational instability when the disk is still young and massive (Baehr, Zhu, & Yang 2022). Another is in a large-scale gaseous vortex, which naturally traps and concentrates dust particles (Lyra et al. 2024). If any of these processes proves to be robust, the theoretical timescale for planet formation could be significantly shortened and better meet the constraint of a typical disk lifetime of a few million years inferred from observations (see, e.g., Williams & Cieza 2011).

As a final remark, how a distribution of dust particles of different sizes participate in the formation of planetesimals has generated quite some interests in recent years. Below the radial-drift barrier, the smaller a dust particle, the more tightly coupled to the gas it is (see, e.g., Weidenschilling 1977). This results in increasing mobility of dust particles of increasing sizes in streaming turbulence and hence the largest particles tend to be found in regions with high total dust density while being depleted in regions with low total dust density (Yang & Zhu 2021). Therefore, it is implied that the composition of a newborn planetesimal should be significantly more contributed by the largest dust particles. Indeed, this implication has been recently found in computer simulations by Cañas et al. (2024).

#### 4. SUMMARY

In summary, planetesimal formation suffers from radial-drift and fragmentation/bouncing barriers. To overcome these barriers, dust particles can actively help themselves concentrate to high densities via the back reaction of the drag force to the gas. The criterion for planetesimal formation depends on the solid abundance ( $> O(1\%)$ ), the particle size, the radial pressure gradient, and perhaps the gas turbulence. The initial mass function of planetesimals is top-heavy and shows a characteristic exponential cut-off at high-mass end. The composition of plan-

etesimals may be predominantly contributed by those of the largest dust particles.

#### REFERENCES

- Adachi, I., Hayashi, C., & Nakazawa, K. 1976, *PThPh*, 56, 1756
- Baehr, H., Zhu, Z., & Yang, C.-C. 2022, *ApJ*, 933, 100
- Baronett, S. A., Yang, C.-C., & Zhu, Z. 2024, *MNRAS*, 529, 275
- Birnstiel, T., Fang, M., & Johansen, A. 2016, *SSRv*, 205, 41
- Cañas, M. H., Lyra, W., Carrera, D., Krapp, L., Sengupta, D., Simon, J. B., Umurhan, O. M., Yang, C.-C., & Youdin, A. N. 2024, *PSJ*, 5, 55
- Johansen, A., Mac Low, M.-M., Lacerda, P., & Bizzarro, M. 2015, *Science Advances*, 1, 1500109
- Johansen, A. & Youdin, A. 2007, *ApJ*, 662, 627
- Johansen, A., Youdin, A., & Mac Low, M.-M. 2009, *ApJ*, 704, L75
- Kavelaars, J. J., Petit, J.-M., Gladman, B., et al. 2021, *ApJ*, 920, L28
- Lesur, G., Flock, M., Ercolano, B., et al. 2023, in *Protostars and Planets VII*, ed. S.-i. Inutsuka, Y. Aikawa, T. Muto, K. Tomida, & M. Tamura. ASP Conference Series, Vol. 534 (San Francisco: Astronomical Society of the Pacific), p. 465
- Li, R. & Youdin, A. N. 2021, *ApJ*, 919, 107
- Li, R., Youdin, A. N., & Simon, J. B. 2019, *ApJ*, 885, 69
- Lyra, W., Yang, C.-C., Simon, J. B., Umurhan, O. M., & Youdin, A. N. 2024, *ApJ*, in press
- Schäfer, U. & Johansen, A. 2022, *A&A*, 666, A98
- Schäfer, U., Johansen, A., & Banerjee, R. 2020, *A&A*, 635, A190
- Schäfer, U., Yang, C.-C., & Johansen, A. 2017, *A&A*, 597, A69
- Simon, J. B., Armitage, P. J., Li, R., & Youdin, A. N. 2016, *ApJ*, 822, 55
- Weidenschilling, S. J. 1977, *MNRAS*, 180, 57
- Williams, J. P. & Cieza, L. A. 2011, *ARA&A*, 49, 67
- Winn, J. N. & Fabrycky, D. C. 2015, *ARA&A*, 53, 409
- Xu, Z. & Bai, X.-N. 2022, *ApJ*, 924, 3
- Yang, C.-C. & Johansen, A. 2014, *ApJ*, 792, 86
- Yang, C.-C., Johansen, A., & Carrera, D. 2017, *A&A*, 606, A80
- Yang, C.-C., Mac Low, M.-M., & Johansen, A. 2018, *ApJ*, 868, 27
- Yang, C.-C. & Zhu, Z. 2021, *MNRAS*, 508, 5538
- Youdin, A. N. 2010, in *Physics and Astrophysics of Planetary Systems*, ed. T. Montmerle, D. Ehrenreich & A. M. Lagrange. EAS Publications Series, Vol. 41 (Les Ulis Cedex: EDP Sciences), p. 187
- Youdin, A. N. & Goodman, J. 2005, *ApJ*, 620, 459
- Zsom, A., Ormel, C. W., Güttler, C., Blum, J., & Dullemond, C. P. 2010, *A&A*, 513, A57

## VERY MASSIVE STARS IN NGC 3125-A1 ( $Z \sim 0$ ) AND CDFS131717 ( $Z \sim 3$ )

A. Wofford<sup>1</sup>, A. Sixtos<sup>1</sup>, G. Bruzual<sup>2</sup>, S. Charlot<sup>3</sup>, F. Cullen<sup>4</sup>, L. Smith<sup>5</sup>, and S. Hernández<sup>6</sup>

### RESUMEN

La masa máxima que puede poseer una estrella es desconocida. Revisamos algo de lo que se sabe actualmente sobre las estrellas más masivas del Universo cercano. En particular, presentamos evidencia de estrellas con masas ZAMS por encima del límite superior de masa canónico ( $\sim 150 M_{\odot}$ ) en la galaxia de brotes de formación estelar cercana, NGC 3125, y la galaxia de mediodía cósmico, CDFS131717. En ambos casos, la evidencia se basa en espectroscopia UV en el marco de reposo, donde estas estrellas tienen las principales líneas de diagnóstico: O V  $\lambda 1371$ , N IV]  $\lambda 1468$ , He II  $\lambda 1640$ , and N IV  $\lambda 1720$ . El reciente descubrimiento de estrellas similares en nueve galaxias de mediodía cósmico resalta la importancia de continuar los estudios de estas estrellas en galaxias cercanas, donde se pueden obtener vistas detalladas sobre las condiciones favorables para su presencia, retroalimentación y destinos.

### ABSTRACT

The maximum mass that a star can possess is unknown. We review some of what is currently known about the most massive stars in the nearby Universe. In particular, we present evidence for stars with ZAMS masses above the canonical upper mass limit ( $\sim 150 M_{\odot}$ ) in nearby starburst galaxy, NGC 3125, and cosmic-noon galaxy, CDFS131717. In both cases, the evidence is based on rest-frame UV spectroscopy, where these stars have the main diagnostic lines: O V  $\lambda 1371$ , N IV]  $\lambda 1468$ , He II  $\lambda 1640$ , and N IV  $\lambda 1720$ . The recent discovery of similar stars in nine cosmic-noon galaxies highlights the importance of pursuing studies of these stars in nearby galaxies, where one can obtain details views about conditions favorable to their presence, feedback and fates.

*Key Words:* galaxies: starburst — techniques: spectroscopic — ultraviolet: galaxies — ultraviolet: stars

### 1. INTRODUCTION

Massive ( $\geq 8 M_{\odot}$ ) stars define the upper limits of the star formation process, dominate the energetics of their local environments, and significantly affect the chemical evolution of galaxies. Their role in starburst galaxies and the early Universe is likely to be important, but we still don't know the maximum mass that a star can possess. Stars with masses significantly above the “canonical” upper limit of e.g. the Galactic Center (Figer 2005), i.e., with  $\gg 150 M_{\odot}$ , are known as Very Massive Stars (VMS; Vink 2015). By re-analyzing the most massive hydrogen-

and-nitrogen rich Wolf-Rayet (WNh) stars in the center of R136, which is the main ionizing cluster of the Tarantula Nebula in the Large Magellanic Cloud (LMC), Crowther et al. (2010) found that stars originally assumed to be below  $150 M_{\odot}$  were actually more luminous and massive, i.e., VMS. VMS R136a1 is the most massive star known to date. According to multiple mass determinations (Crowther et al. 2010; Bestenlehner et al. 2020; Brands et al. 2022; Kalari et al. 2022) its initial mass is  $\geq 200 M_{\odot}$ . In addition, it is putatively single. This is based on multi-epoch spectroscopy showing the absence of a radial velocity shift in excess of 50 km/s. Such an excess would indicative the presence of a close companion star (Shenar et al. 2023). Two other VMS in R136 are also putatively single according to this criterion (Shenar et al. 2023). Another indication that the latter three VMS in R136 are very massive is that they show strong broad He II  $\lambda 1640$  emission that can be modeled by formation in the wind of a very luminous (and massive) star that approaches the Eddington limit (Vink et al. 2011), where the force of radiation balances that of gravity. If R136a1 was composed of 10 main sequence stars of  $\sim 20 M_{\odot}$  instead of a single  $200 M_{\odot}$  star,

<sup>1</sup>Instituto de Astronomía, Universidad Nacional Autónoma de México, Unidad Académica en Ensenada, Km 103 Carr. Tijuana–Ensenada, Ensenada, B.C., C.P. 22860 México (awofford@astro.unam.mx).

<sup>2</sup>Centro de Radioastronomía y Astrofísica, UNAM, Campus Morelia, Apartado Postal 3–72, 58090, Morelia, Michoacán, México.

<sup>3</sup>Sorbonne Université, CNRS, UMR 7095, Institut d’Astrophysique de Paris, 98 bis bd Arago, 75014 Paris, France.

<sup>4</sup>Institute for Astronomy, University of Edinburgh, Royal Observatory, Edinburgh, EH9 3HJ, UK.

<sup>5</sup>Space Telescope Science Institute, 3700 San Martin Drive, Baltimore, MD 21218, USA.

<sup>6</sup>AURA for ESA, Space Telescope Science Institute, 3700 San Martin Drive, Baltimore, MD 21218, USA.

it would show He II absorption, but it doesn't. Unfortunately, the formation mechanism(s), evolutionary path(s) and fate(s) of VMS are poorly known. This is a problem for understanding their role in the Universe. However, one can obtain clues about the environments that are favorable to their presence by considering the properties of R136. This dense cluster is 2 – 2.5 Myr old (Brands et al. 2022); has a binary-corrected virial mass of  $4.6 - 14.2 \times 10^4 M_{\odot}$  (Hénault-Brunet et al. 2012) that is consistent with its photometric mass ( $\sim 5 \times 10^4 M_{\odot}$ , Andersen et al. 2009); and has an ionized-gas oxygen abundance of  $12+\log(\text{O}/\text{H})=8.39\pm 0.01$  (Domínguez-Guzmán et al. 2022). This is half of the solar reference value, where  $12+\log(\text{O}/\text{H})_{\odot}=8.69\pm 0.05$  (Asplund et al. 2009). The R136 cluster is massive and considered to be strongly star-forming. It thus qualifies as a mini-starburst.

Beyond the Local Group, due to distance, VMS located in the centers of clusters like R136 cannot be resolved individually. In the rest-frame UV, VMS have spectral signatures that are similar to those of classical Wolf-Rayet (cWR) stars, which are the core He-burning descendants of stars with  $\gtrsim 25 M_{\odot}$  (Crowther 2007). In particular, both types of stars produce strong P-Cygni like profiles of N V  $\lambda\lambda 1239, 1243$  and C IV  $\lambda\lambda 1548, 1551$ , as well as strong broad (FWHM  $\sim 1000$  km/s) He  $\lambda 1640$  emission. By analyzing the UV spectrum of R136, Crowther et al. (2016) found that seven VMS dominate its integrated He II  $\lambda 1640$  emission. In addition, Crowther & Castro (2024) analyzed a more extended 30 pc x 30 pc region of NGC 2070, which is the dominant giant H II region of the Tarantula nebula and includes R136. The individual stars in the extended region have ages between 1 and 7 Myr. Crowther & Castro (2024) found that a combination of classical Wolf-Rayet (cWR) and main sequence WNh + transition Of/WN stars (including VMS), dominate the He II  $\lambda 1640$  emission. cWR stars appear in a single stellar population at  $\sim 3 - 4$  Myr, i.e., after the VMS WNh stars. Because VMS are very short lived ( $< 2.5$  Myr, e.g., Wofford et al. 2023) signatures of their presence are indicative of a very young massive star region.

In a recent compilation, Martins et al. (2023) use a combination of UV + optical criteria to establish that a region is VMS-dominated. These are: presence of broad (FWHM  $\approx 1000$  km/s) and strong (equivalent width,  $EW \gtrsim 3 \text{ \AA}$ ) He II  $\lambda 1640$  emission, and weak or absent red bump at  $\sim 5801 - 12 \text{ \AA}$ , as the latter is produced by carbon-rich cWR stars. According to these criteria, Martins et al. found that in nearby galaxies beyond the Lo-

cal Group, only two galaxies, J1129+2034/SB179 ( $12+\log(\text{O}/\text{H})=8.29$ , Senchyna et al. 2021) and J1200+1343 ( $12+\log(\text{O}/\text{H})=8.26$ , Berg et al. 2022), have VMS-dominated clusters (considering known galaxies with UV spectra). In addition, they classify two regions as having VMS and/or cWR: NGC 3125-A1 ( $12 + \log(\text{O}/\text{H}) = 8.32$  (Wofford et al. 2023; hereafter, W23) and a region in J1215+2038/SB191 ( $12+\log(\text{O}/\text{H})=8.30$  (Senchyna et al. 2017). According to other authors, VMS candidates are present in two additional nearby galaxies: NGC 5253 (cluster 5;  $12+\log(\text{O}/\text{H})=8.26$ , Smith et al. 2016 and Mrk 71 ( $12+\log(\text{O}/\text{H}) = 7.89$ , Smith et al. 2023). Excitingly, there have been several claims of detections of VMS at much larger distances ( $z = 2 - 3$ ), i.e., during the epoch when galaxies present a peak in their star formation rate density (Koushan et al. 2021), which is known as cosmic noon. Upadhyaya et al. (2024) show that in addition to strong broad He II emission, VMS-dominated regions also show strong broad emission lines of N IV]  $\lambda 1486$  and N IV  $\lambda 1720$ . Finally, O V  $\lambda 1371$  blue-shifted absorption has also been proposed as an indicator of the possible presence of VMS (Wofford et al. 2014, 2023). Other stars that show O V  $\lambda 1371$  are O-type and carbon-rich WR stars (WC; Martins & Palacios 2022). However, if WC stars dominate the O V absorption, then the so-called red bump at  $\sim 5801 - 12 \text{ \AA}$  will be strong in the optical (Martins et al. 2023).

In § 2 and § 3, we discuss the evidence for VMS found in NGC 3125 and CDFS131717, respectively. In § 4, we provide our conclusions.

## 2. NGC 3125-A1

Super star cluster (SSC) A1 ( $3.1 \times 10^5 M_{\odot}$ ) in NGC 3125 has one of the strongest ( $EW = 4.6 \pm 0.5 \text{ \AA}$ ) broad ( $FWHM = 1131 \pm 40 \text{ km s}^{-1}$ ) He II  $\lambda 1640$  emission lines in the nearby Universe and constitutes an important template for interpreting observations of extreme He II emitters out to redshifts of  $z \sim 2 - 3$  (W23). In W23, we present observations of A1 obtained with the Cosmic Origins Spectrograph (COS) on board of the *HST*, using gratings G130M (PI Leitherer, PID 12172) and G160M (PI Wofford, PID 15828). Figure 1 shows an *HST* image of NGC 3125 with the COS aperture overlaid and A1's position indicated. In W23, we show that there is no significant contamination of the He II line with nebular emission and that the line is redshifted by  $121 \pm 17 \text{ km s}^{-1}$  relative to ISM lines. In addition, we compare the COS observations of A1 to recent single-star Charlot & Bruzual (CB19, Plat et al. 2019) simple stellar population (SSP) models with VMS of up

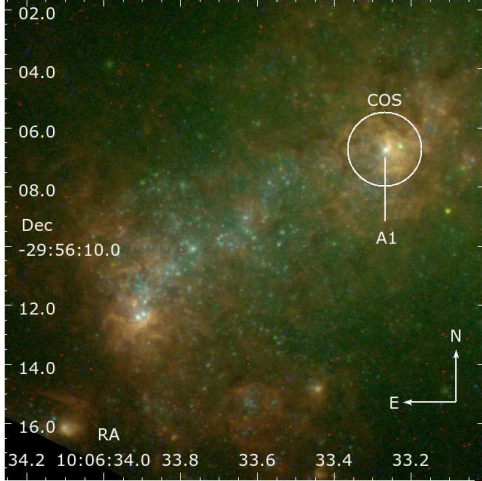


Fig. 1. HST ACS HRC composite image (R: F658N, G: F555W, B: F330W; PI Chandar, PID 10400) of NGC 3125 with  $2.5''$  COS aperture overlaid. We indicate the position of SSC A1. At a distance of  $\approx 14.84$  Mpc (Mould et al. 2000), the COS aperture spans a projected distance of  $\approx 179.27$  pc.

to  $300 M_{\odot}$ . We find that a model with  $Z = 0.008$ , age = 2.2 Myr, and VMS approaching the Eddington limit provides an excellent fit to the He II emission and fits reasonably well N V  $\lambda\lambda 1238, 1241$ , N IV]  $\lambda 1486$ , C IV  $\lambda\lambda 1548, 1551$ , and N IV  $\lambda 1720$ . This can be seen in Figure 2.

In W23, we also show that BPASS version 2.3 models with close binaries (Byrne et al. 2022) currently fail to reproduce strong stellar He II emission. However, it is clear that population synthesis models should allow for close binary evolution (Sana et al. 2012). Finally, W23 present O V  $\lambda 1371$  line-profile predictions showing that this line constitutes an important tracer of youth and VMS in galaxies. O V is also seen in O-type and WC stars.

### 3. CDFS131717

Broad He II  $\lambda 1640$  emission is the strongest stellar line in the stacked UV spectrum of 811 Lyman Break Galaxies (LBGs) located at  $z \sim 3$  produced by Shapley et al. (2003). Lyman Break Galaxies are star-forming galaxies that are selected using their differing appearance in several imaging filters due to the position of the Lyman limit. In stacked spectra, the uncertainties in the redshifts of the galaxies that make up the spectrum contribute to some extent to the width of the composite He II line profile. However, a recent deep (20 hr) observation of a UV bright ( $M_{UV} = -21.7$ ) non-lensed star-forming galaxy (ID = CDFS131717) that is located at  $z_{\text{spec}} = 3.071$  and is part of the deep public ESO spectroscopic survey

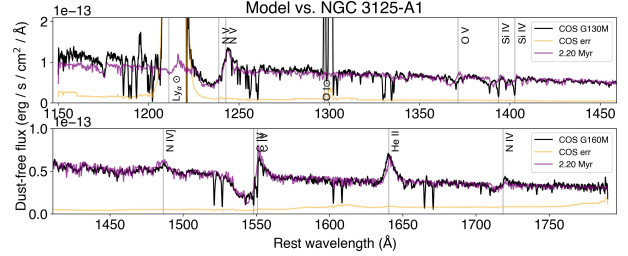


Fig. 2. Comparison of HST COS G130M (top) + G160M (bottom) UV spectrum of NGC 3125-A1 with best-fit  $Z = 0.008$  CB19 model accounting for VMS (black and purple curves, respectively). We indicate the positions of relevant stellar and geocoronal lines.

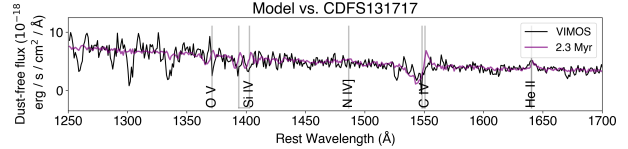


Fig. 3. Comparison of VLT VANDELS spectrum with model accounting for VMS. (black and purple curves, respectively). We indicate the positions of relevant stellar lines.

with VIMOS on the *Very Large Telescope (VLT)*, VANDELS (McLure et al. 2018; Garilli et al. 2021), clearly shows the existence of broad He II 1640 emission in single objects (Stanton et al., in prep.). In Figure 3, we show the rest-frame UV spectrum of CDFS131717 with a  $Z = 0.006$  model accounting for VMS overlaid (see W23 for more details). Given the simultaneous tentative detection of O V  $\lambda 1371$ , this cosmic-noon galaxy could contain a mix of VMS and cWR. As previously mentioned, nine other VMS-dominated candidates are reported in (Upadhyaya et al. 2024), highlighting the importance of accounting for VMS in population synthesis models and the need for further nearby spatially-resolved studies of VMS-dominated stellar populations, so that we can learn about the environments that are favorable to their formation, effects of their feedback, and also their fates.

### 4. CONCLUSIONS

In conclusion, population synthesis models should include binaries, VMS, modern mass-loss prescriptions, and rotational mixing. Our results show the effect of the improved formulation of stellar mass loss rates.

### REFERENCES

- Andersen, M., Zinnecker, H., Moneti, A., et al. 2009, *ApJ*, 707, 1347  
 Asplund, M., Grevesse, N., Sauval, A. J., & Scott, P. 2009, *ARA&A*, 47, 481

- Berg, D. A., James, B. L., King, T., et al. 2022, *ApJS*, 261, 31
- Bestenlehner, J. M., Crowther, P. A., Caballero-Nieves, S. M., et al. 2020, *MNRAS*, 499, 1918
- Brands, S. A., de Koter, A., Bestenlehner, J. M., et al. 2022, *A&A*, 663, A36
- Byrne, C. M., Stanway, E. R., Eldridge, J. J., McSwiney, L., & Townsend, O. T. 2022, *MNRAS*, 512, 5329
- Crowther, P. A. 2007, *ARA&A*, 45, 177
- Crowther, P. A., Caballero-Nieves, S. M., Bostroem, K. A., et al. 2016, *MNRAS*, 458, 624
- Crowther, P. A. & Castro, N. 2024, *MNRAS*, 527, 9023
- Crowther, P. A., Schnurr, O., Hirschi, R., et al. 2010, *MNRAS*, 408, 731
- Domínguez-Guzmán, G., Rodríguez, M., García-Rojas, J., Esteban, C., & Toribio San Cipriano, L. 2022, *MNRAS*, 517, 4497
- Figer, D. F. *Astrophysics and Space Science Library*, Vol. 327, *The Initial Mass Function 50 Years Later*, ed. E. Corbelli, F. Palla & H. Zinnecker, 89
- Garilli, B., McLure, R., Pentericci, L., et al. 2021, *A&A*, 647, A150
- Hénault-Brunet, V., Evans, C. J., Sana, H., et al. 2012, *A&A*, 546, A73
- Kalari, V. M., Horch, E. P., Salinas, R., et al. 2022, *ApJ*, 935, 162
- Koushan, S., Driver, S. P., Bellstedt, S., et al. 2021, *MNRAS*, 503, 2033
- Martins, F. & Palacios, A. 2022, *A&A*, 659, A163
- Martins, F., Schaerer, D., Marques-Chaves, R., & Upadhyaya, A. 2023, *A&A*, 678, A159
- McLure, R. J., Pentericci, L., Cimatti, A., et al. 2018, *MNRAS*, 479, 25
- Mould, J. R., Huchra, J. P., Freedman, W. L., et al. 2000, *ApJ*, 529, 786
- Plat, A., Charlot, S., Bruzual, G., et al. 2019, *MNRAS*, 490, 978
- Sana, H., de Mink, S. E., de Koter, A., et al. 2012, *Science*, 337, 444
- Senchyna, P., Stark, D. P., Charlot, S., et al. 2021, *MNRAS*, 503, 6112
- Senchyna, P., Stark, D. P., Vidal-García, A., et al. 2017, *MNRAS*, 472, 2608
- Shapley, A. E., Steidel, C. C., Pettini, M., & Adelberger, K. L. 2003, *ApJ*, 588, 65
- Shenar, T., Sana, H., Crowther, P. A., et al. 2023, *A&A*, 679, A36
- Smith, L. J., Crowther, P. A., Calzetti, D., & Sidoli, F. 2016, *ApJ*, 823, 38
- Smith, L. J., Oey, M. S., Hernandez, S., et al. 2023, *ApJ*, 958, 194
- Upadhyaya, A., Marques-Chaves, R., Schaerer, D., et al. 2024, arXiv e-prints, arXiv:2401.16165
- Vink, J. S., ed. 2015, *Astrophysics and Space Science Library*, Vol. 412, *Very Massive Stars in the Local Universe*
- Vink, J. S., Muijres, L. E., Anthonisse, B., et al. 2011, *A&A*, 531, A132
- Wofford, A., Leitherer, C., Chandar, R., & Bouret, J.-C. 2014, *ApJ*, 781, 122
- Wofford, A., Sixtos, A., Charlot, S., et al. 2023, *MNRAS*, 523, 3949

## STELLAR WINDS FROM MASSIVE STARS

S. J. Arthur<sup>1</sup>

### RESUMEN

Los vientos estelares de estrellas masivas son importantes para la retroalimentación de energía y momento, así como el enriquecimiento químico del medio interestelar. Observaciones a multifrecuencias de junto con simulaciones numéricas en 2 y 3 dimensiones han contribuido a nuestro entendimiento de la interacción de los vientos estelares con sus entornos. En este artículo, examino los avances recientes en los vientos de estrellas de la secuencia principal, choques de proa y vientos de etapas evolucionadas de estrellas masivas.

### ABSTRACT

Stellar winds from massive stars are important for feedback of energy and momentum, as well as chemical enrichment of the interstellar medium. Multiwavelength observations together with numerical simulations in 2 and 3 dimensions have contributed to our understanding of the interaction of stellar winds with their environment. In this review, I examine recent progress on stellar winds from main-sequence stars, bow shocks and winds from evolved stages of massive stars.

*Key Words:* circumstellar matter — H II regions — ISM: bubbles — stars: mass loss — stars: winds, outflows

### 1. INTRODUCTION

For stars with initial masses above  $15M_{\odot}$ , mass loss through stellar winds is important at every stage of their evolution. On the main sequence, hot O or early B stars drive fast winds through momentum transfer from UV photons to metal ion lines in the stellar atmosphere. These stars also produce ionizing photons and so the stellar winds expand inside of H II regions. We might expect to see a spherical bubble filled with hot, shocked stellar wind material around every young massive star.

The GLIMPSE *Spitzer* Infrared Survey of the Galactic plane identified more than 500 partial and closed rings, interpreted as 2D projections of 3D bubbles (Churchwell et al. 2006, 2009). The survey covers between one and two degrees of latitude either side of the midplane and spans 65 degrees of longitude either side of the Galactic centre. The bubbles are rimmed with PAH emission at  $3.6$  and  $8\mu\text{m}$  and the interiors reveal the presence of warm silicate dust at  $24\mu\text{m}$ . These bubbles are primarily formed by hot young stars in massive star formation regions. About 25% of the bubbles coincide with known radio H II regions produced by O and early B stars, however, the majority are produced by non-ionizing FUV photons from B stars (Churchwell et al. 2009), which do not have important stellar winds. In addition,

the presence of warm dust in the interior is an argument against the bubbles being formed by fast stellar winds, since dust is not produced in a wind and cannot survive in such an environment.

So, if these aren't the bubbles we're looking for, what does the interaction between a fast stellar wind and the environment look like? This review takes as inspiration a conference talk given by You-Hua Chu (Chu et al. 2004), where she posed the questions

- Why don't we see interstellar bubbles around every main sequence O star?
- How hot is the bubble interior?
- What is going on at the hot/cold interfaces in a bubble?

which are still relevant 20 years later. To this list I would add "What are the mass-loss rates?" since these have been revised (downwards) by an order of magnitude in the same time period.

### 2. INTERACTION OF A STELLAR WIND WITH THE ENVIRONMENT

The expansion of a stellar wind bubble in a uniform environment has been studied extensively in the literature, from analytical steady state solutions (Pikel'Ner 1968) and similarity solutions (Avedisova 1972; Dyson & de Vries 1972; Weaver et al. 1977) to numerical simulations (e.g., Falle 1975; Rozyczka 1985; Arthur 2007). Radiation-hydrodynamic simulations are particularly useful since they show that,

<sup>1</sup>Instituto de Radioastronomía y Astrofísica, UNAM, Campus Morelia, Antigua Carretera a Pátzcuaro #8701, Ex-Hda. San José de la Huerta, 58089, Morelia, Michoacán, México (j.arthur@irya.unam.mx).

although the hot shocked stellar wind can drive the dynamics of an internal bubble at early times, at late times the dynamics is governed by the photoionized gas in the external H II region, which dominates the pressure and confines the stellar wind bubble (Arthur 2007). Wind-blown bubbles around O stars in H II regions have been detected kinematically but not morphologically because there is no dense swept-up shell and the expansion speeds are low (Nazé et al. 2001). The temperature in the shocked wind bubble,  $T_{\text{sh}}$ , depends on the stellar wind velocity,  $V_w$ , through the relation  $T_{\text{sh}} = 3\mu m_u V_w^2 / 16k$ , where  $\mu$ ,  $m_u$  and  $k$  are the mean particle mass, the atomic mass unit and the Boltzmann constant, respectively. For typical wind velocities of  $1000 \text{ km s}^{-1}$ , the temperature in the hot gas should be  $> 10^8 \text{ K}$ .

A different structure results if the massive star has supersonic motion relative to its environment. This can happen if the star itself is moving, for example, if it is a runaway star that has been ejected from a cluster, or if the star and its wind are embedded in a larger flow, such as a champagne flow or photoevaporated flow from an H II region. In these scenarios, a bow shock structure forms instead of a spherical bubble (van Buren & Mac Low 1992; Comeron & Kaper 1998). In the upstream direction, the stand-off distance,  $d$ , between the apex of the bow shock and the star is set by the balance between the ram pressure of material passing through the outer shock,  $\rho_0 v_a^2$ , and the thermal pressure of the shocked stellar wind  $\dot{M} V_w / 4\pi d^2$ , where  $v_a$  is the relative velocity between the star and the environment and  $\dot{M}$  is the mass-loss rate. These bow shock structures are most easily seen in the infrared because dust swept up from the environment absorbs UV photons from the massive star and reemits at longer wavelengths. Kobulnicky et al. (2016) catalogued over 700 arc-shaped mid-infrared nebulae in  $24 \mu\text{m}$  *Spitzer* and  $22 \mu\text{m}$  *WISE* surveys of the Galactic Plane as probable dusty interstellar bowshocks.

Observations of H II regions, such as the Eagle Nebula (M16) and the Orion Nebula (M42), reveal that their borders are not regular but instead consist of pillars and other concave and convex structures, clearly seen at optical and near-infrared wavelengths. These are the result of the interaction of the ionizing photons from the massive stars with a surrounding clumpy molecular cloud, and are readily reproduced in numerical simulations of H II regions (Mellema et al. 2006; Medina et al. 2014). The photoevaporation flows coming off the clumps and filaments can reach velocities up to two or three times the sound speed in the photoionized gas and inter-

act in the interior of the H II region, producing a much higher internal velocity dispersion than in the standard expanding Strömgren sphere (Medina et al. 2014). Moreover, many H II regions are found at the edges of molecular clouds where there are strong density gradients. This produces champagne flows (Tenorio-Tagle 1979), in which the ionization front can break out in the direction of decreasing density and leads to a high-pressure outflow with velocities up to several times the sound speed in the ionized gas (Henney 2007). These are the complex environments in which stellar wind bubbles develop.

At first glance, the Bubble Nebula seems to fulfill the role of classical stellar wind bubble inside the photoionized region NGC 7635 which is illuminated by the single central O6.5III star BD+60°25 22. At optical wavelengths, it consists of an approximately circular parsec-scale wind-blown bubble. The stellar wind velocity of  $2000 \text{ km s}^{-1}$  suggests that shocked wind temperatures should be  $> 10^8 \text{ K}$ . However, no extended X-ray emission was detected by Toalá et al. (2020) with their XMM Newton EPIC observations, while optical spectroscopic observations reveal that the apparently simple bubble is really a series of nested shells and blisters. Additionally, the massive star has a peculiar velocity of  $\sim 30 \text{ km s}^{-1}$ , which led Green et al. (2019) to performed 2D hydrodynamical simulations of the Bubble Nebula as a bow shock due to the supersonic motion of the star relative to its environment. The best-matching simulation to the H $\alpha$  and infrared emission required an inclination angle of 60 degrees to the line of sight and the apparent sphericity of the bubble is a simply projection effect. This simulation predicts soft X-ray emission from the edges and wake of the bow shock due to mixing of dense cool gas into the hot shocked wind material, but this is not observed.

The Orion Nebula is a nearby blister H II region illuminated by the O6.5V star  $\theta^1$  Orionis C. The ionizing photons from the hot star photoevaporate material from the surface of nearby protoplanetary discs around young low-mass stars, or proplyds (Henney et al. 1996). The photoevaporation flows are mildly supersonic and flow away from the proplyds until they reach pressure balance with the surrounding medium; for the proplyds closest to the central star this is the free-flowing stellar wind, while for more distant proplyds this could be the photoionized champagne flow (O'Dell et al. 2009). Bow shocks around proplyds are clearly visible in *Hubble Space Telescope* images of the inner Orion Nebula and these are evidence for the stellar wind from  $\theta^1$  Orionis C, even though no closed stellar wind bub-

ble forms due to the strong density gradient at the edge of the molecular cloud.

Of the 709 mid-infrared, bow-shaped nebulae catalogued by Kobulnicky et al. (2016), 286 objects have measured proper motions consistent with a runaway star scenario, 103 objects face giant H II regions and 58 objects face bright-rimmed clouds. An outstanding example of this latter class of object is the O7.5III star Menkib, which faces the California Nebula. Not only is the stellar wind from the hot star interacting with the photoevaporated flow from the face of the bright-rimmed cloud, but the star also has a peculiar motion of  $64 \text{ km s}^{-1}$  towards the nebula. At infrared wavelengths, the PAH near-infrared emission from the face of the nebula can be clearly distinguished from the bow-shaped arc of warm dust mid-infrared emission around the star. However, not all bow-shaped infrared arcs are bow shocks; a hydrodynamical wind-supported bow shock is the result only when radiation effects are unimportant. As the optical depth of the shocked shell increases, radiation pressure contributes a greater fraction of the total pressure to help support the shell structure (Henney & Arthur 2019). The limiting case, when the shell is completely opaque to the stellar radiation, is a radiation-supported bow shock, where it is the radiation pressure that completely balances the ram pressure of the external medium. For intermediate opacities and weak gas-grain coupling, the dust can decouple from the gas, leading to a dust wave outside of a wind-supported bow shock. Thus, the shell optical depth and the degree of coupling between the grains and the gas will determine what sort of bow shock is being observed. Bow shocks have the potential to allow stellar wind parameters, such as velocity and mass-loss rate, to be estimated in wind regimes where traditional diagnostic methods are difficult to apply, such as in the weak-wind regime and for stars with  $T_{\text{eff}} < 25000 \text{ K}$  (Kobulnicky et al. 2016; Mackey et al. 2016).

### 3. STELLAR WINDS FROM MAIN-SEQUENCE MASSIVE STARS

The stellar winds of hot main-sequence stars are driven by the transfer of momentum from photons in the photosphere of very luminous stars to the gas in the stellar atmosphere through absorption by spectral lines (Kudritzki & Puls 2000). The hugely successful *International Ultraviolet Explorer* (IUE) telescope enabled hot star wind velocities to be determined with a high degree of accuracy ( $\sim 10\%$ ) from P Cygni profiles of UV resonance lines of metal ions such as C IV, Si IV and N V. Wind velocities of 2000

to  $3000 \text{ km s}^{-1}$ , or 2 to 3 times the escape speed, are found for main sequence O stars (Prinja et al. 1990). However, the same saturated line profiles cannot be used to determine the mass-loss rates.

The standard, empirical methods for obtaining mass-loss rates from OB stars use the H $\alpha$  recombination line and the radio or sub-mm continuum emission excess (Kudritzki & Puls 2000; Vink 2022). Both of these methods are density-squared dependent and so are sensitive to density inhomogeneities, shocks and clumping in the wind. Additionally, low-abundance unsaturated UV resonance lines like P V, which are linearly dependent on density, can be used to determine the mass-loss rate. Bow shocks can also be used to determine mass-loss rate if the stand-off distance, ambient medium density, relative velocity and wind velocity are known (Kobulnicky et al. 2019). Discrepancies between derived mass-loss rates from different methods of factors up to 2 or 3 are attributed to porosity, i.e. opacity effects from clumping, and vorosity, i.e. the effect of a velocity field on line processes (Owocki 2015).

A factor of only 2 or 3 difference in the main sequence mass-loss rate for a massive star can have huge repercussions for its evolution and final fate, even determining the type of supernova and compact remnant. The mass loss affects the main-sequence lifetime and impacts the core structure. In rotating stars it will affect the rate of angular momentum loss. Renzo et al. (2017) used the MESA stellar evolution code to explore outcomes for various initial mass stars using different mass-loss prescriptions and efficiency factors, and find that the initial mass to final mass ratio can vary by up to 50%, with the greatest uncertainty for stars more massive than  $30 M_{\odot}$ . For a  $60 M_{\odot}$  star, this can be the difference between retaining most of its envelope right up to its death as a  $25 M_{\odot}$  black hole, or losing most of its mass through winds and ending its life as a  $\sim 2 M_{\odot}$  neutron star.

### 4. STELLAR WINDS FROM EVOLVED MASSIVE STARS

Massive stars do not spend much time on the main sequence. After less than 10 million years, core hydrogen burning stops, the stars expand and move to the right in the HRD. Stars with initial masses  $< 30 M_{\odot}$  become a cool, red supergiants (RSG) and will conserve part of the hydrogen envelope until ending their lives as Type II core-collapse supernovae. Derived mass-loss rates from RSG are much higher ( $\sim 10^{-5} M_{\odot} \text{ yr}^{-1}$ ) than for main-sequence stars and determine the final evolution of a star. Mass loss

from RSG is still not well understood: it probably requires the combined effects of radiation pressure on dust grains formed in the cool RSG atmosphere (Gehrz & Woolf 1971) together with pulsations to move sufficient mass to dust-forming regions (Yoon & Cantiello 2010), and empirically determined mass-loss rates differ by more than an order of magnitude (Decin 2021). Moreover, mass loss in RSG is highly anisotropic and episodic, as revealed by the recent “great dimming” of Betegeuse (Dupree et al. 2022).

For stars with initial masses above  $30M_{\odot}$ , the single massive star scenario (Conti 1975) requires the complete loss of the hydrogen envelope before the Wolf-Rayet stage. Beasor & Smith (2022) have suggested that this route implies enhanced mass-loss rates ( $> 10^{-4} M_{\odot} \text{yr}^{-1}$ ) in the RSG stage, which are not observed. Instead, binary interaction has been proposed as a way of removing the stellar envelope, through mass transfer to a companion or through expulsion of a common envelope (Shenar 2022).

Wolf-Rayet stars are hot and produce ionizing photons and fast, radiation-driven winds, with mass-loss rates  $\dot{M} > 10^{-5} M_{\odot} \text{yr}^{-1}$ , at least an order of magnitude higher than those of O stars. This is because multiple scattering of the UV photons in the stellar atmosphere enhances the wind driving efficiency. The fast wind interacts with the circumstellar medium, which is composed of material expelled from the star in a previous stage of evolution or due to a binary interaction. Outside of cluster environments, this interaction can form Wolf-Rayet nebulae, which were first classified by Chu (1981). The most striking nebulae are found around runaway, nitrogen-rich WN stars. For example, the  $\sim 17$  parsec diameter nebula S308 around the WN4 star WR6 is a classical example of a wind-blown bubble (Chu 1981) and is one of only a handful of single massive star bubbles with detectable diffuse X-ray emission (Chu et al. 2003; Toalá et al. 2012). The other bubbles are NGC 2359 around WR7 (Zhekov 2014), NGC 6888 around WR136 (Toalá et al. 2016), and NGC 3199 around WR18 (Toalá et al. 2017). However, despite the high stellar wind velocity ( $V_w = 1700 \text{ km s}^{-1}$ ), the main X-ray component has a derived temperature of only  $1.1 \times 10^6 \text{ K}$ , with a secondary component at  $13 \times 10^6 \text{ K}$  (Toalá et al. 2012). In fact, all of the WR bubbles detected in diffuse X-rays have derived temperatures in the range  $1\text{--}2 \times 10^6 \text{ K}$  (similar to those found for planetary nebulae).

The difference between wind-blown bubbles around Wolf-Rayet stars and those around main sequence O stars is the medium into which they are expanding and the timescales for the interaction. In

Wolf-Rayet bubbles, the fast wind sweeps up the circumstellar medium, which is composed of material previously lost from the stellar envelope. The resulting thin shell is subject to hydrodynamic and radiation-hydrodynamic instabilities and the contact discontinuity between the hot, shocked stellar wind and the cooling swept-up material becomes distorted and very complex (Garcia-Segura et al. 1996; Toalá & Arthur 2011). Mixing at the interface can lead to gas with temperatures intermediate between the  $\sim 10^8 \text{ K}$  shocked wind and the  $\sim 10^4 \text{ K}$  photoionized shell. Thermal conduction can also play a role, evaporating shell material into the hot bubble, where it will have intermediate temperatures. Evidence for conduction fronts in stellar wind bubbles has proved inconclusive, since it requires spectroscopic observations at ultraviolet wavelengths (Chu et al. 2016). Toalá & Arthur (2018) suggest that turbulent mixing layers, together with the filtering effect of the sharply peaked emission coefficient,  $\epsilon(T)$ , are responsible for the narrow range of derived temperatures, even though the actual temperature distribution in the shocked stellar wind is much broader.

For Wolf-Rayet nebulae classified as “ejecta-type” (Chu 1981), such as M1-67 and WR40, the interaction between the fast stellar wind and the circumstellar medium is less clear. If the clumps seen in the nebulae are pre-existing, i.e. come from a clumpy RSG wind or expelled common envelope, numerical simulations of the interaction of a shock with a clumpy medium show that a complex turbulent post-shock flow strips material from the clumps and destroys them, resulting in a thick, dense shell of mixed wind and circumstellar material (Alūzas et al. 2012). Alternatively, the clumps could be formed when a swept-up thin shell becomes dynamically unstable. Studies of Wolf-Rayet nebulae can tell us about the previous mass-loss stages of massive stars and discriminate between possible scenarios.

## 5. CONCLUSIONS

The interaction of stellar winds from massive stars with their environment is important for energy and momentum feedback as well as chemical enrichment of the interstellar medium. Multiwavelength observations, and their interpretation using 2D and 3D numerical simulations, provide insight into physical processes at interfaces and the interaction of stellar winds from stars that are moving with respect to the ambient medium. Bow shocks and dust waves are detected as mid-infrared arcs and are found both inside and outside of the H II regions where massive stars are normally found. Bow shocks

can be used to find model-independent estimates of the stellar wind mass-loss rates. The mass-loss rates continue to be the most uncertain parameter, which has repercussions for the final evolutionary state of massive stars. New X-ray telescopes will help to determine the temperature distributions in the hot shocked gas in wind-blown bubbles but the lack of UV facilities means that it remains difficult to explore the intermediate temperature range predicted for interface regions by numerical simulations.

**Acknowledgments:** I would like to express my appreciation to You-Hua Chu for all of the inspiring encounters and discussions at conferences since 1990, which have had a decidedly positive influence on my research.

## REFERENCES

- Alūzas, R., Pittard, J. M., Hartquist, T. W., Falle, S. A. E. G., & Langton, R. 2012, *MNRAS*, 425, 2212
- Arthur, S. J. 2007, in *Astrophysics and Space Science Proceedings, Vol. 1, Diffuse Matter from Star Forming Regions to Active Galaxies - A Volume Honouring John Dyson*, 183
- Avedisova, V. S. 1972, *Soviet Ast.*, 15, 708
- Beasor, E. R. & Smith, N. 2022, *ApJ*, 933, 41
- Chu, Y. H. 1981, *ApJ*, 249, 195
- Chu, Y.-H., Arthur, S. J., Garcia-Segura, G., et al. 2016, *Resolving the Thermal Conduction Front in the Bubble S308, HST Proposal. Cycle 20, ID. #12875*
- Chu, Y. H., Guerrero, M. A., & Gruendl, R. A. 2004, in *Astrophysics and Space Science Library, Vol. 315, How Does the Galaxy Work?*, 165
- Chu, Y.-H., Guerrero, M. A., Gruendl, R. A., García-Segura, G., & Wendker, H. J. 2003, *ApJ*, 599, 1189
- Churchwell, E., Babler, B. L., Meade, M. R., et al. 2009, *PASP*, 121, 213
- Churchwell, E., Povich, M. S., Allen, D., et al. 2006, *ApJ*, 649, 759
- Comeron, F. & Kaper, L. 1998, *A&A*, 338, 273
- Conti, P. S. 1975, *Memoirs of the Societe Royale des Sciences de Liege*, 9, 193
- Decin, L. 2021, *ARA&A*, 59, 337
- Dupree, A. K., Strassmeier, K. G., Calderwood, T., et al. 2022, *ApJ*, 936, 18
- Dyson, J. E. & de Vries, J. 1972, *A&A*, 20, 223
- Falle, S. A. E. G. 1975, *A&A*, 43, 323
- Garcia-Segura, G., Langer, N., & Mac Low, M. M. 1996, *A&A*, 316, 133
- Gehrz, R. D. & Woolf, N. J. 1971, *ApJ*, 165, 285
- Green, S., Mackey, J., Haworth, T. J., Gvaramadze, V. V., & Duffy, P. 2019, *A&A*, 625, A4
- Henney, W. J. 2007, in *Astrophysics and Space Science Proceedings, Vol. 1, Diffuse Matter from Star Forming Regions to Active Galaxies - A Volume Honouring John Dyson*, 103
- Henney, W. J. & Arthur, S. J. 2019, *MNRAS*, 486, 3423
- Henney, W. J., Raga, A. C., Lizano, S., & Curiel, S. 1996, *ApJ*, 465, 216
- Kobulnicky, H. A., Chick, W. T., & Povich, M. S. 2019, *AJ*, 158, 73
- Kobulnicky, H. A., Chick, W. T., Schurhammer, D. P., et al. 2016, *ApJS*, 227, 18
- Kudritzki, R.-P. & Puls, J. 2000, *ARA&A*, 38, 613
- Mackey, J., Haworth, T. J., Gvaramadze, V. V., et al. 2016, *A&A*, 586, A114
- Medina, S. N. X., Arthur, S. J., Henney, W. J., Mellema, G., & Gazol, A. 2014, *MNRAS*, 445, 1797
- Mellema, G., Arthur, S. J., Henney, W. J., Iliev, I. T., & Shapiro, P. R. 2006, *ApJ*, 647, 397
- Nazé, Y., Chu, Y.-H., Points, S. D., et al. 2001, *AJ*, 122, 921
- O'Dell, C. R., Henney, W. J., Abel, N. P., Ferland, G. J., & Arthur, S. J. 2009, *AJ*, 137, 367
- Owocki, S. P. 2015, in *Astrophysics and Space Science Library, Vol. 412, Very Massive Stars in the Local Universe*, ed. J. S. Vink, 113
- Pikel'Ner, S. B. 1968, *Astrophys. Lett.*, 2, 97
- Prinja, R. K., Barlow, M. J., & Howarth, I. D. 1990, *ApJ*, 361, 607
- Renzo, M., Ott, C. D., Shore, S. N., & de Mink, S. E. 2017, *A&A*, 603, A118
- Rozyczka, M. 1985, *A&A*, 143, 59
- Shenar, T. 2022, *arXiv e-prints*, arXiv:2208.02614
- Tenorio-Tagle, G. 1979, *A&A*, 71, 59
- Toalá, J. A. & Arthur, S. J. 2011, *ApJ*, 737, 100
- \_\_\_\_\_. 2018, *MNRAS*, 478, 1218
- Toalá, J. A., Guerrero, M. A., Chu, Y. H., et al. 2016, *MNRAS*, 456, 4305
- Toalá, J. A., Guerrero, M. A., Chu, Y. H., et al. 2012, *ApJ*, 755, 77
- Toalá, J. A., Guerrero, M. A., Todt, H., et al. 2020, *MNRAS*, 495, 3041
- Toalá, J. A., Marston, A. P., Guerrero, M. A., Chu, Y. H., & Gruendl, R. A. 2017, *ApJ*, 846, 76
- van Buren, D. & Mac Low, M.-M. 1992, *ApJ*, 394, 534
- Vink, J. S. 2022, *ARA&A*, 60, 203
- Weaver, R., McCray, R., Castor, J., Shapiro, P., & Moore, R. 1977, *ApJ*, 218, 377
- Yoon, S.-C. & Cantiello, M. 2010, *ApJ*, 717, L62
- Zhekov, S. A. 2014, *MNRAS*, 443, 12

## MASSIVE STARS HERE AND THERE, ALWAYS WITH SOME IMPACT

Yaël Nazé<sup>1,2</sup>, Beomdu Lim<sup>3</sup>, and Gregor Rauw<sup>1</sup>

### RESUMEN

Puede decirse que las estrellas masivas, con sus fuertes vientos, intensa radiación ionizante y explosión final en forma de supernova, son los principales causantes de la evolución de las galaxias. Esta contribución examinará resultados recientes obtenidos para dos estrellas masivas magnéticas, HD108 y HD148937, los cuales ponen de relieve el impacto en sus respectivos entornos circumstelares.

### ABSTRACT

With their strong winds, intense ionizing radiation, and supernova explosion ending, massive stars can truly be said to be main shaping agents in galaxies. This contribution will examine the case of two magnetic stars, HD108 and HD148937. Recent results obtained for both of them highlight the properties of their circumstellar environments.

*Key Words:* stars: massive — stars: mass-loss — stars: individual (HD108, HD148937)

### 1. INTRODUCTION

Massive stars play a key role when stellar feedback on the interstellar medium (ISM) is considered. Indeed, their intense ionizing radiations, combined to their fast and dense outflows and their deaths as supernovae, are able to shape the ISM on various scales. This contribution examines two cases of magnetic massive stars. Contrary to low-mass stars, magnetism is far from ubiquitous in the high-mass range: only about 7% of such stars were found to be magnetic. The magnetic fields appear strong, temporally stable, and dipolar - all characteristics again in contrast to those of low-mass stars. Such magnetic fields influence the feedback of massive stars on several levels. First, the wind outflows are channelled towards the magnetic equator by the magnetic field (ud-Doula & Owocki 2002). If the star rotates fast, this material can accumulate, creating a dense circumstellar region. If the rotation is slow (as found for most magnetic O-type stars), the material falls back onto the star, reducing the amount of mass injected into the ISM. In addition, strong magnetic fields may modify the inner structure of the stars which, combined to the mass-loss change, modify the stellar evolution hence the overall stellar feedback (Petit et al. 2017; Takahashi & Langer 2021; Keszhelyi et al. 2022). Magnetic massive stars thus

appear relevant in a conference dedicated to circumstellar and interstellar environments.

### 2. HD108

HD108 has a spectral type Of?p. Historically, this peculiar spectral type was introduced to describe O-type spectra with strong C III emission lines near 4650Å (Walborn 1972). With time, it was found that stars of this type exhibited additional peculiarities, notably periodic variabilities of the Balmer emission lines and X-ray overluminosities. The detection of magnetic fields in these stars led to an understanding of these characteristics. The narrow optical emission lines are born in the magnetically confined winds and the plasma collision at the magnetic equator leads to an increase of temperature hence of the X-ray emission. The variability of these features can be explained by a magnetic oblique rotator geometry, which changes the viewing angle on the magnetospheric regions as a function of rotational phase.

The Liège Astrophysics Institute has a long story of studying this star. Its former director, Pol Swings, observed HD108 in the 1940s, then his pupil Jean-Marie Vreux took the succession in the 1970s–1980s, and the Liège co-authors of this paper have continued since. This long chain of observation led us to identify the period of HD108: 54 years (Nazé et al. 2001; Rauw et al. 2023 and references therein). In the context of the magnetic oblique rotator model, this extremely long period should correspond to stellar rotation. This might seem surprising, but the combination of a strong magnetic field and a strong stellar wind can result in a strong magnetic braking (ud-Doula et al. 2009).

<sup>1</sup>STAR/AGO, Université de Liège, Allée du 6 Août 19c, B5c, B-4000, Liège, Belgium.

<sup>2</sup>FRS-FNRS Senior Research Associate (ynaze@uliege.be).

<sup>3</sup>Department of Earth Science Education, Kongju National University, 56 Gongjudaehak-ro, Gongju-si, Chungcheongnam-do 32588, Republic of Korea.

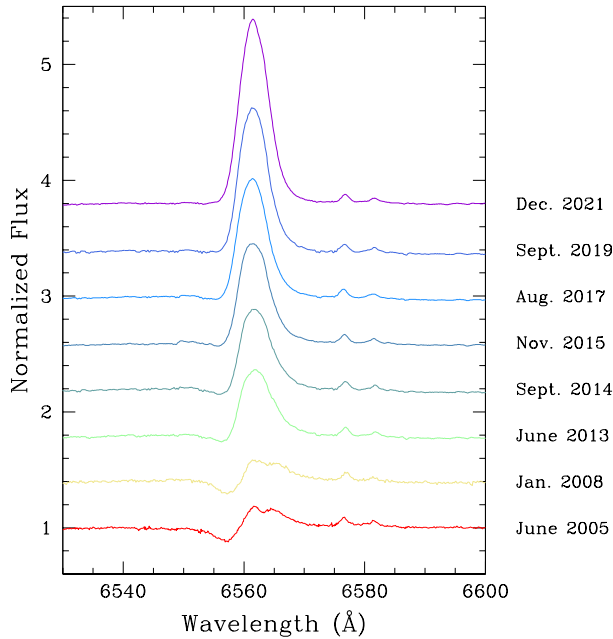


Fig. 1. Time evolution of the  $H\alpha$  profile in the spectrum of HD108, showing how the emission is now recovering after the 2007 minimum.

Over the last two decades, the “minimum emission state” occurred in 2007, as the confined winds were then seen close to edge-on. The optical emissions are now seen to increase again (Fig. 1). While the exact value of the field is not yet known, modelling of the emission variations favors a value around  $-4\text{kG}$  (Rauw et al. 2023). In parallel, new X-ray observations show an increase in luminosity and X-ray hardness, as expected. Finally, radial velocity changes with a period of 8.5 yrs clearly indicate that HD108 is a binary, with a mid-B companion.

### 3. HD148937

HD148937 is one of the other “historic” Of?p stars, but with a much shorter (7d) rotational period and a lower variation amplitude due to its pole-on configuration (see Mahy et al. 2017; Lim et al. 2024 and references therein for details). It is also a binary with  $P \sim 20\text{ yrs}$ , with a companion of similar mass. Finally, it is surrounded by several nebulosities. Faint arcs delineate a large shell  $12'$  in radius, considered to be a wind-blown bubble, while even larger nebulosities are seen as tracing the Strömgren sphere of the star. Closer, on each side of the star, are found the bright nebulae NGC6164 and NGC6165 that form a single elongated structure  $5'$  in diameter centered on HD148937. Due to its expanding motion and its peculiar abundances, it was

interpreted as ejecta, as seen around some LBVs and WR stars.

A recent study of the main NGC6164/5 nebula was performed in the infrared using *WISE*, *Spitzer*, and *Herschel* data (Mahy et al. 2017). The total ejected mass was estimated to be more than  $1.6 M_{\odot}$ . This study further derived abundances in different places of the nebula: in the bright lobes,  $N/O=1.54$  and  $C/O=2.24$ , which is clearly much larger than solar (values of 0.14 and 0.5, respectively), but the fainter nebulosities closer to the star display a lower enrichment:  $N/O=1.06$  and  $C/O=1.42$ . When compared to evolutionary tracks, such abundances yield ages of 0.5–0.7 and 1.2–1.3 Myr for the ejections from the stellar surface giving rise to the faint close and bright distant features, respectively.

Such a distribution of the abundances is difficult to understand within the context of the proposed nebular models. If the ejected material has a helical geometry (Carranza & Agueero 1986), then it would require mass to flow away from the equator, while magnetic channeling works in the other direction. Considering the close and distant features as the result of a two-step ejection also yields problems: if the bright lobes are equatorial and the inner parts polar, the latter ones should have large radial velocity shifts compared to the former, which is not the case (Leitherer & Chavarria-K. 1987); if the bright lobes are polar and the inner features equatorial (Leitherer & Chavarria-K. 1987), then it contradicts the low inclination, pole-on geometry of the star, established through different means. A last possibility is to have both features born in a single event. While magnetic fields of massive stars are sometimes advocated to be the result of a merger event, it remains to be established that the current slow rotation of the magnetic star and the current configuration (mass and orbit) of its companion, initially a third star in this context, are compatible with such an idea. Another event could be a periastron passage, as has been proposed for the eruptions of  $\eta\text{ Car}$ .

To test this idea, new spectra were obtained with ESO’s FLAMES+GIRAFFE instrumentation (Lim et al. 2024). The profiles of the  $H\alpha$  and nearby [SII], [NII] lines were fitted by a set of Gaussians. This revealed that NGC6164/5 has a complex velocity field, with multiple layers of material superimposed along our line-of-sight. To model it, three expanding features were considered: the nitrogen-enriched cores of the bright lobes, their envelopes, and expanding hollow shells close to the equatorial plane. Such a geometry is able to reproduce the observed geometry and velocity field with a single expansion velocity

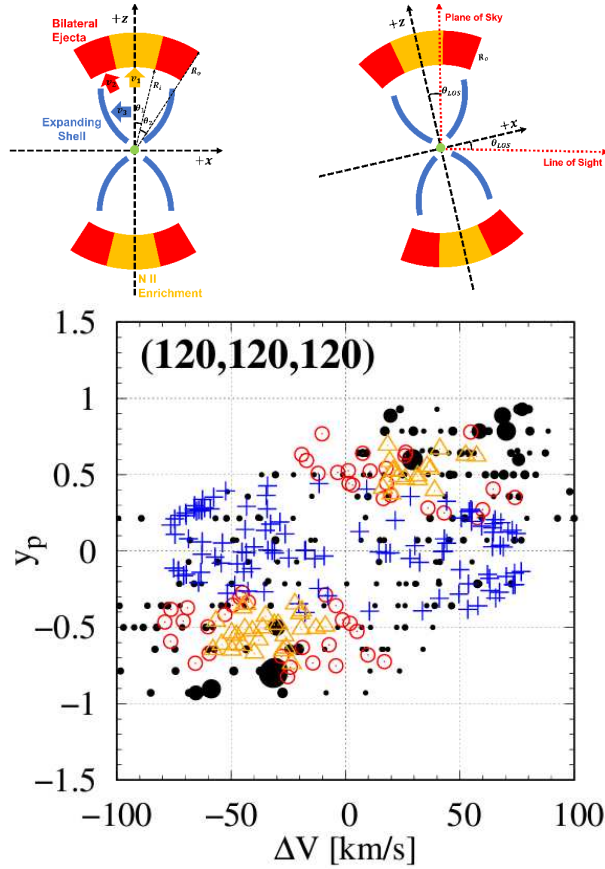


Fig. 2. *Top*: Schematic illustration of the 3-structures model, with nitrogen-enriched cores (orange), envelopes (red), and expanding hollow shells (blue). *Bottom*: Position-velocity diagrams of the measured  $H\alpha$  velocities (black dots) compared to velocities from the model nebula with  $120 \text{ km s}^{-1}$  expansion velocity (nitrogen-enriched cores, envelopes, and hollow shells are shown by orange triangles, red circles, and blue plus symbols, respectively). Figure adopted from Lim et al. (2024).

of  $120 \text{ km s}^{-1}$  (Fig. 2). This would result in an age of 7500 yrs for the nebula, much less than previously believed. The different abundances would then be understood in the framework of a periastron ejection, in which matter from both stars would mix in various proportions depending on the feature under consideration. Further studies are now required to understand whether and how this could happen exactly.

**Acknowledgments:** BL acknowledges support from the National Research Foundation of Korea grant funded by the Korean government (MSIT; grant No. 2022R1C1C2004102). YN and GR acknowledge support from the FNRS, ESA and Belspo (PRODEX Programme).

## REFERENCES

- Carranza, E. & Agueero, E. L. 1986, *Ap&SS*, 123, 59, doi:10.1007/BF00649124
- Keszthelyi, Z., de Koter, A., Götberg, Y., et al. 2022, *MNRAS*, 517, 2028, doi:10.1093/mnras/stac2598
- Leitherer, C. & Chavarria-K., C. 1987, *A&A*, 175, 208
- Lim, B., Naze, Y., Chang, S.-J., et al. 2024, *ApJ*, 961, 72
- Mahy, L., Hutsemékers, D., Nazé, Y., et al. 2017, *A&A*, 599, A61, doi:10.1051/0004-6361/201629585
- Nazé, Y., Vreux, J.-M., & Rauw, G. 2001, *A&A*, 372, 195, doi:10.1051/0004-6361:20010473
- Petit, V., Keszthelyi, Z., MacInnis, R., et al. 2017, *MNRAS*, 466, 1052, doi:10.1093/mnras/stw3126
- Rauw, G., Nazé, Y., ud-Doula, A., et al. 2023, *MNRAS*, 521, 2874, doi:10.1093/mnras/stad693
- Takahashi, K. & Langer, N. 2021, *A&A*, 646, A19, doi:10.1051/0004-6361/202039253
- ud-Doula, A. & Owocki, S. P. 2002, *ApJ*, 576, 413, doi:10.1086/341543
- ud-Doula, A., Owocki, S. P., & Townsend, R. H. D. 2009, *MNRAS*, 392, 1022, doi:10.1111/j.1365-2966.2008.14134.x
- Walborn, N. R. 1972, *AJ*, 77, 312, doi:10.1086/111285

## WIND-BLOWN NEBULAE FROM MASSIVE STARS

J. Mackey<sup>1</sup>

RESUMEN

La interacción entre el viento estelar y el medio interestelar de una estrella que se mueve supersónicamente a través de este genera nebulosas de choque de proa. Simulaciones de esta interacción pueden modelar su emisión térmica desde radio hasta rayos X. Modelos hidrodinámicos axialmente simétricos predicen fuerte emisión difusa de rayos X en las turbulencias tras el paso del choque de proa, pero esta no se detecta en NGC 7635. Por el contrario, las simulaciones 3D con campos magnéticos predicen emisión difusa en rayos X inferior a la que se detecta en  $\zeta$  Oph. Aquí presento un estudio preliminar de los efectos de resolución en el nivel de emisión en rayos X, demostrando que la emisión puede variar notablemente en tiempo y la necesidad de obtener cálculos de alta resolución para resolver las inestabilidades dinámicas en la discontinuidad de contacto.

ABSTRACT

Bow shocks are nebulae produced by interaction between stellar winds and the interstellar medium, when the star is moving supersonically through its surroundings. Simulations can model the interaction and its thermal emission from radio to X-rays. Axisymmetric hydrodynamic models predicted strong diffuse X-ray emission from the turbulent wake behind the star, but this was not detected in observations of NGC 7635. In contrast, 3D simulations including magnetic fields underpredicted the diffuse X-ray emission observed around  $\zeta$  Oph. I present preliminary work studying the effects of resolution on the simulated X-ray emission, demonstrating significant time-variation in the emission and the importance of high-resolution calculations to resolve dynamical instabilities at the contact discontinuity.

*Key Words:* methods: numerical — ISM: bubbles — circumstellar matter — X-rays: ISM

### 1. INTRODUCTION

Nebulae are rare around main-sequence massive stars except for the runaway stars, where the dynamical pressure of the relative motion between star and interstellar medium (ISM) keeps the wind-ISM interaction region close to the star and also shock-compresses the interstellar gas (Henney & Arthur 2019a; Mackey 2023). The outer shock is typically isothermal so that large compression factors may occur. Because the whole region is photoionized by the central star's EUV radiation, this shocked ISM emits optical and infrared spectral lines of common diagnostic ions and bremsstrahlung in the radio band. Bow shocks also emit synchrotron radiation at radio wavelengths; see PhD project of M. Moutzouri and Moutzouri et al. (2022). Dust that is heated by the intense stellar radiation field emits brightly in the mid-infrared, and this is the most successful waveband for detecting bow shocks (van Buren & McCray 1988; Henney & Arthur 2019b). At the contact discontinuity between shocked ISM (with temperature  $T \sim 10^4$  K) and shocked stellar-wind

( $T \sim 10^7$  K) there is an interface layer of mixed material at intermediate temperatures, produced by hydrodynamic instabilities and subsequent turbulent mixing (Mackey et al. 2015; Toalá & Arthur 2018) and/or thermal conduction (Meyer et al. 2014). This gas may emit brightly in soft X-rays (Toalá et al. 2016, 2017) and UV lines (Borosso et al. 1997), depending on the effectiveness of the mixing processes.

Green et al. (2019) studied the Bubble Nebula (NGC 7635) using 2D hydrodynamical simulations assuming the nebula is produced by a runaway star moving into a dense ISM. These high-resolution simulations showed strong mixing at the wind-ISM interface, generated by shear-induced Kelvin-Helmholtz instability (KHI), and resulting in a turbulent flow in the wake behind the star (similar to Mackey et al. 2015). Synthetic observations showed reasonable morphological agreement with infrared and optical emission from the nebula, but the predicted soft X-ray emission was significantly larger than the upper limits subsequently obtained by Toalá et al. (2020). The vigorous mixing in the simulated nebula was evidently stronger than is occurring in Nature.

To investigate this discrepancy, Green et al. (2022) made 3D MHD simulations of the bow shock

<sup>1</sup>Dublin Institute for Advanced Studies, Astronomy & Astrophysics Section, DIAS Dunsink Observatory, Dublin, D15 XR2R, Ireland (jmackey@cp.dias.ie).

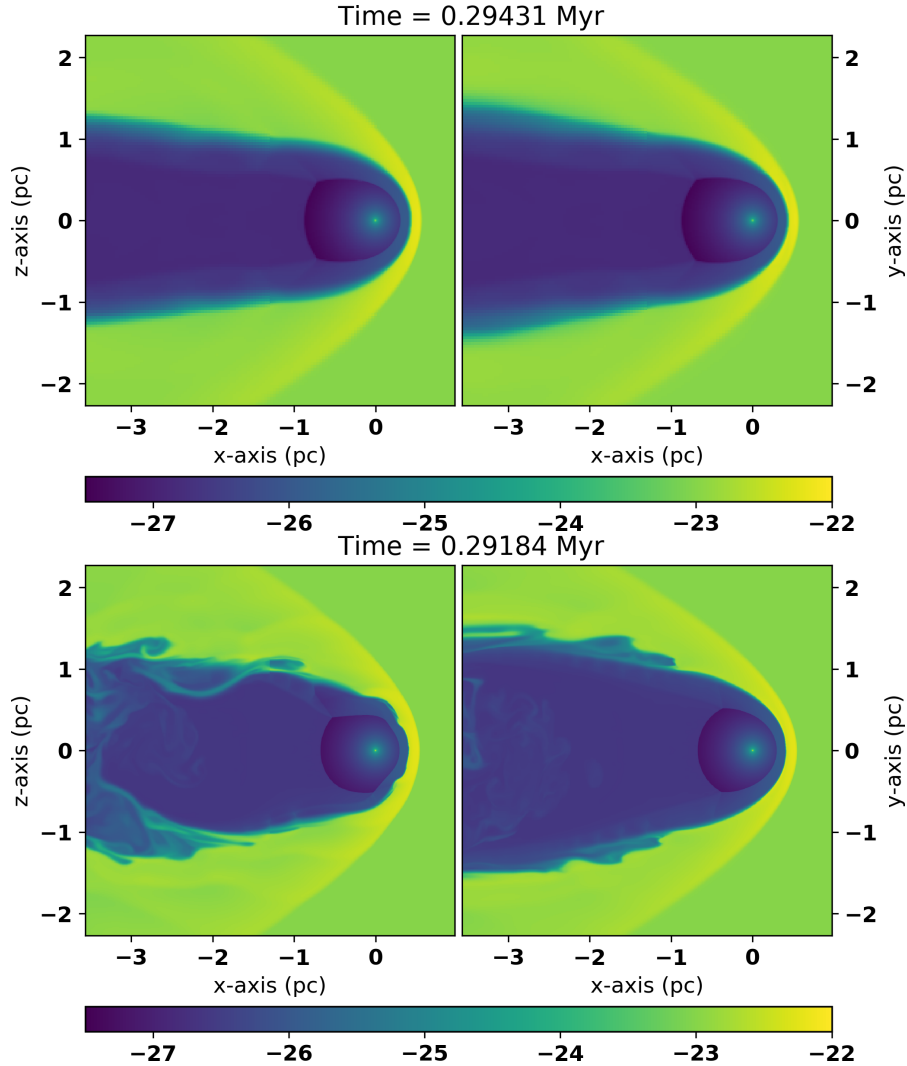


Fig. 1. Snapshots of  $\log_{10}$  of gas density in  $\text{g cm}^{-3}$  from 3D simulations with low- ( $128^3$ , 3 refinement levels, above) and high- ( $384^3$ , 3 refinement levels, below) resolution, of the same bow shock using MHD with the ISM magnetic field almost perpendicular to the space velocity of the star. The star is moving from left to right into a uniform ISM and is located at the origin. In both plots the left panel shows the plane  $y = 0$  and the right panel shows  $z = 0$ .

of  $\zeta$  Oph, the closest O star to Earth and the only one with detected diffuse X-ray emission from the shocked stellar wind (Toalá et al. 2016). Surprisingly, they found that the simulations significantly *underpredicted* the soft X-ray emission compared with observations. This could have been a result of insufficient numerical resolution (the KHI was absent), suppression of mixing by magnetic fields, or because thermal conduction was not included in the calculations. This prompted us to undertake a study of the effects of different physical and numerical approximations on the resulting X-ray emission predicted by simulations, especially to assess numerical convergence. The same simulation was run with the

PION MHD code (Mackey et al. 2021) in 2D and 3D, with (i) hydrodynamics and MHD, (ii) a diffusive (HLL) and a more accurate (HLLD) flux solver, and (iii) varying numerical resolutions consistent with available computing resources.

## 2. RESULTS

Simulations were run of the bow shock produced by a runaway star moving at  $v_* = 30 \text{ km s}^{-1}$  in the positive  $\hat{x}$  direction through a uniform ISM with density  $\rho = 10^{-23} \text{ g cm}^{-3}$  and magnetic field  $\mathbf{B} = \{1, 4, 0\} \mu\text{G}$ . Static mesh-refinement was used with 3 grid levels focused on the centre of the domain at the  $+\hat{x}$  boundary, so that the apex of the bow shock

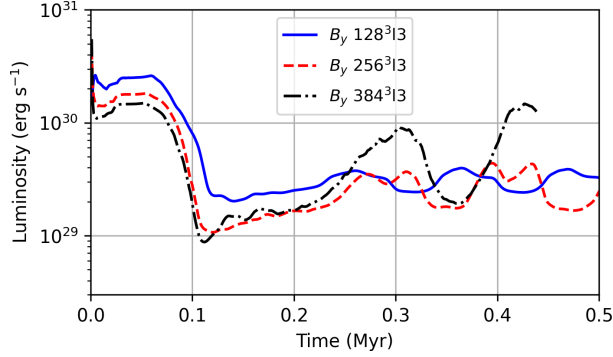


Fig. 2. X-ray emission (0.3–10 keV) from 3D MHD simulations of the same bow shock as a function of time for three different numerical resolutions.

has the highest spatial resolution. A reference frame is used such that the star is at rest with respect to the grid and located at the origin.

Slices through 3D MHD simulations plotting gas density on a logarithmic colour scale are shown in Figure 1. The upper panels show a low-resolution simulation with  $128^3$  grid cells per level and 3 refinement levels. The lower panels show the same simulation but with  $384^3$  grid cells per level and at an earlier time. Both simulations use the HLLD solver. The qualitative difference in the solution is obvious, with KHI active in the high-resolution case but not resolved in the low-resolution case. The KHI introduces some time-variation in the simulation properties for the high-resolution case, whereas the low-resolution simulation has reached an almost-stationary state.

Figure 2 shows predicted X-ray luminosity (0.3–10 keV) of the diffuse gas within the simulations as a function of time for three different resolutions as indicated in the legend. The dynamical timescale of the bow shock,  $\tau \sim R_0/v_*$  ( $R_0$  is the distance from the star to the wind-termination shock), is approximately 0.1 Myr. The initial high X-ray emission followed by a sharp drop after 0.1 Myr is a relic of the initial conditions. At the lowest resolution the X-ray luminosity relaxes to an almost-constant value, reflecting the lack of KHI and the resulting time-variation that this process produces. At medium resolution ( $256^3$  cells) there is more variation, about a factor of 3 from peak to trough, and at the highest resolution ( $384^3$  cells) the variability is an order of magnitude from peak to trough, driven by KHI. While this sequence of simulations has not converged numerically, the large range of X-ray luminosities found in the highest-resolution simulation is compa-

table to the range found for even higher-resolution 2D simulations.

### 3. CONCLUSIONS

A large suite of hydrodynamic and MHD simulations of bow shocks has been run and is currently being analysed (Mackey et al., in preparation). The preliminary results indicate that low-resolution 3D simulations may lack the spatial resolution to capture the KHI at the wind-ISM interface, resulting in a bow shock that is artificially stabilised by numerical diffusion. Higher-resolution simulations capture the KHI and the consequent turbulent mixing of wind and ISM material in the wake behind the star, resulting in time-variable X-ray emission that may vary by an order of magnitude depending on the time of observation. Using a turbulent model for the ISM (rather than the uniform medium considered here) may result in even stronger time variation.

**Acknowledgements:** I would like to thank my many colleagues who worked with me on these projects over the past 10 years; it has been a pleasure working with you all! This work was supported by a Royal Society-Science Foundation Ireland University Research Fellowship.

### REFERENCES

- Boroson, B., McCray, R., Oelfke Clark, C., et al. 1997, *ApJ*, 478, 638
- Green, S., Mackey, J., Haworth, T. J., Gvaramadze, V. V., & Duffy, P. 2019, *A&A*, 625, A4
- Green, S., Mackey, J., Kavanagh, P., et al. 2022, *A&A*, 665, A35
- Henney, W. J. & Arthur, S. J. 2019a, *MNRAS*, 486, 3423
- . 2019b, *MNRAS*, 489, 2142
- Mackey, J. *Winds of Stars and Exoplanets*, ed. , A. A. Vidotto L. Fossati & J. S. Vink, Vol. 370, 205–216
- Mackey, J., Green, S., Moutzouri, M., et al. 2021, *MNRAS*, 504, 983
- Mackey, J., Gvaramadze, V. V., Mohamed, S., & Langer, N. 2015, *A&A*, 573, A10
- Meyer, D. M.-A., Mackey, J., Langer, N., et al. 2014, *MNRAS*, 444, 2754
- Moutzouri, M., Mackey, J., Carrasco-González, C., et al. 2022, *A&A*, 663, A80
- Toalá, J. A. & Arthur, S. J. 2018, *MNRAS*, 478, 1218
- Toalá, J. A., Guerrero, M. A., Todt, H., et al. 2020, *MNRAS*, 495, 3041
- Toalá, J. A., Marston, A. P., Guerrero, M. A., Chu, Y. H., & Gruendl, R. A. 2017, *ApJ*, 846, 76
- Toalá, J. A., Oskinova, L. M., González-Galán, A., et al. 2016, *ApJ*, 821, 79
- van Buren, D. & McCray, R. 1988, *ApJ*, 329, L93

## IMPLEMENTATION OF MULTI-ION CHEMICAL KINETICS FOR CIRCUMSTELLAR NEBULAE

Arun Mathew<sup>1</sup> and Jonathan Mackey<sup>1</sup>

### RESUMEN

Se presenta el desarrollo de un módulo multi-iónico fuera de equilibrio con funciones de enfriamiento para cada ión considerando abundancias elementales arbitrarias desarrollado para cubrir un amplio rango de temperaturas entre  $10^{3.5} - 10^{8.5}$  K. Se han llevado a cabo una serie de validaciones para determinar la precisión y eficiencia del módulo en diferentes escenarios, incluyendo variaciones en la temperatura, abundancias y especies químicas y en la velocidad de un flujo.

### ABSTRACT

A non-equilibrium multi-ion chemistry model is developed to cover a broad temperature range of  $10^{3.5} - 10^{8.5}$  K, with cooling functions computed on an ion-by-ion basis, accommodating arbitrary elemental abundances. Several validation tests are conducted to assess the accuracy and effectiveness of our approach across various scenarios, including variations in flow velocity, temperature, abundances, and chemical species.

*Key Words:* atomic processes — methods: numerical — plasmas — shockwaves

### 1. INTRODUCTION

Chemical kinetics, integrated into Hydrodynamic (HD) and Magnetohydrodynamic (MHD) simulations for investigating circumstellar nebulae around stars like Wolf-Rayet nebulae (García-Segura et al. 1996) and colliding-wind binaries (Parkin et al. 2011), often rely on oversimplified assumptions of thermal and/or ionization equilibrium or homogeneous elemental abundances. However, extreme variations in elemental abundances across circumstellar nebulae of evolved stars (Esteban et al. 2016) and the presence of strong shockwaves may invalidate these assumptions. Furthermore, in colliding-wind binaries, the winds from the two stars may exhibit vastly different abundances (e.g. Pollock et al. 2005). The application of cooling curves, whether under collisional ionization equilibrium (CIE) (e.g. Sutherland & Dopita 1993) or photoionization equilibrium (Wiersma et al. 2009), may not always be suitable in such complex scenarios. Thus, integrating more detailed models that account for these complexities may advance our understanding of the evolution of circumstellar nebulae, and certainly enables more realistic comparison of simulations with observational data on line-emission from nebulae.

In this present work, we have significantly enhanced the microphysics module within PION, a grid-based HD and MHD simulation code that includes

radiative transfer of ionizing and non-ionizing photons for R-HD and R-MHD (Mackey et al. 2021). Previously, the module relied on a single tracer variable representing the Hydrogen ion fraction, with ionization states of He, C, N, and O aligned with that of hydrogen. Our new module now accommodates multiple chemical species, spatially varying elemental abundances and non-equilibrium ionization of each element. Our new module features a highly realistic ion-by-ion based cooling function utilizing CHIANTIPy v0.15.0 (Zanna et al. 2021; Young et al. 2003) with CHIANTI database version 10.0.2. This represents a significant enhancement over the previous version’s cooling function.

In the forthcoming sections, we outline the theory and a comprehensive array of tests aimed at validating the accuracy and efficiency of our method across diverse scenarios. These scenarios encompass variations in density, temperature, metallicity, and chemical species. In Section 3, we establish CIE cooling functions. Additionally, we conduct 1D MHD shock tests under non-adiabatic conditions with cooling activated. Moreover, we outline our future intentions in our conclusion.

### 2. CHEMICAL KINETICS

Apart from the ideal inviscid MHD equations we solve the equations of all ions of H, He, C, N, O, Ne, Si, S, and Fe through

$$\frac{\partial \rho X_{\kappa,i}}{\partial t} + \nabla \cdot (\rho X_{\kappa,i} \vec{v}) = \rho S_{\kappa,i}, \quad (1)$$

<sup>1</sup>Dublin Institute for Advanced Studies, Astronomy & Astrophysics Section, DIAS Dunsink Observatory, Dublin, D15 XR2R, Ireland (arun, jmackey@cp.dias.ie).

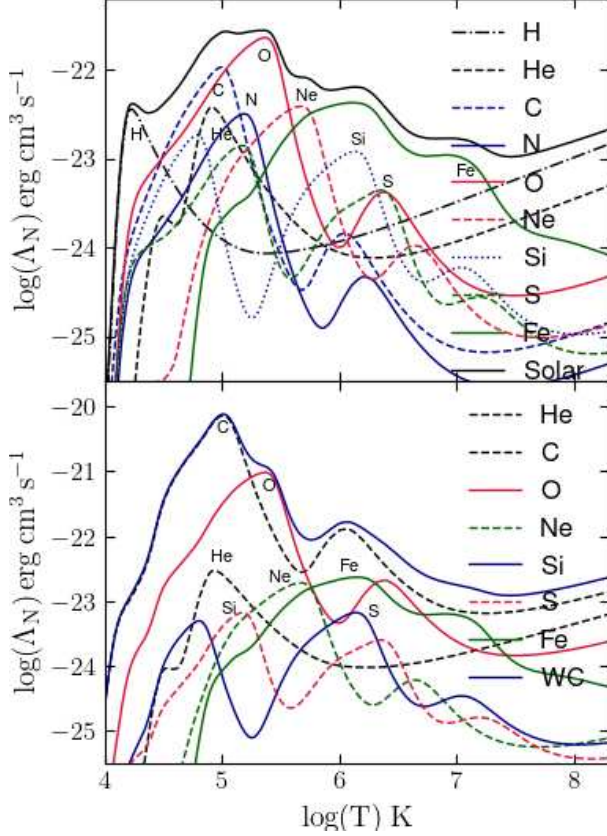


Fig. 1. Elemental contributions  $n_e \sum_i n_{\kappa,i} \Lambda_{\kappa,i}$  (scaled with  $(m_H/\rho)^2$ ) and net cooling function  $\Lambda_N$  for Solar (top panel) and WC (bottom panel) abundances.

where  $X_{\kappa,i}$  denotes the fraction of the  $i$ -th ionization state of element  $\kappa$ . The source term  $S_{\kappa,i}$  represents the net rate of change due to ionization processes, given by:

$$S_{\kappa,i} = X_{\kappa,i+1} n_e \alpha_{\kappa,i+1} - X_{\kappa,i} (n_e \zeta_{\kappa,i} + n_e \alpha_{\kappa,i} + \beta \delta_{i0}) + X_{\kappa,i-1} n_e \zeta_{\kappa,i-1}, \quad (2)$$

where,  $\zeta_{\kappa,i}(T)$  and  $\alpha_{\kappa,i}(T)$  are temperature-dependent collisional ionization and recombination rate coefficients, respectively. The cosmic-ray ionization rate is assumed constant at  $\beta = 1.0 \times 10^{-17} \text{ s}^{-1}$  (Goldsmith & Langer 1978) and  $\delta_{i0}$  is the Kronecker delta. These equations are solved using an operator splitting method, with the source term evolved using backward differencing with Newton iteration utilizing the SUNDIALS/CVODE library (Cohen et al. 1996).

The source term for the energy equation associated with chemical kinetics is

$$S_E = -(L_{\text{coll}} + L_{\text{rec}} + L_{\text{cool}}) + Q_{\text{cr}}, \quad (3)$$

with the radiative cooling term given by  $L_{\text{cool}} = n_e \sum_{\kappa,i} n_{\kappa,i} \Lambda_{\kappa,i}$ , involving individual radiative cooling rates  $\Lambda_{\kappa,i}(n_e, T)$  per electron, per ion of the species  $\kappa$ , and charge  $i$ , calculated using CHIANTIpy v0.15.0 with CHIANTI database version 10.0.2. Radiative losses due to recombination are expressed as  $L_{\text{rec}} = \frac{3}{2} k_B n_e T \sum_{\kappa} \sum_{i=1}^{N_{\kappa}} \alpha_{\kappa,i} n_{\kappa,i}$ , and radiative losses due to collisional processes are given by  $L_{\text{coll}} = n_e \sum_{\kappa} \sum_{i=0}^{N_{\kappa}-1} I_{\kappa,i} \zeta_{\kappa,i} n_{\kappa,i}$ . The heating consists of cosmic rays and is represented by  $Q_{\text{cr}} = \langle E_{\text{cr}} \rangle \beta \sum_{\kappa} n_{\kappa,0}$ . This is based on the simple assumption of constant deposition of average ionization energy, with  $\langle E_{\text{cr}} \rangle = 20 \text{ eV}$  per ionization of neutral species into the gas. The source term is evaluated by integrating the internal energy density of the gas together with the ionization rate equations in CVODE.

### 3. SIMULATIONS AND RESULTS

PION is now updated to include cooling rates for a range of ions including H, He, C, N, O, Ne, Si, S, and Fe. We compute the ionization fraction for all ions corresponding to the aforementioned elements under CIE, as a function of temperature. Utilizing this one can obtain the CIE cooling function as shown in Figure 1. Here the radiative cooling accounts for line-emission, free-bound emission, Bremsstrahlung emission, and two-photon emission.

The top panel of Figure 1 depicts cooling contributions from various elements under CIE conditions at different temperatures, assuming solar photospheric abundances (Asplund et al. 2009). These align with prior computations (Sutherland & Dopita 1993), though differences in atomic data can cause variations. The bottom panel contrasts the cooling function obtained for a plasma with abundances appropriate for the wind of a WC9 star (Eatson et al. 2022), where cooling is notably higher compared to solar abundances, particularly in the range  $\log T$  from 4.5 to 6.5. However, in the  $10^4 < T < 1.5 \times 10^4 \text{ K}$  range, solar abundances exhibit superior cooling, emphasizing the impact of elemental abundances on cooling.

Figure 2 depicts the spatial ionization profile of Fe in a non-adiabatic planar shock test with inflow velocities of 1000 km/s and 3000 km/s. The flow direction is from right to left, and the shock is located near the right edge of the plot. Ionization progresses from right to left starting from the shock front, due to finite ionization time scales for each ionization state. The temperature increase behind the shock allows ionization across multiple Fe ion levels. Higher ionization states become significant at specific distances from the shock front, influenced by the gas

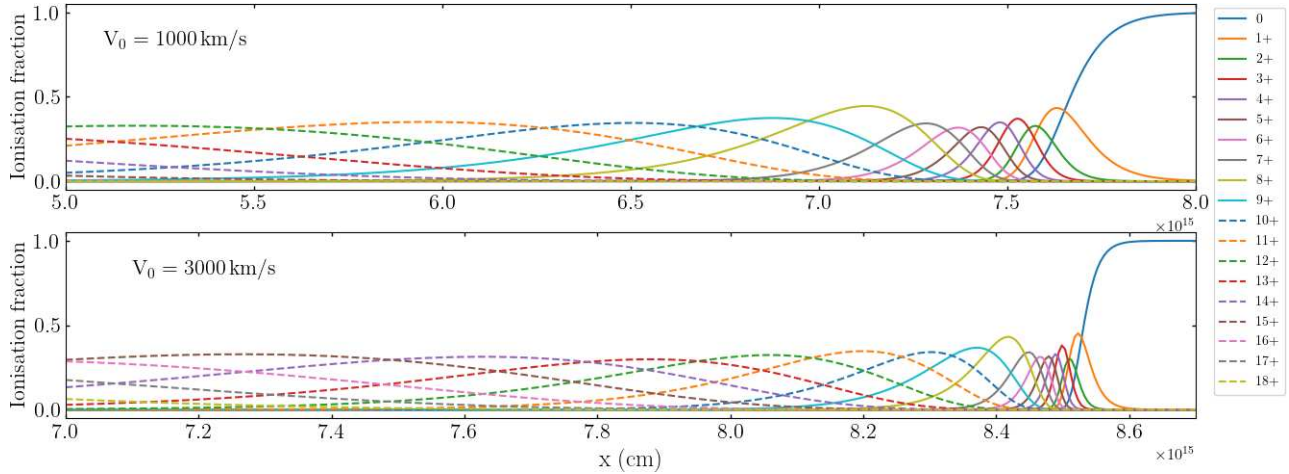


Fig. 2. Spatial profiles of ion fractions for different ionization levels of Iron behind the shock front in non-adiabatic flows at velocities of 1000 km/s (top panel) and 3000 km/s (bottom panel).

temperature. Immediately behind the shock, lower ionization states dominate the emission spectra, albeit with minor contributions due to their smaller area under the curve. In contrast, highly ionized gas emits away from the shock front, contributing substantially to the spectra. However, as the post-shock gas cools, recombination processes promote increasing contributions from lower ionization states to the spectra.

#### 4. CONCLUSION

Here, we introduce a novel non-equilibrium multi-ion module being developed for the R-MHD code PION. This provides enhanced accuracy in tracking ionization state and temperature both temporally and spatially. This advancement holds significant promise for enhancing the predictive capabilities of computer simulations. For instance, it can greatly improve the fidelity of synthetic X-ray spectra of hot plasma and the spectral lines of ions across UV/optical/IR wavelengths. Moreover, the incorporation of an ion-by-ion cooling function further strengthens its utility, enabling meaningful predictions even under non-equilibrium conditions where elemental abundances may dynamically evolve, such as in scenarios involving stellar wind or colliding-wind binaries.

Our future plans involve expanding this module's functionality to encompass multi-ion photoionization resulting from a single radiation source and charge exchange reactions. This extension will broaden the scope of applications, enabling more comprehensive

simulations in scenarios where such interactions play a crucial role.

#### REFERENCES

- Asplund, M., Grevesse, N., Sauval, A. J., & Scott, P. 2009, *ARA&A*, 47, 481, <https://doi.org/10.1146/annurev.astro.46.060407.145222>
- Cohen, S. D., Hindmarsh, A. C., & Dubois, P. F. 1996, *ComPh*, 10, 138, <https://doi.org/10.1063/1.4822377>
- Eaton, J. W., Pittard, J. M., & Van Loo, S. 2022, *MNRAS*, 516, 6132, <https://doi.org/10.1093/mnras/stac2617>
- Esteban, C., Mesa-Delgado, A., Morisset, C., & García-Rojas, J. 2016, *MNRAS*, 460, 4038, <https://doi.org/10.1093/mnras/stw1243>
- García-Segura, G., Langer, N., & Mac Low, M. 1996, *A&A*, 316, 133
- Goldsmith, P. F. & Langer, W. D. 1978, *ApJ*, 222, 881
- Mackey, J., Green, S., Moutzouri, M., et al. 2021, *MNRAS*, 504, 983
- Parkin, E. R., Pittard, J. M., Corcoran, M. F., & Hamaguchi, K. 2011, *ApJ*, 726, 105
- Pollock, A. M. T., Corcoran, M. F., Stevens, I. R., & Williams, P. M. 2005, *ApJ*, 629, 482
- Sutherland, R. S. & Dopita, M. A. 1993, *ApJS*, 88, 253
- Wiersma, R. P. C., Schaye, J., & Smith, B. D. 2009, *MNRAS*, 393, 99
- Young, P. R., Del Zanna, G., Landi, E., et al. 2003, *ApJS*, 144, 135
- Del Zanna, G., Dere, K. P., Young, P. R., & Landi, E. 2021, *ApJ*, 909, 38, <https://dx.doi.org/10.3847/1538-4357/abd8ce>

## SMALL BUBBLES AROUND BIG STARS

K. Weis<sup>1</sup>

### RESUMEN

La vida de las estrellas masivas es corta y está dominada por fuertes vientos estelares. Este viento puede acumular material en nebulosas circunestelares alrededor de estrellas masivas. Algunas estrellas masivas pueden pasar la fase de variable luminosa azul (LBV), una fase de transición entre la fase de secuencia principal de la estrella y su estado final como RSG, BSG o la estrella Wolf-Rayet. Las LBVs son, como su nombre indica, estrellas variables y tienen una tasa de pérdida de masa muy alta. Muchas, por lo tanto, tienen pequeñas nebulosas. Cómo se ven estas nebulosas, cómo se formaron y qué implican para la fase LBV y lo que causa la inestabilidad que además del viento es responsable de la formación de las nebulosas son los temas que se abordan aquí.

### ABSTRACT

The life of massive stars is short and dominated by strong stellar winds. This wind can accumulate material in circumstellar nebulae around massive stars. Some massive stars may pass the Luminous Blue Variable (LBV) phase, a transitional phase between the stars main-sequence phase and its final state as either RSG, BSG or Wolf-Rayet star. LBVs are as the name indicates variable stars, have a very large mass-loss rate. Many therefore have small nebulae. How these nebulae look like, how they formed and what they imply for the LBV phase and what causes the instability that beside the wind is responsible for the formation of the nebulae are topics addresses here.

*Key Words:* stars: massive — stars: mass loss — stars: winds, outflows

### 1. INTRODUCTION

Circumstellar nebulae or bubbles around stars are not unusual. During the rather short life massive star lose a significant part of their mass via stellar winds. In the main-sequence phase this wind sweeps up the surrounding interstellar medium and forms a wind blown bubble a theoretical description is given by Weaver et al. (1977). Only later, after several evolutionary phases with faster and slower winds circumstellar bubble form around stars. Examples are Planetary Nebulae, Wolf-Rayet Nebulae and Luminous Blue Variable Nebulae.

### 2. LUMINOUS BLUE VARIABLES (LBVS)

LBVs are evolved massive stars. Observations and theoretical stellar evolution models that include rotation (Meynet & Maeder 2005) find LBVs with initial mass as low as  $22 M_{\odot}$ . The original term Luminous blue Variables was introduced by Peter Conti during a conference talk he said: I shall refer to the non WR or other hot stars as Luminous blue Variables. This spontaneous introduction of the name was not intended as and is far from any good definition. By now several characteristics are known to

clearly distinct an LBV from normal blue supergiant. It is the variability! LBVs change their spectra from a hot OB stars to a cool AF stars and back by changing their radius. This S Dor variability or S Dor cycle can be as short as a few years or up to several decades and is intrinsic to LBVs. More violent variations are the giant eruptions, here the brightness rises spontaneously by several magnitudes. These LBVs are designated *giant eruption LBVs*, the best known examples are  $\eta$  Car, P Cygni, NGC2403-V12, and SN1961V, the latter indicating LBV giant eruptions have been mistaken for supernovae. In wake of the large SN search programmes now ongoing, transient events that look like a supenova at first, but for the one or the other reason turn out to be non-terminal explosions, are dubbed 'SN imposters'. One view is indeed to claim that they are LBV giant eruptions. Indeed giant eruptions will look like SN imposters **but not** all SN imposter are giant eruptions. For a detailed review of LBVs see Weis & Bomans (2020)

### 3. LBV NEBULAE

The change in spectral type during a S Dor cycle leads to changes in the stellar wind velocity and wind wind interaction of the fast hot star wind with slower and denser cool star wind. During a giant eruption

<sup>1</sup>Astronomical Insitute, Faculty for Physics & Astronomy, Ruhr University Bochum.

larger amounts of mass can be ejected in less than a few years. Both scenarios are formation mechanism for circumstellar nebula, the LBV nebulae. LBV nebulae are rather small, with a typical diameters of a few parsec. A large fraction ( $\sim 70\%$ ) shows a bipolar morphology only a few are really spherical. So far only one R 143 is irregular (Weis 2003), given its position in a rather turbulent environment—near the center of 30 Dor giant HII region—this is not really surprising.

The expansion velocities are often complex patterns with a range from a few km/s to well above 1000 km/s. LBV nebulae have strong [N II] emission. Nebulae of LMC LBVs are on average larger, at the same time their expansion velocities are slower as the galactic. (Weis 2011)

### 3.1. The petite LBV nebulae

A few LBVs nebulae have physical size below 1 parsec, for now I call them the petite LBV nebulae. This subsample contains the nebulae of the giant eruption LBVs  $\eta$  Car and P Cygni, the classic galactic LBVs HD 168625, the largest petite is WRA 751 and finally S61 the smallest of all LMC LBV nebulae.

**HD 169625:** Is with a size of  $0.13 \times 0.17$  pc the smallest galactic LBV nebula. The size indicate an already not spherical shape, the kinematics I derived from longslit echelle spectra indicate an asymmetric or even bipolar structure expanding with 30 km/s. Supportingly Mahy et al. (2016) mentioned bipolar components, looking at the enlargement of the HST image in Fig.1 one is tempted to identify two shells nearly on top of each other.

**WRA 751:** The nebulae appear very diffuse, its inner body is spherical with a radius of 0.38 pc but to the north and south triangular shaped extension are detected, they are 0.05 and 0.1 pc long and the kinematics reveal a clearly bipolar nature. For a detailed discussion Weis (2000)

**P Cygni:** Is one of the few LBVs in the northern hemisphere. It has two distinct nebulae a larger outer structure with a size of larger with a diameter of 0.8 to 0.9 pc (not shown here) And the inner nebulae with a diameter of 0.2 pc (Fig. 1 shows our new LBT AO image) and an expansion velocity of 100-250 km/s that matches an ejection during the 1600AD giant eruption (Weis et al. in Prep)

**$\eta$  Carinae:** Has at least three nebula structures, the Homunculus, first observed and described as little manikin or Homunculus by Gaviola (1950), the Little Homunculus (Ishibashi et al. 2003) nestled inside the Homunculus (maximum size of about 0.04 pc).

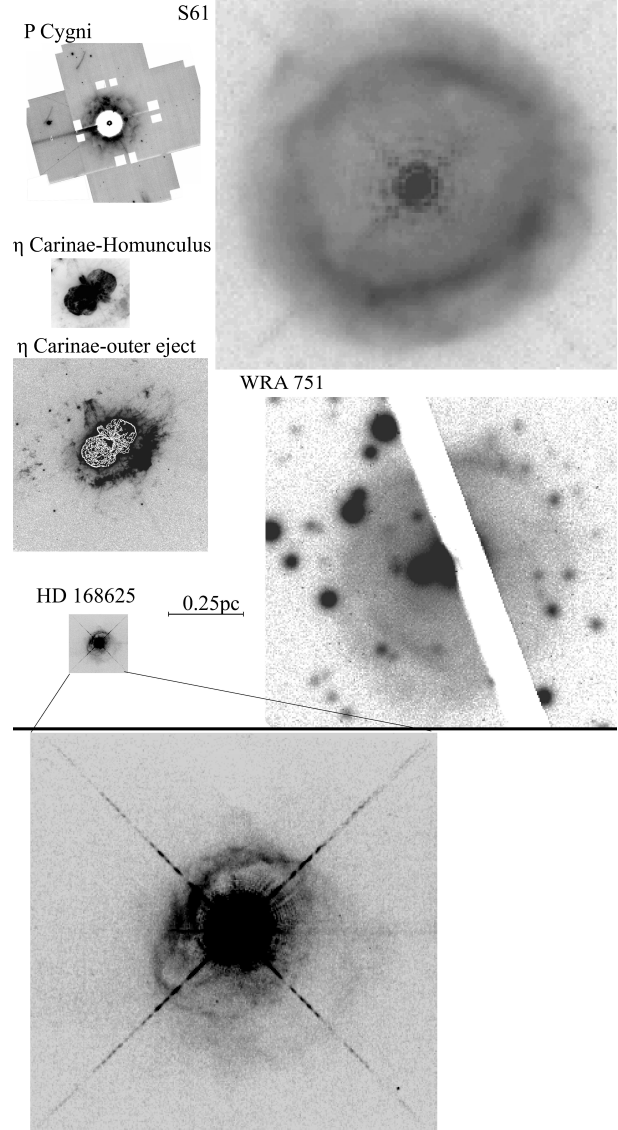


Fig. 1. Top: petite nebulae on scale. Bottom: enlargement of the HD 168625 nebula (HST F656N image).

Further out is the filamentary but bipolar outer ejecta (Weis 2012) it covers a radius of about 0.67 pc and has expansion velocities ranging from several 100 km/s to several 1000 km/s.

**S61:** With a diameter of about 0.85 pc S61 is the smallest LBV nebula in Large Magellanic Cloud (LMC). While the nebulae appears spherical at first an accurate measurement reveals a slight elongation with a larger axis of 0.89 pc and a smaller of 0.82 pc. Noteworthy is also that the brightest part of the nebulae is not as expected for a bubble the outer radius. But diffuse emission surpasses the brighter ring at all sides. The kinematics fits well to a spherical expansion of 27 km/s (Weis 2003).

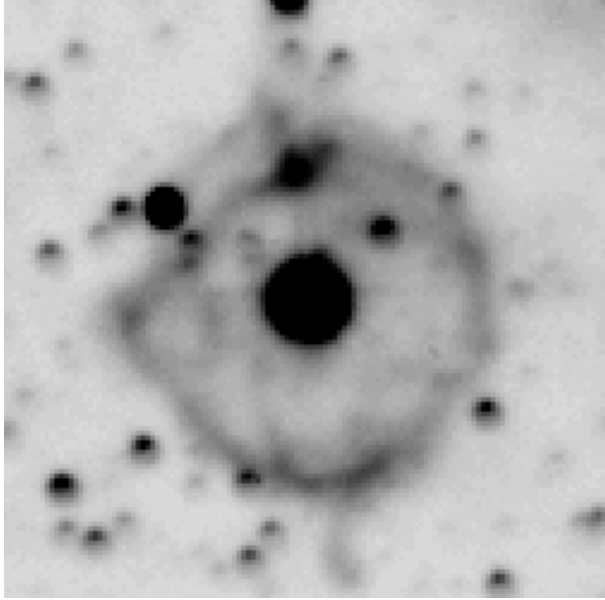


Fig. 2. the Sk -69 279 nebula

#### 4. THE PERSONAL SIDE

Since this conference is also Happy Birthday event I like to add a small personal touch to this text. I met You-Hua being a visiting grad student from the University Heidelberg, Germany. On the long run she became an additional supervisor for my Diploma and PhD theses. For more than 3 years I spent several month per year with her in Illinois and very much enjoyed the time working with her, as well as watching the squirrels.

##### 4.1. *Sk-69 279 - my first astronomical image*

At my starting visit You-Hua gave me an imaging dataset from the LMC. The first data I ever analysed. I opened my first completely reduced image and was surprised by a nice ring nebulae that appeared near the center of the image. I was excited and expected You-Hua to tell me a lot about this object. But she looked astonished at the image and said simply: I have never seen this nebula before. The image of this surprise nebulae is given in Fig. 2 It turned out the central stars is Sk-69 279, an O9f supergiant. That started my astronomical career and long term connection to You-Hua as well as a life long affection for bubbles and circumstellar nebulae. The star was the topic of my Diploma thesis (german analog for Master at that time). Today it is a good

LBV candidate (Weis & Bomans 2020) and like the other LBVs its nebulae shows strong [N II] emission.

##### 4.2. *Sk-69 279 - my first astronomical conference and publication*

The story continued with You-Hua dragging me to a conference and present this discovery in a poster. Furthermore the conference proceedings became my first paper Weis et al. (1995) and was published in RMxAC!

##### 4.3. *Sk-69 279 - scientific results*

My detailed analysis (Weis et al. 1997) of the nebulae shows a sphere with a radius of 4.5 pc. In an echelle long-slit spectrum of the nebulae an expansion ellipse was detected with an expansion velocity of 14 km/s, it further supported the spherical shape. Further observations, in particular additional spectra, revealed more details and deviations from a perfect sphere. We also detected a faint faster outflow to the north (Weis & Duschl 2002).

*Acknowledgements:* Thanks to Dominik Bomans for comments and suggestions. I further thank my thesis advisor Wolfgang Duschl for allowing me to work with You-Hua and spend extended time spans away from Heidelberg. KW acknowledge funding from the German Science Foundation DFG, via the Collaborative Research Center SFB1491 “From Source to Signal”.

#### REFERENCES

- Gaviola, E. 1950, ApJ, 111, 408  
 Ishibashi, K., Gull, T. R., Davidson, K., et al. 2003, AJ, 125, 3222  
 Mahy, L., Hutsemékers, D., Royer, P., & Waelkens, C. 2016, A&A, 594, A94  
 Meynet, G. & Maeder, A. 2005, A&A, 429, 581  
 Weaver, R., McCray, R., Castor, J., Shapiro, P., & Moore, R. 1977, ApJ, 218, 377  
 Weis, K. 2000, A&A, 357, 938  
 ———. 2003, A&A, 408, 205  
 ———. 2011, IAUS, 272, 372  
 ———. Astrophysics and Space Science Library, Vol. 384, Eta Carinae and the Supernova Impostors, ed. K. Davidson R. M. Humphreys, 171  
 Weis, K. & Bomans, D. J. 2020, Galaxies, 8, 20  
 Weis, K., Bomans, D. J., Chu, Y.-H., Joner, M. D., & Smith, R. C. RMxAC, 1995, 3, 273  
 Weis, K., Chu, Y. H., Duschl, W. J., & Bomans, D. J. 1997, A&A, 325, 1157  
 Weis, K. & Duschl, W. J. 2002, A&A, 393, 503

## MIXED MORPHOLOGY SUPERNOVA REMNANTS AND THE CONTRIBUTION OF MARGARITA ROSADO TO THE DETECTION OF EXTENDED X-RAY EMISSION FROM SUPERBUBBLES

Margarita Rosado<sup>1</sup>, Jorge Reyes-Iturbide<sup>1</sup>, Patricia Ambrocio-Cruz<sup>2</sup>, Lorena Arias-Montaña<sup>3</sup>, Ruslan Gabbasov<sup>4</sup>, Isidro Ramirez-Ballinas<sup>1</sup>, and Alejandra Llamas-Bugarin<sup>1</sup>

### RESUMEN

Recordamos la primera propuesta exitosa para detectar emisiones de rayos X de superburbujas empujadas por vientos y la formación de tres astrónomos mexicanos especializados en observaciones de rayos X de fuentes nebulares extendidas. Basándonos en este entrenamiento, damos los resultados de varias propiedades de una clase definida de remanentes de supernova: los remanentes de supernova de Morfología Mixta. Hemos estudiado varios casos en al menos tres dominios de longitudes de onda: radio, rayos X y óptico. Establecemos varias de sus propiedades y favorecemos el modelo de evaporación de nubes densas que sobreviven al choque de supernova utilizando una importante herramienta de modelado.

### ABSTRACT

We recall the memories of the first successful proposal to detect X-ray emission from wind-blown superbubbles and the training of three Mexican astronomers specialized in X-ray observations of extended nebular sources. Based on this training we give the results of several properties of a defined class of supernova remnants: the Mixed Morphology supernova remnants. We have studied several cases in at least three wavelengths domains : Radio, X-rays and Optical. We establish several of their properties and we favor the model of evaporation of dense cloudlets surviving the forward supernova shock using an important modeling tool.

*Key Words:* galaxy: kinematics and dynamics — ISM: bubbles — ISM: kinematics and dynamics — ISM: supernova remnants

### 1. GENERAL

Most of you do not know but I have the honor of having contributed with my small grain of sand to the discovery of X-ray emission from superbubbles. I was a PhD student when my observing proposal with the Einstein Satellite of deep exposures of several superbubbles in the Large Magellanic Cloud including the superbubbles N70 and N185 was accepted. Indeed, at that time I have just measured the high expansion velocities of N70 and N185 by means of Fabry-Perot interferometry (about 70 km/s) and I have computed the X-ray luminosities submitting a proposal to the Einstein Observatory together with my adviser Guy Monnet. The Rosado and Monnet proposal was accepted by Einstein Observatory

board and the observations carried out giving the result of the detection, for the first time, of X-ray emission from the superbubbles N70 and N185, among other superbubbles. We submitted an article reporting those successful results that was rejected by an anonymous referee that argued that it was only noise (at that time the Einstein Observatory instrumental function was concealed for alien users as me, so that it was really hard to answer to the aggressive referee). Years after, our observations were used by You-Hua Chu and Mordecai Mac Low showing that indeed there was X-ray emission from those superbubbles. In fact, bubbles and superbubbles were unexpected objects that successful emit in X-rays besides the binary compact X-ray sources. Thanks to that observing proposal the X-ray emission from superbubbles started to be studied from the X-ray observatories. You-Hua Chu kindly invited Margarita Rosado to collaborate with her on X-ray emission from superbubbles by training three of her students: Patricia Ambrocio-Cruz, Jorge Reyes-Iturbide and Lorena Arias who spent several months at Urbana University learning to reduce X-ray data from You-Hua's team. One of our works, derived from this

<sup>1</sup>Instituto de Astronomía, Universidad Nacional Autónoma de México, Apdo. Postal 70-264, 04510 CDMX, México.

<sup>2</sup>Escuela Superior de Tlahuelilpan, Universidad Autónoma del Estado de Hidalgo, Ex-Hacienda de San Servando Col. Centro, Tlahuelilpan, Hgo. CP 42780.

<sup>3</sup>Universidad Iberoamericana, Prol. Paseo de la Reforma 880, CP 01219, CDMX, México.

<sup>4</sup>Universidad Autónoma Metropolitana, Unidad Azcapotzalco, Av. San Pablo 180, Reynosa Tamaulipas, 02200 CDMX, México.

knowledge, refer to the multiwavelength study of several supernova remnants (SNRs) belonging to a conspicuous class, the Mixed Morphology SNRs .

## 2. MIXED MORPHOLOGY SUPERNOVA REMNANTS

Mixed Morphology Supernova Remnants (MM-SNRs) is a special class of SNRs characterized by being shell-type at radio wavelengths whereas their X-ray emission is filled-center . Other characteristics are their gamma-rays emission (pointing to an association with molecular clouds and thus with core-collapse supernovae progenitors) and a roughly uniform radial distribution of temperature of the hot interior gas. However, it is not well-known how is their optical emission and how to explain their conspicuous morphology and origin.

Regarding the explanation of the properties of MM-SNRs there are two main models:

1. Thermal conduction in the remnant interior (Cox et al. 1999)

Or:

2. Evaporation of dense cloudlets surviving the forward shock, and increasing the gas density at the center (White & Long 1991) (White & Long 1991).

In studying these MM-SNRs we used an important tool, a Python code modeling SNR evolution considering several models. including a clumpy interstellar medium, ISM, equivalent to the second model listed above (Leahy & Williams 2017; Leahy & Ranasinghe 2018; Leahy et al. 2019, 2020).

We are studying several MM-SNRs using mainly archive XMM-Newton X-ray observations and optical spectroscopic and interferometric observations of the optical counterparts of the SNRs.

### 2.1. Determination of MM-SNRs properties from X-ray observations

From archive XMM-Newton X-ray observations we are able of determining the following properties:

- Electron temperature of the hot interior.
- Velocity of the primary shockwave.
- Age of the SNR (together with the linear diameter determination).
- Electron density of the hot interior gas.
- Initial energy deposited in the ISM from the supernova explosion.

### 2.2. Determination of MM-SNRs properties from optical observations

From optical emission line imaging, slit spectroscopy and Fabry-Perot 2D spectroscopy of various emission lines such as  $H_\alpha$ , [SII] and [OIII] being the most important, we can derive:

- Detection of the optical counterpart of the SNRs by means of the high [SII]/ $H_\alpha$  line-ratio..
- Kinematic distance for Galactic SNRs, obtained from the measure of the SNR systemic velocity, equivalent to the SNR’s rotation velocity around the Galactic Center.
- Linear diameter. Mostly derived from radio-shell angular diameter and kinematic distance.
- Electron density of the dense clouds.
- Velocity of the secondary shock induced in the dense cloudlets.

## 3. LIST OF STUDIED MIXED MORPHOLOGY SUPERNOVA REMNANTS

Until now we have studied the following three MM-SNRs:

- SNR 0520-69.4 in the Large Magellanic Cloud galaxy (Ramírez-Ballinas et al. 2020)
- Galactic SNR W51C (Reyes-Iturbide et al. 2022).
- Galactic SNR CTB1 (Reyes-Iturbide et al. 2024).

## 4. CONCLUSIONS

- The three cases of MM-SNRs are consistent with a SN explosion interacting with dense (molecular) cloudlets.
- Under that condition, optical emission should be detected unless high interstellar absorption hide it.
- Optical lines are quite helpful to determine important SNRs quantities, combined with radio and X-rays.

**Acknowledgments:** The authors wish to acknowledge the grant CF- 86367 from CONAHCYT from its financial and academic support. Also, to the staff of San Pedro Mártir Observatory in Baja California, México for their important support during PUMA’s (UNAMS Fabry-Perot observations).

## REFERENCES

- Cox, D. P., Shelton, R. L., Maciejewski, W., et al. 1999, ApJ, 524, 179
- Leahy, D. A. & Williams, J. E. 2017, AJ, 153, 239
- Leahy, D. A. & Ranasinghe, S. 2018, ApJ, 866, 9
- Leahy, D., Wang, Y., Lawton, B., et al. 2019, AJ, 158, 149
- Leahy, D. A., Ranasinghe, S., & Gelowitz, M. 2020, ApJS, 248, 16
- Ramírez-Ballinas, I., Reyes-Iturbide, J., Ambrocio-Cruz, P., et al. 2020, MNRAS, 499, 4213
- Reyes-Iturbide, J., Ramírez-Ballinas, I., Rosado, M., et al. 2022, MNRAS, 516, 6055
- Reyes-Iturbide, J., Ambrocio-Cruz, P., Silva, R., et al. 2024, MNRAS, 527, 803
- White, R. L., & Long, K. S. 1991, ApJ, 373, 543

## FEEDBACK FROM MASSIVE STAR WINDS

J. M. Pittard<sup>1</sup>, M. M. Kupilas<sup>1,2</sup>, C. J. Wareing<sup>1,3</sup>, and S. A. E. G. Falle<sup>3</sup>

### RESUMEN

En esta contribución se revisa el conocimiento teórico actual del impacto que los vientos de estrellas masivas tienen en el medio interestelar (ISM). Dichos viento son potencialmente una importante fuente de momento al medio interestelar, pero en la práctica el aporte de momento depende fuertemente del grado de mezcla entre el material del viento chocado a altas temperaturas y el gas más frío que lo rodea o está embebido en él. Este proceso de mezcla permanece aún poco entendido. Aquí se discuten las diferentes posibilidades que pudieran existir.

### ABSTRACT

Our current theoretical understanding of the impact of winds from massive stars on the interstellar medium (ISM) is reviewed. Such winds have the potential to be a significant source of momentum to the ISM. In practice, the momentum boost is highly sensitive to the degree of mixing between the hot shocked stellar wind material and surrounding or embedded colder gas. This mixing remains an ill-understood process. The range of possibilities that might exist is discussed.

*Key Words:* galaxies: ISM — ISM: bubbles — ISM: kinematics and dynamics — stars: early-type — stars: massive — stars: winds, outflows

### 1. INTRODUCTION

Feedback processes, caused by massive star winds, radiation fields, and supernovae (SNe) are a key requirement of modern galaxy formation and evolution theories. They are necessary in order to obtain the observed galaxy populations, to reduce star formation to the observed rates, and to move gas and metals out of galaxies via galactic winds. Of the three processes noted, SNe are believed to be the dominant stellar input responsible for generating and maintaining the turbulent pressure that regulates the star formation rate within galaxies, and to create the hot phase of the ISM. Without SN feedback, galaxy models form stars too efficiently.

The key parameter for SN feedback is the amount of radial momentum that each supernova remnant (SNR) injects at the end of its life. This determines the amplitude of the turbulent gas motions, which limit gravitational condensation and collapse, and ultimately limits and regulates star formation. However, it has proven tricky to add SN feedback into galaxy and cosmological simulations. Only in the very latest prescriptions has SN-driven feedback become independent of numerical resolution (e.g. the

FIRE-2 algorithm implemented by Hopkins et al. 2018). However, *what* is implemented may still be inaccurate, as simulations have yet to capture the full complexity of real SNRs, including the effect of clustering and multiple SN explosions.

While SNe dominate on large scales, it appears that early (pre-SN) feedback is needed to explain the short feedback timescale required to explain the relative dearth of molecular material around young massive stars (Kruijssen et al. 2019). The relative importance of stellar wind and radiative feedback may further increase if massive stars struggle to explode at all (e.g. Smartt 2015; Sukhbold et al. 2016), or if the stellar initial mass function extends significantly past 100  $M_{\odot}$  (Crowther et al. 2016), is top heavy (Schneider et al. 2018), or non-universal (Yan et al. 2023).

### 2. WIND-BLOWN BUBBLE THEORY

Classical wind-blown bubble (WBB) theory (Pikelner 1968; Dyson & de Vries 1972; Avedisova 1972; Falle 1975) deals with the expansion of an energy-driven bubble in a low-pressure medium with no cooling of the hot interior gas and no mass-loading. In such circumstances, the winds from very massive stars have the potential to inject into the ISM via their WBBs an amount of radial momentum that is comparable to that injected by individual SNRs.

<sup>1</sup>School of Physics and Astronomy, University of Leeds, Leeds, LS2 9JT, UK (j.m.pittard@leeds.ac.uk).

<sup>2</sup>School of Chemistry, University of Leeds, Leeds, LS2 9JT, UK.

<sup>3</sup>Department of Applied Mathematics, University of Leeds, Leeds, LS2 9JT, UK.

### 2.1. Mass-loaded WBBs

Mass-loading of WBBs describes the injection of material into the hot bubble interior from either cold material in the swept-up shell or from cold clouds or clumps in the ambient medium that are over-run as the bubble expands.

The thermal evaporation of mass from the cold dense shell into the hot bubble interior was first studied by Castor, McCray & Weaver (1975) and Weaver et al. (1977). Because cooling at the interface was not considered, only the interior structure of the bubble is altered, and there is no effect on the bubble energetics, expansion rate or radial momentum. If cooling *is* considered, the evaporative mass flux into the bubble interior reduces by a factor of 3 – 30 (El-Badry et al. 2019). However, the energy loss resulting from the cooling reduces the expansion rate and radial momentum of the bubble (the latter by a factor of 2). One caveat is that the simulations by El-Badry et al. (2019) were 1D, so it was not possible to explicitly model the instabilities at the hot-cold interface. Instead, the effects of turbulent mixing and heat diffusion were parameterized with an effective conductivity, and the true value may be greater than supposed.

The effect of mass-loading from overrun embedded clumps on WBBs was first investigated with 1D simulations by Arthur et al. (1993) and Arthur et al. (1996). The injected mass is assumed to be rapidly mixed, and radiative losses at the hot-cold interfaces around the clumps are assumed to be unimportant. This allows the mass-loaded bubbles to maintain interior gas at temperatures in excess of  $10^6$  K (unless the mass-loading is very strong). In these simulations, the global rate of mass injection increases with time, scaling roughly with the volume of the bubble. The models were applied to the Wolf-Rayet ring nebula RCW 58, and were able to reproduce the broad velocity range of the ultraviolet absorption features observed towards the central star.

More recently, Pittard (2022) investigated the behaviour of a WBB subject to mass-loading from embedded clumps where the global rate of mass injection was instead assumed to scale with the mass-loss rate of the star. The amount of mass injection could also be limited by the available reservoir of cold mass. Again, the bubbles were found to maintain hot interiors, and are still able to do significant  $PdV$  work (momentum boost) on the swept-up gas, though are smaller, have less retained energy, and have reduced radial momentum than bubbles without any mass-loading. The assumption of non-radiative mixing interfaces in all three of these works

is likely to lie at the extreme end of possibilities, though remains plausible if the temperature of the interface  $T \lesssim 8000$  K, and/or if the clumps are small (for more details see Pittard 2022).

### 2.2. Multi-dimensional simulations of WBBs

WBBs typically expand into a complex, inhomogeneous environment. Harper-Clark & Murray (2009) posited that in such circumstances the swept-up shell may fracture, allowing hot interior gas to vent out, further reducing the interior pressure and the expansion rate and size of the bubble. Three-dimensional simulations reveal that the shocked wind finds paths of least resistance through the clumpy surroundings, flowing around and past dense clumps which become entrained in the flow (Rogers & Pittard 2013; Dale et al. 2014). The dense clumps are pushed away and are eventually destroyed by the action of the wind(s).

The effect of large-scale magnetic fields on the evolution of a gravitationally bound cloud, star formation, and subsequent stellar wind feedback was investigated by Wareing et al. (2017) and Wareing et al. (2018). If the cloud collapses preferentially along the field lines, the morphology of the background gas and magnetic field can efficiently direct subsequent stellar wind feedback away from denser molecular material. This offers an elegant solution to the “missing wind” problem in the Rosette Nebula (Wareing et al. 2018).

### 2.3. Efficiently-cooling WBBs

Much work in the literature finds that WBBs can efficiently cool (e.g. Geen et al. 2015; Haid et al. 2018), and thus produce little  $PdV$  work. The cooling predominantly occurs at the fractal-like interface between the cooler gas in the shell and hotter gas in the bubble interior, and its rate is dominated by turbulent mixing (Lancaster et al. 2021a,b). Star formation and stellar wind feedback were examined together by Lancaster et al. (2021c). Cooling is found to be very efficient in the denser clouds, but becomes insignificant on cluster scales at later times after most of the gas has turned into stars (cooling may remain significant on larger scales where the swept-up shell exists, but this effect was not captured by this simulation). However, in all these works the mixing rate (and thus cooling) is likely dominated by numerical diffusion, and it remains unclear if WBBs actually cool efficiently.

## 3. SUMMARY AND CONCLUSIONS

Stellar winds and radiation appear to be responsible for clearing molecular gas out of massive star-forming regions. However, the complexity of real

environments means that it is still unclear how efficiently actual stellar wind bubbles cool, and how much  $PdV$  work they can do to boost their radial momentum. These issues are likely to be dependent on the environment, the assumed IMF (e.g. the maximum stellar mass), and the timing (cooling may become ineffective once most of the gas mass has formed stars and/or being expelled from the star forming region). It is likely that there will be significant diversity between one bubble and the next.

A final issue is that not all numerical simulations of stellar wind feedback in the literature had the necessary spatial resolution for the bubble to correctly form and inflate. These bubbles missed their highest pressure phase when young and thus did not achieve their correct radial momentum (for further details see Pittard et al. 2021).

#### REFERENCES

- Arthur S. J., Dyson J. E., Hartquist T. W., 1993, *MNRAS*, 261, 425
- Arthur S. J., Henney W. J., Dyson J. E., 1996, *A&A*, 313, 897
- Avedisova V. S., 1972, *Soviet Ast.* 15, 708
- Castor J., McCray R., Weaver R., 1975, *ApJ*, 200, L107
- Crowther P. A., et al., 2016, *MNRAS*, 458, 624
- Dale J. E., Ngoumou J., Ercolano B., Bonnell I. A., 2014, *MNRAS*, 442, 694
- Dyson J. E., de Vries J., 1972, *A&A*, 20, 223
- El-Badry K., Ostriker E. C., Kim C.-G., Quataert E., Weisz D. R., 2019, *MNRAS*, 490, 1961
- Falle S. A. E. G., 1975, *A&A*, 43, 323
- Geen S., Rosdahl J., Blaizot J., Devriendt J., Slyz A., 2015, *MNRAS*, 448, 3248
- Haid S., Walch S., Seifried D., Wünsch R., Dinnbier F., Naab T., 2018, *MNRAS*, 478, 4799
- Harper-Clark E., Murray N., 2009, *ApJ*, 693, 1696
- Hopkins, P., 2018, *MNRAS*, 477, 1578
- Kruijssen J. M. D., et al. 2019, *Nature*, 569, 519
- Lancaster L., Ostriker E. C., Kim J.-G., Kim C.-G., 2021a, *ApJ*, 914, 89
- Lancaster L., Ostriker E. C., Kim J.-G., Kim C.-G., 2021b, *ApJ*, 914, 90
- Lancaster L., Ostriker E. C., Kim J.-G., Kim C.-G., 2021c, *ApJL*, 922, L3
- Pikelner S. B., 1968, *Astrophys. Lett.*, 2, 97
- Pittard J. M., Wareing C. J., Kupilas M. M., 2021, *MNRAS*, 508, 1768
- Pittard J. M., 2022, *MNRAS*, 515, 1815
- Rogers H., Pittard J. M., 2013, *MNRAS*, 431, 1337
- Schneider F. R. N., et al., 2018, *Science*, 359, 69
- Smartt S. J., 2015, *PASA*, 32, e016
- Sukhbold T., Ertl T., Woosley S. E., Brown J. M., Janka H.-T., 2016, *ApJ*, 821, 38
- Wareing C. J., Pittard J. M., Falle S. A. E. G., 2017, *MNRAS*, 465, 2757
- Wareing C. J., Pittard J. M., Wright N. J., Falle S. A. E. G., 2018, *MNRAS*, 475, 3598
- Weaver R., McCray R., Castor J., Shapiro P., Moore R., 1977, *ApJ*, 218, 377
- Yan Z., Jerabkova T., Kroupa P., 2023, *A&A*, 670, A151

## MULTI-WAVELENGTH OBSERVATIONS OF GALACTIC WINDS

D. J. Bomans<sup>1</sup>

### RESUMEN

En este texto presentaré algunos ejemplos recientes de análisis de múltiples longitudes de onda de enanas con estallidos estelares, con especial énfasis en observaciones del continuo de radio de baja frecuencia y algunos con algunas reminiscencias de mi época de trabajo con You-Hua en UIUC.

### ABSTRACT

In this text I will present a few recent examples of multiwavelength analyses of starburst dwarfs with special emphasis of low frequency radio continuum observations and some with some reminiscences from my time working with You-Hua at UIUC.

*Key Words:* Galaxies: irregular — Galaxies: ISM — Galaxies: magnetic fields — Galaxies: starburst — Galaxies: evolution — radio continuum: galaxies

### 1. BACKGROUND

Galactic scale outflows (when the material stays inside the gravitational well of the galaxies) and galactic winds (when the material escapes into the intergalactic medium) driven by stellar feedback are well established as important processes for the evolution of galaxies (Rupke 2018; Zhang 2018). There is a lot of progress in simulations and observation over the last years, but many questions remain unanswered. Multi-wavelength (or even multi-messenger) observations on galactic winds are critical for the understanding of the complex physics, e.g. when looking at the different situations: stellar wind driven and supernova driven galactic winds, radiation pressure driven winds (AGN or near maximum starbursts), cosmic ray driven winds (with several possible CR transport mechanisms), and intercombination of all the processes. Multi-wavelength observations provide data on structure and kinematics of different gas phases, the relative importance of magnetic fields and dust, as well as the energetic, driving sources, and also the transport mechanisms prevalent for the cosmic rays.

### 2. NGC 4449

While working with You-Hua on the X-ray and H $\alpha$  data of NGC 4449 (Bomans et al. 1997), the possible importance of ordered magnetic fields and cosmic ray feedback in NGC 4449 also became clear (Klein et al. 1996). The creation of strong, ordered magnetic fields is well explained in spiral galaxies by the workings of the  $\alpha\omega$  dynamo (e.g. Beck 2015), ordered magnetic fields in low mass galaxies require

<sup>1</sup>Astronomical Institute, Faculty for Physics & Astronomy, Ruhr University Bochum, Germany.

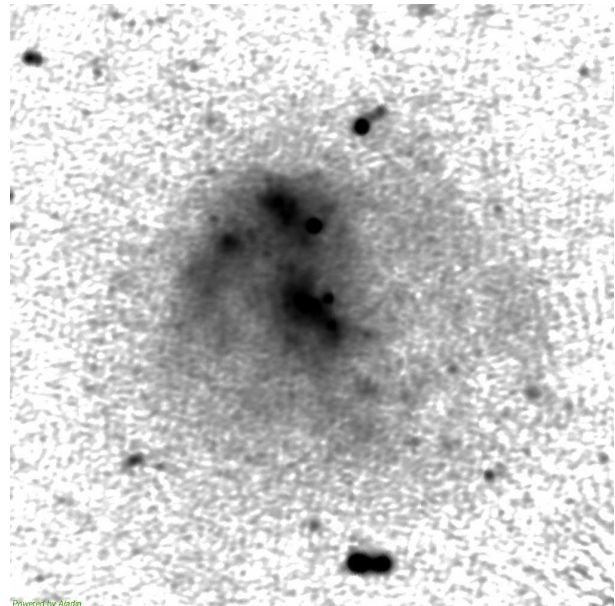


Fig. 1. High resolution (6'') LOFAR 150 MHz image (9'  $\times$  9') of NGC 4449, displayed with logarithmic stretch to show the very extended synchrotron halo of this starbursting irregular galaxy.

different processes, especially a working turbulent dynamo (e.g. Siejkowski et al. 2014). Over the last 20 years more and more observations showed not only ordered magnetic fields inside low mass star forming galaxies, but also in their outflows and winds (e.g. Chyży et al. 2016). With the installation of the LOFAR (LOW Frequency Array) in the Netherlands and several other European countries (notably Germany with 6 stations, and Poland with 3 stations) observations of galaxies at low frequencies ( $\sim 30$  to  $\sim 200$

MHz) with high sensitivity, and high spatial resolution ( $20''$  and  $6''$  at a frequency of 150 MHz) became possible (Heesen et al. 2022). At 150 MHz, the observed emission is dominated by synchrotron emission and is therefore tracing magnetic fields frozen in a thermal plasma and relativistic electrons. In the case of NGC 4449, the LOFAR image (Fig. 1) shows the starforming regions filling the main body of the galaxy (the sites of the freshly accelerated relativistic electrons by supernovae and large scale shocks). Still, it also shows the galactic scale outflow, we previously analyzed at UIUC. The 150 MHz emission correlates well with the large shells and filaments (Bomans et al. 1997; Bomans & Weis 2014), but also show faint, diffuse radio continuum emission well beyond the faintest  $H\alpha$  filaments detected in NGC 4449 (Bomans & Weis 2014).

### 3. MRK 1434

Going from the large irregular galaxy NGC 4449 to a lower mass starbursts, Mrk 1434, is one of the very promising relatively nearby ( $\sim 35$  Mpc distance) laboratories for low metallicity, compact starbursts showing particularly highly ionized emission lines. Based on SDSS data, (Shirazi & Brinchmann 2012) conducted a search for He II emitting galaxies, which resulted in a catalog of 3164 objects, of which 84 star forming galaxies showed nebular He II emission, but no stellar features typical of Wolf-Rayet stars, which are (besides the presence of an AGN) the natural explanation for a hard radiation field in galaxies. So one could speculate that these objects contain very massive, low metallicity stars, making them good proxies for highest redshift galaxies, which recent JWST results on  $z \sim 12$  galaxies seem to support (Topping et al. 2024). We did searches which provided more highly ionized dwarf galaxies and we could show for a new sample, that these galaxies are good candidates for Lyman continuum leakers (Enders et al. 2023), which would make these galaxies also important drivers of reionization. Mrk 1434 is such a proxy galaxy, where we can study the feedback processes in details unobtainable even with JWST. We took a deep spectrum of Mrk 1434 with the LBT MODS spectrograph. Fig. 2 shows an archival HST F606W image which not only shows the red stellar continuum, but clearly the filamentary, bubbly ionized gas emission all over the galaxy and several kpc into the halo, the slit runs through the central region with a position angle of  $45$  deg. The HST image is presented at hard contrast with an inset showing the structure of the brightest emission. A central superbubble and large diffuse

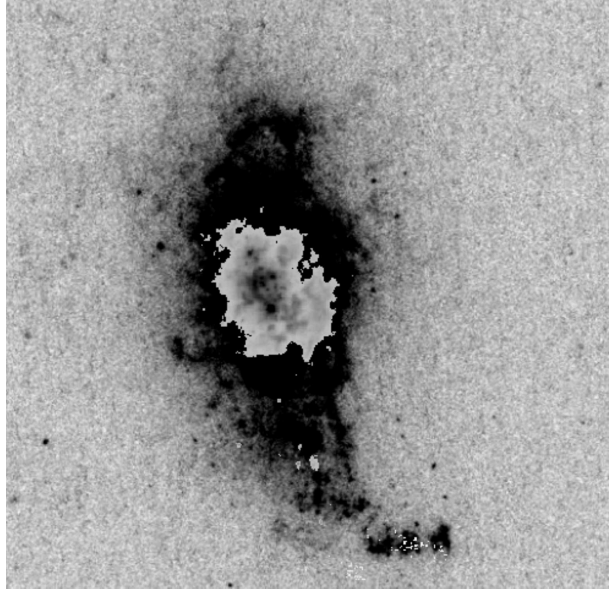


Fig. 2. Section of an archival HST F606W image of Mrk 1434 ( $20'' \times 20''$ ). Together with a hard contrast image to show the faint filamentary emission in the halo, a soft stretch image of the brightest central part of the galaxy is put in to show the central superbubble.

filaments are visible. Fig. 3 shows a small section of the MODS spectrum (the  $H\beta$  line). Two velocity components are needed for a satisfactory fit of the line, implying an outflow with an expansion velocity of  $150 \text{ km s}^{-1}$ . This pattern is also visible in other strong lines. The galaxy also shows soft X-ray emission centered on the superbubble and is detected with LOFAR, implying a complex magnetized superbubble and galactic outflow/wind in the galaxy. Our analysis is still ongoing.

### 4. LARS 14

Making another step into more distant and extreme dwarf starbursts, I picked LARS 14. This member of the “green pea” galaxy class (Cardamone et al. 2009) is the most distant and lowest mass object of the LARS (Lyman Alpha Reference Survey) (Hayes et al. 2013), which used HST to analyze the nature of the Ly $\alpha$  emission of a sample of nearby galaxies. It is also the second strongest Ly $\alpha$  leaker in the sample. Fig. 4 shows an archival HST F390W image of LARS 14 with contours of the LOFAR 150 MHz emission overlaid. LARS 14 is clearly detected and its synchrotron emission appears extended with similar shape and size as the Ly $\alpha$  emission shown in Hayes et al. (2013). Clearly, high resolution radio data are needed, but it is tempting to speculate that LARS 14 is hosting a magnetized outflow. We

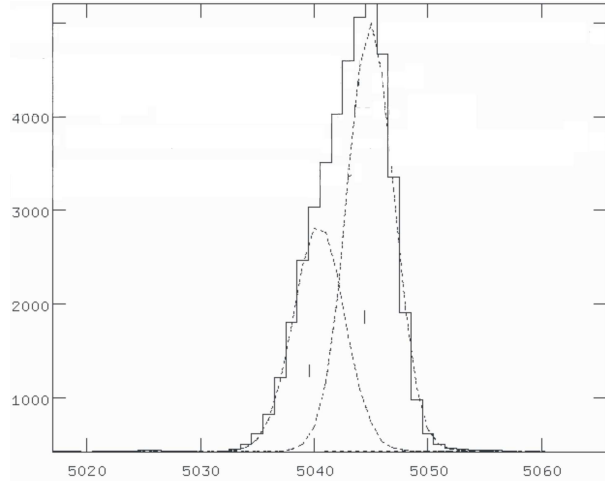


Fig. 3. Section of the MODS spectrum of Mrk 1434 around the  $H\beta$  lines with the two component fit shown. The line split of  $300 \text{ km. s}^{-1}$  together with superbubble seen in the HST image.

currently conducting a larger survey of Green Pea Galaxies with LOFAR and LBT/MODS.

## 5. CONCLUSIONS

The multi-wavelength analysis of low mass galaxies using UV, optical, X-ray and radio-continuum data hold a lot of promise for the understanding of the complex, interwoven processes driving and shaping galactic outflows,  $\text{Ly}\alpha$  and Ly continuum leaking, and chemical evolution. Magnetic fields apparently play a significant role for the structure and dynamics of outflows and galactic winds even for these low and very low mass galaxies. This implies also, that the processes during galaxy formation are even harder to decipher with the current (already beautiful) data of the current generation of telescopes. Even SKA will not change this significantly, so the use of the relatively local, extreme objects as proxies to get detailed physics insights is still highly rewarding.

**Acknowledgements:** Thanks to my PhD students Adam Enders and Sam Taziaux for input to the talk, and Kerstin Weis for commenting on this text. DJB acknowledge funding from the German Science Foundation DFG, via the Collaborative Research Center SFB1491 ‘Cosmic Interacting Matters – From Source to Signal’.

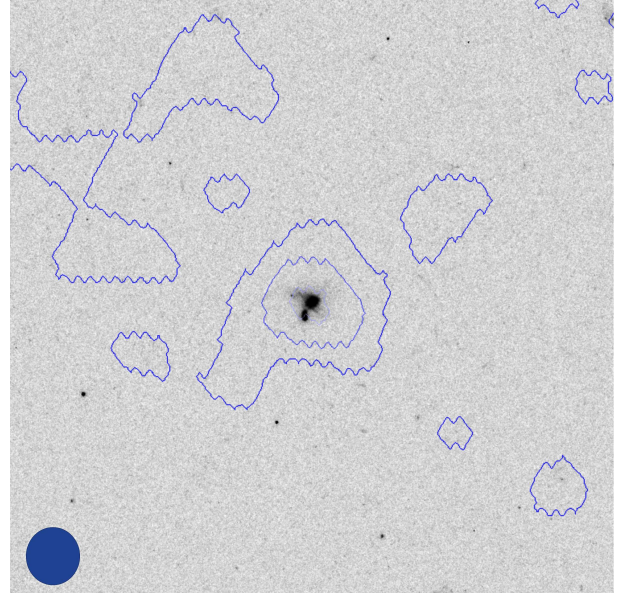


Fig. 4. Archival HST F390W image section ( $45'' \times 45''$ ) of the Green Pea galaxy LARS 14 with the LOFAR 150 MHz contours overlaid. The synchrotron emission is extended (see beam in lower left) and closely resembles the Lyman  $\alpha$  emission of LARS 14.

## REFERENCES

- Beck, R. 2015, *A&A Rev.*, 24, 4  
 Bomans, D. J., Chu, Y.-H., & Hopp, U. 1997, *AJ*, 113, 1678  
 Bomans, D. J. & Weis, K. 2014, *AN*, 335, 99  
 Cardamone, C., Schawinski, K., Sarzi, M., et al. 2009, *MNRAS*, 399, 1191  
 Chyży, K. T., Drzazga, R. T., Beck, R., et al. 2016, *ApJ*, 819, 39  
 Enders, A. U., Bomans, D. J., & Wittje, A. 2023, *A&A*, 672, A11  
 Hayes, M., Östlin, G., Schaerer, D., et al. 2013, *ApJ*, 765, L27  
 Heesen, V., Staffehl, M., Basu, A., et al. 2022, *A&A*, 664, A83  
 Klein, U., Hummel, E., Bomans, D. J., & Hopp, U. 1996, *A&A*, 313, 396  
 Rupke, D. S. N. 2018, *Galaxies*, 6, 138  
 Shirazi, M. & Brinchmann, J. 2012, *MNRAS*, 421, 1043  
 Siejkowski, H., Otmianowska-Mazur, K., Soida, M., Bomans, D. J., & Hanasz, M. 2014, *A&A*, 562, A136  
 Topping, M. W., Stark, D. P., Senchyna, P., et al. 2024, *MNRAS*, 529, 3301  
 Zhang, D. 2018, *Galaxies*, 6, 114

## THE INFLUENCE OF STELLAR CLUSTERS ON PAHS: THE POWER OF JOINT HST/JWST OBSERVATIONS IN NEARBY GALAXIES

D. A. Dale<sup>1</sup> and The PHANGS Team

### RESUMEN

Presentamos las últimas comparaciones de las predicciones teóricas del continuo de polvo y la emisión de hidrocarburos aromáticos policíclicos (PAH) con nuevas observaciones HST+JWST en 19 galaxias cercanas derivadas del proyecto PHANGS. Nuestro análisis se centra en datos de miles de cúmulos estelares compactos y asociaciones estelares. Los resultados iniciales muestran que las distribuciones y tendencias en los colores infrarrojos centrados en los PAH observados generalmente concuerdan con las expectativas teóricas, y que la mayor parte de las observaciones están más alineadas con modelos de PAHs ionizados más grandes.

### ABSTRACT

We present the latest comparisons of theoretical predictions of dust continuum and polycyclic aromatic hydrocarbon (PAH) emission with new HST+JWST observations in 19 nearby galaxies stemming from the PHANGS project. Our analysis focuses on data from many thousands of compact stellar clusters and stellar associations. Initial results show that the distributions and trends in the observed PAH-focused infrared colors generally agree with theoretical expectations, and that the bulk of the observations is more aligned with models of larger, ionized PAHs.

*Key Words:* Galaxies: spiral — open clusters and associations — stars: clusters

### 1. INTRODUCTION

Polycyclic aromatic hydrocarbons (PAHs) are common throughout the interstellar media of galaxies. PAHs exhibit prominent infrared emission features that are sensitive to the shape and intensity of the radiation field that excites these small dust grains. In turn, the PAH features themselves are sensitive to their ionization levels and size distributions. Dale et al. (2023) analyzed PAH band ratios near stellar clusters within PHANGS galaxies NGC 0628, NGC 1365, and NGC 7496. This preliminary effort found evidence for the PAHs to be preferentially larger and more ionized. In the results presented here, we provide the PAH band ratios and their interpretation for all 19 galaxies from the PHANGS Cycle 1 JWST Treasury program (PID 2107; PI J. Lee).

### 2. THE SAMPLE

The galaxies analyzed here are part of the PHANGS JWST Cycle 1 Treasury project (Lee et al. 2023). All 19 are star-forming main sequence galaxies. JWST imaging was obtained for each galaxy in the NIRCam F200M, F300M, F335M, and F360M filters and the MIRI F770W, F1000W, F1130W, and F2100W MIRI filters. Figure 1 shows the sample as observed by JWST.

<sup>1</sup>Department of Physics & Astronomy, University of Wyoming, Laramie, WY 82071 USA (ddale@uwyo.edu).

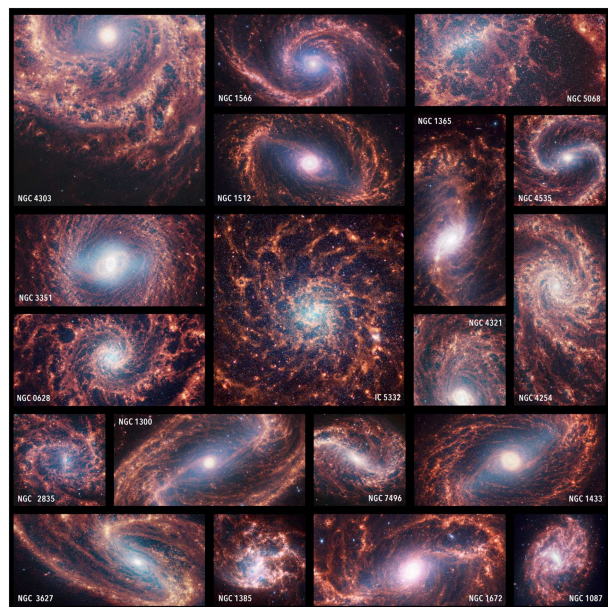


Fig. 1. The PHANGS-JWST Cycle 1 galaxies as seen by NIRCam and MIRI. Image credit: J. Depasquale & A. Pagan (STScI)

Photometry was carried out near the compact Class 1 and 2 stellar clusters (Whitmore et al. 2021; Deger et al. 2022) and stellar associations Larson et al. (2023). Ages and masses for these ob-

jects are based on spectral energy distribution fits to PHANGS-HST photometry (e.g., Turner et al. 2021). We also identified diffuse regions within each galaxy that do not overlap with the stellar clusters or associations, regions that are used to serve as a control sample.

### 3. ANALYSIS

Continuum-subtracted  $3.3\mu\text{m}$  PAH emission is derived following the recipe of Sandstrom et al. (2023). All images at wavelengths shorter than  $11.3\mu\text{m}$  are smoothed to the resolution of the F1130W imaging. Photometry was carried out for each cluster using  $0''.6$  diameter circular apertures. Photometry was also done for each stellar association using the polygons defined in Larson et al. (2023). A signal-to-noise threshold of 5 was employed. In the next section we compare the observed PAH band ratios with those predicted from synthetic spectra derived from the Draine et al. (2021) models using the CIGALE SED fitting software package (Boquien et al. 2019).

### 4. RESULTS

Figure 2 shows the PAH band ratios for the stellar clusters and associations in all 19 JWST-PHANGS Cycle 1 galaxies. Included in Figure 2 is the grid of synthetic points from the models of Draine et al. (2021) described in § 3. The black and grey grids in Figure 2 demonstrate how the synthetic points depend on stellar cluster age, PAH size distribution, and PAH ionization for a fixed radiation field intensity  $U = 1$ . The large arrows and corresponding descriptors indicate how the synthetic PAH feature ratios change for each modeled parameter. The overall distributions of the observed ratios in Figure 2 track well with the grid of synthetic models, and the majority of the observations are consistent with the PAHs having elevated ionization levels and large size distributions. In other words, the data are mostly populating the black grid for larger PAHs (and not the grey grid for smaller PAHs) between the “standard” and “high” ionization model tracks forming the lefthand half of the black grid.

There are no significant differences between the ensemble medians and dispersions for the clusters compared to the associations, but there are some galaxy-to-galaxy differences. For example, most clusters and associations for NGC 1087 appear higher up the black (large PAH) grid, suggestive of dust heating by younger/harder radiation fields. Conversely, nearly all of the data points for

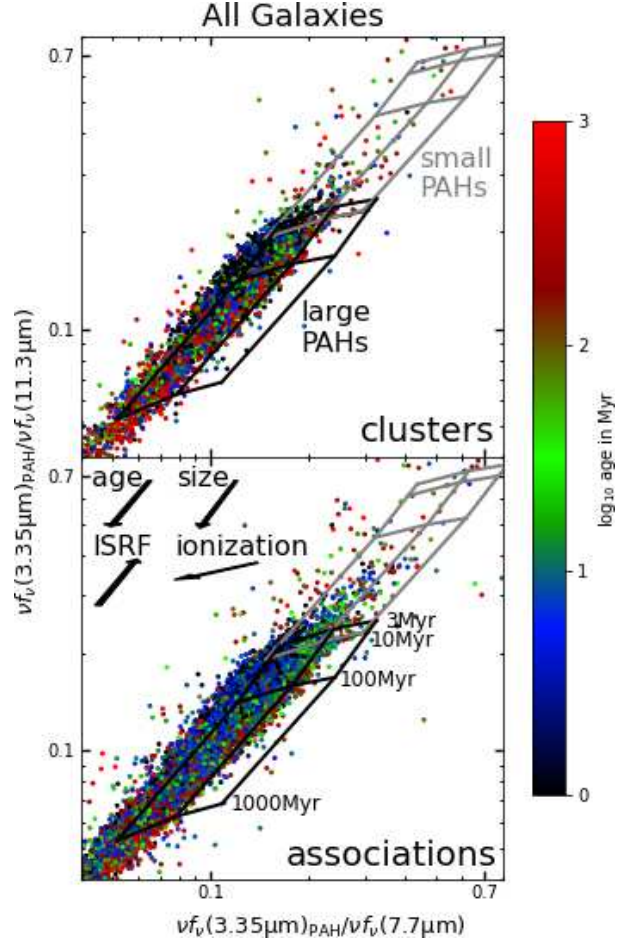


Fig. 2. Top: PAH ratios for stellar clusters in PHANGS-JWST Cycle 1 galaxies. Overlaid tracks show dust emission models from Draine et al. (2021). The grey and black tracks are for small ( $a_{01} = 3 \text{ \AA}$ ) and large ( $a_{01} = 5 \text{ \AA}$ ) modeled PAH distributions, respectively, with both assuming  $\log U=0$ ,  $\text{ion}=0,1,2$ , and  $\text{age}=3,10,100,1000 \text{ Myr}$ . Bottom: The same as the top panel but for stellar associations.

NGC 1365 are shifted down the grid and lie between black model grid lines corresponding to effective stellar population ages of 100 Myr–1 Gyr, indicative of older and/or softer-than-average radiation fields. Interestingly, the median PAH feature ratios for each galaxy trend opposite to expectations when compared against galaxy-integrated offsets from the star-forming main sequence (Leroy et al. 2021) and disk-averaged surface density of the star formation rate (Dale et al. 2024, in prep.).

Figure 3 shows the PAH feature ratios for the selected diffuse regions. In terms of ionization, we find no (leftward) shift of the distribution for diffuse regions with respect to the clusters and associations for

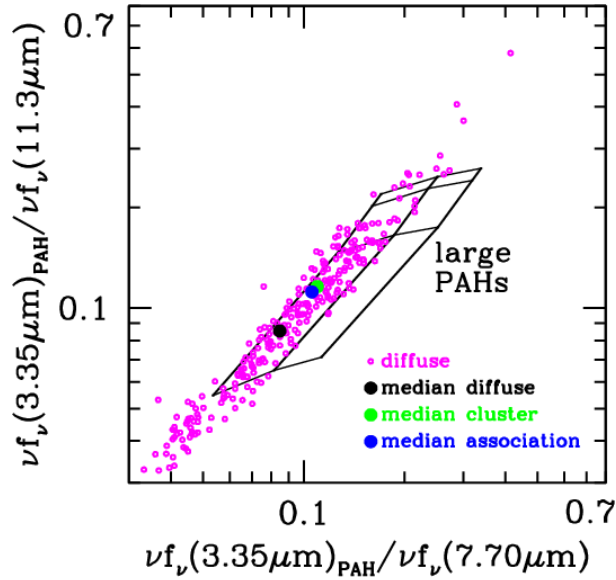


Fig. 3. The median PAH band ratios for clusters (green), associations (blue), and diffuse regions (black). The PAH band ratios for individual diffuse regions are shown in magenta.

diffuse regions. However, the diffuse data points appear to be shifted “down” parallel to the grid. This downward shift can be interpreted as representing radiation fields that are older/softer and/or larger PAH size distributions. The inference of an older/softer radiation field is not unexpected for diffuse regions of the interstellar medium.

## 5. CONCLUSIONS

An update to the PAH band ratio analysis of Dale et al. (2023) is presented here, utilizing all 19 of the galaxies from the JWST Cycle 1 PHANGS Treasury program. The results presented here are consistent with those from Dale et al. (2023): the ensemble of stellar clusters and stellar associations exhibit PAH band ratios that are consistent with ionized and large PAH size distributions. A comparison with PAH band ratios extracted for diffuse regions within each galaxy was also carried out. The PAHs from the diffuse regions show smaller  $3.3\mu\text{m}/7.7\mu\text{m}$  and  $3.3\mu\text{m}/11.3\mu\text{m}$  ratios, consistent with the softer radiation fields expected for such environments. Inspection on a galaxy-by-galaxy basis shows smaller median PAH band ratios for larger spatially-integrated offsets from the star-forming galaxy main sequence and larger disk-averaged star formation rate surface densities. These latter results merit careful study in future efforts.

## REFERENCES

- Boquien, M. et al. 2019, *A&A*, 622, A103  
 Dale, D. A. et al. 2023, *ApJL*, 944, L23  
 Deger, S. et al. 2022, *MNRAS*, 510, 32  
 Draine, B. T. et al. 2021, *ApJ*, 917, 3  
 Larson, K. L. et al. 2023, *MNRAS*, 523, 6061  
 Lee, J. C. et al. 2023, *ApJL*, 944, L17  
 Leroy, A. K. et al. 2021, *ApJS*, 257, 43  
 Sandstrom, K. M. et al. 2023, *ApJL*, 944, L7  
 Turner, J. A. et al. 2021, *MNRAS*, 502, 1366  
 Whitmore, B. C. et al. 2021, *MNRAS*, 506, 5294

## PLANETARY NEBULA IN THE BINARY ERA

Guillermo García-Segura<sup>1</sup>, Ronald E. Taam<sup>2</sup>, and Paul M. Ricker<sup>3</sup>

### RESUMEN

El proyecto que se presenta es un estudio completo de la interacción dinámica que producen la radiación y los vientos estelares con el medio interestelar. Este proyecto está basado en una estrecha comunicación entre dos grandes pilares de la astrofísica moderna: la evolución estelar y la magneto-hidrodinámica, incluyendo una pieza fundamental actual que es la binariedad.

### ABSTRACT

The project presented in this talk is a complete study of the dynamical interaction that produce radiation and stellar winds with the interstellar medium. This project is based on a close communication between two great pillars of modern astrophysics: stellar evolution and magneto-hydrodynamics, including a current fundamental piece that is binarity.

*Key Words:* planetary nebulae — stars: mass-loss, binaries

### 1. INTRODUCTION

Stellar radiation and winds, as well as supernova explosions, have a profound influence on the structure of the surrounding gas, heating it, sweeping it into large shells, and changing its chemical composition. Stars go through phases with very different mass losses during their evolution, producing a wide variety of structures in the surrounding gas. Although this mass loss is in the form of constant winds for most of their lives, the final phase can be a supernova explosion, depending on the initial mass. One result of this long process is the ejection of materials synthesized in nuclear reactions. Such ejections change the abundance of the circumstellar medium, enriching it with heavier elements. The kinetic energy deposited on the medium by massive stars, in turn, is the main source of hot coronal gas in the interstellar medium. The shock waves produced can even induce star formation. Both steady winds and supernova ejections produce shock waves that sweep through the ambient gas, forming ring nebulae (including planetary nebulae) and supernova remnants respectively. An example of the need to take into account the full history of stellar mass loss is the

discovery of the previously formed nebula surrounding the 1987 A supernova.

We have shown in previous works that to understand ring nebulae, the history of the central star must be taken into account (García-Segura et al. 1996a, 1996b). Stellar evolution simply tells us that there are multiple dynamic interactions with the circumstellar medium, the final conditions of a first stage are the initial conditions of a second phase, as can be clearly seen in the case of SN 1987 A. The complete dynamical evolution is a very complex problem.

Although stellar evolution calculations are sufficiently precise to predict a number of observational parameters, such as abundances and surface temperatures, the rate at which mass is lost from the central star is still subject to large uncertainties, especially after the main sequence phase. In previous calculations we (Langer et al. 1999) emphasized that ring nebulae are extremely sensitive to wind speed and mass loss history. The high degree of sensitivity allows us to combine stellar evolution calculations with hydrodynamic studies to verify the structures predicted by the computed mass loss. In other words, by combining stellar evolution with circumstellar evolution, we can visualize the printing of stellar models, and compare directly with observed images.

Stellar evolution was of great importance in the 20th century and laid the foundations for practically all advances in astrophysics. Its interaction with the interstellar medium has been fundamental to understanding many of the very important observations for modern cosmology, such as all types of super-

<sup>1</sup>Instituto de Astronomía, Universidad Nacional Autónoma de México, Km. 107 Carr. Tijuana-Ensenada, 22860, Ensenada, B. C., México.

<sup>2</sup>Center for Interdisciplinary Exploration and Research in Astrophysics (CIERA), Department of Physics and Astronomy, Northwestern University, 2145 Sheridan Road, Evanston, IL 60208, USA.

<sup>3</sup>Department of Astronomy, University of Illinois, 1002 W. Green St., Urbana, IL 61801, USA.

novae with their brightness decay, especially due to the interaction with the circumstellar medium, especially SN Ia and gamma-ray burst among other objects that can or could be used as distance indicators.

However, these studies focused primarily on the stellar evolution of isolated stars. Already in the 21st century, it has become clear that almost all important events have to include binarity in their work schemes. For example, LIGO detections are unthinkable if there is no common envelope evolution in stars, which give way to mergers of stellar black holes (BH-BH), neutron stars (NS-NS), combinations of these (BH-NS), and recently the SN Ia candidates from white dwarf mergers (WD-WD). Thus, we see, for example, that the study of common envelope evolution has become of vital importance for astrophysics, and yet, this phenomenon is not observed directly, since it is very difficult statistically to observe it by its short duration.

What can be easily observed are the nebulae that form after the common envelope evolution process, and it is here where planetary nebulae take on a unique role, due to their large number. Every day more and more short period binary stars (hours, days) are confirmed in planetary nebulae, in addition to hydrodynamic studies, teaching us that only with common envelope evolution is it possible to explain their morphology. For example, to explain the planetary nebula NGC 3231 recently observed with the James Webb Space Telescope (De Marco et al. 2022), a system of four stars is needed (two of them produce a common envelope evolution). Even now the need for a binary process to explain the formation of the Homunculus, the nebula surrounding Eta Carina, is debated.

Another important point is that the great advances in the 20th century were made by the magnificent resolution of the HST in the optical regime, vital for observing large objects in the interstellar medium. But with the arrival of ALMA and the James Webb Space Telescope, we can now reach unimaginable resolutions in millimeter and infrared, and these new observations are being key in understanding many events close to the stars that are engulfed by dust, since the majority of common envelope events occur in the red super giant phases (RSG) and in the asymptotic giant branch (AGB). For example, ALMA observations of water fountains involving AGB stars, are revealing the very early stages of proto-planetary nebulae, with the formation of accretion disks and jet launches, such as the case of W43A (Tafoya et al. 2020).

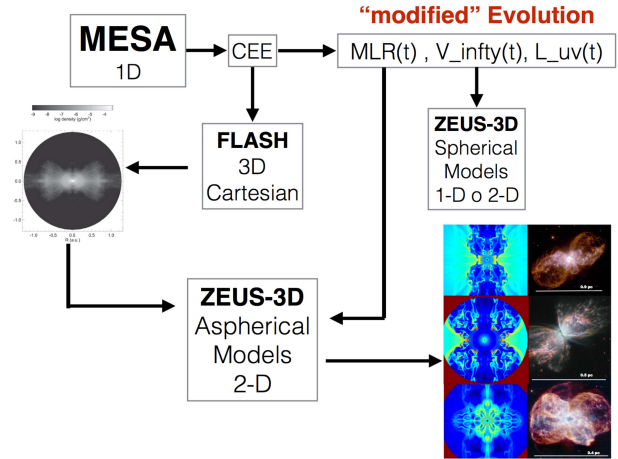


Fig. 1. Working scheme showing the different used codes

## 2. GOALS OF OUR PROJECT

It is proposed to study the dynamical interaction of radiation and stellar mass loss with the circumstellar medium using numerical methods, including the effects of binaries. The project contemplates the computation of stellar evolution models using MESA, for a whole range of initial stellar masses, between low-mass stars that are precursors of planetary nebulae and massive stars that form Wolf-Rayet ring nebulae and blue luminous variables (LBV), as well as the respective hydrodynamical calculations of the gas response around such stars, especially the hydrodynamic calculations of the common envelope events. The direct and indirect results from the MESA stellar evolution code, such as ionizing photons, wind speeds and stellar mass loss-rates, will be used as internal boundary conditions for the magnetohydrodynamics models, using the ZEUS-3D code (see Figure 1). All this including binary as a new ingredient. In turn, MESA models are used to calculate the stellar structure at the time of the common envelope evolution event. The 1-D radial structure is extrapolated into 3-D in FLASH in Cartesian coordinates (Ricker& Taam 2012). As we already did in our recent articles (García-Segura et al. 2018, 2020, 2021, 2022), FLASH’s 3-D Cartesian results are averaged in 2-D spherical coordinates, which are what we use in ZEUS. Note that the FLASH models are computationally very expensive. However, they are not able to follow the ejection of the envelope for a long time, only for a few tens or hundreds of years. That is why, to follow the expansion for thousands of years, typically of planetary nebulae, we use 2-D expanding grids in ZEUS. This way of working is precisely what has made us pioneers in the computation of planetary nebulae that come from a common

envelope evolution, since otherwise, the computation is prohibitive and inefficient.

### 3. FIRST PROJECTED CALCULATIONS

The fragmentation of planetary nebulae has been a recurring theme in several of our previous works. We have shown that photoionization is the most effective method for breaking up nebulae when the shells are partially opaque to ionizing radiation. Recently, the fragmentation produced by the photoionization front has served to explain the James Webb Space Telescope observations of the planetary nebula NGC 3132, and the formation of the molecular “spikes” observed in Molecular Hydrogen. Our hydrodynamic simulations included in this study gave an explanation of the molecular structures in De Marco et al. (2022). Since new observations from the James Webb Space Telescope are showing structures never seen before in the near and mid-infrared, in the first study we will focus on the fragmentation of planetary nebulae, emphasizing the molecular structures that are observed and would be observed in the shadows of the clumps due to lack of photoionization, especially in the phases of stellar evolution when the stars enter in the cooling track towards white dwarfs. This has not yet been well studied. To do this, we will use the models for single stars of 1, 1.5, 2, 2.5, 3.5 and 5 solar masses, and we will calculate the emissions in molecular Hydrogen in the fragmented phases. Later we will confront these models with new ones that include the common envelope phase. The difference between the latter lies in the fact that the expulsion of the AGB envelope is violent and sudden compared to the slow and gradual ejection of isolated stars, considerably increasing the circumstellar density very close to the central star, with much larger opacities. A specific goal would be to measure the molecular mass in the simulations, since this is difficult to do in the observation of molecular Hydrogen.

There are still important questions in common envelope evolution. For example, the efficiency of envelope ejection and the role played by recombination energy, the effects of convection in the circumbinary bound gas, and the role of the mass ratio of the stars in the final morphology of nebulae. It is unknown what the survival time of the circumstellar and circumbinary disks that originate magnetic jets and winds is, and what are the true causes for the formation of nebulae with point symmetry. It is also unknown how long the “Roche-Lobe-Overflow” phase usually lasts prior to the evolution of the common envelope. These and many other questions will be addressed in this project.

**Acknowledgments:** We thank Michael L. Norman and the Laboratory for Computational Astrophysics for the use of ZEUS-3D. The computations were performed at the Instituto de Astronomía-UNAM at Ensenada. Partial support for this work is been provided by PAPIIT-IG101223 grant, and NSF through grants AST-0200876 and AST-0703950.

### REFERENCES

- De Marco, O., Akashi, M., Akras, S., et al. 2022, *NatAs*, 6, 1421
- García-Segura, G., Langer, N., & Mac Low, M. -M. 1996, *A&A*, 316, 133
- García-Segura, G., Mac Low, M. -M., & Langer, N. 1996, *A&A*, 305, 229
- García-Segura, G., Ricker, P. M., & Taam, R. E. 2018, *ApJ*, 860, 19
- García-Segura, G., Taam, R. E., & Ricker, P. M. 2020, *ApJ*, 893, 150
- García-Segura, G., Taam, R. E., & Ricker, P. M. 2021, *ApJ*, 914, 111
- García-Segura, G., Taam, R. E., & Ricker, P. M. 2022, *MNRAS*, 517, 3822
- Langer, N., García-Segura, G., & Mac Low, M. -M. 1999, *ApJ*, 520, L49
- Ricker, P. M. & Taam, R. E. 2012, *ApJ*, 746, 74
- Tafoya, D., Imai, H., Gomez, J. F., et al. 2020, *ApJ*, 890, 14

## COMMON ENVELOPE SHAPING OF PLANETARY NEBULAE

Shiau-Jie Rau<sup>1</sup> and Paul M. Ricker<sup>1</sup>

### RESUMEN

La evolución de envoltura común ocurre cuando una estrella en un sistema binario llena de manera inestable su lóbulo de Roche y la órbita de la otra estrella colapsa en la envoltura extendida. Este proceso normalmente provoca la expulsión de la envoltura, lo que lleva a una binaria cercana o a una fusión estelar. La envoltura que sale no es simétrica, por lo que puede romper la simetría de cualquier viento posterior más rápido, como el producido durante la fase de nebulosa planetaria. Trabajos anteriores han demostrado que el material denso expulsado en la fase de envoltura común puede explicar la forma bipolar de tales nebulosas. Para estudiar este proceso, hemos producido dos sistemas progenitores de nebulosas planetarias de envoltura común. Cada uno entra en una evolución de envoltura común en una fase evolutiva diferente con una cantidad diferente de energía de recombinación disponible. Esto puede ayudarnos a comprender cómo la energía de recombinación afecta la evolución de las nebulosas planetarias.

### ABSTRACT

Common envelope evolution occurs when one star in a binary system unstably fills its Roche lobe, and the other star's orbit shrinks into the expended envelope. This process typically causes the ejection of the envelope, leading to a close binary or stellar merger. The outflowing envelope is not symmetrical, so it may break the symmetry of any subsequent faster wind, such as that produced during the planetary nebula phase. Previous work has shown that the dense material ejected in the common envelope phase can explain the bipolar shape of such nebulae. To study this process, we have produced two common-envelope progenitor systems of planetary nebulae. Each enters common envelope evolution at a different evolutionary phase with a different amount of available recombination energy. This can help us understand how recombination energy affects the evolution of planetary nebulae.

*Key Words:* methods: numerical — stars — stars: binaries: close

### 1. INTRODUCTION

During the evolution of a binary star system, if one of the stars fills its Roche lobe, intense mass transfer between the two stars could occur. This mass transfer can cause angular momentum loss from the system. Once the more compact companion star's orbit shrinks into the other star, they share the same envelope. This situation, in which the two stars share their envelope and evolve together, is called common envelope evolution (CEE) (Ivanova et al. 2020).

In the late stages of stellar evolution, low-mass stars eject their envelopes. The ejected envelope forms a shell of ionized gas known as a planetary nebula. Under this simple scenario, the shapes of planetary nebulae are expected to be roughly spherical or ellipsoidal. However, some of them are bipolar or barrel-type shapes. To produce this kind of shape, a slow, dense wind in the equatorial plane is needed.

Common envelope evolution is an efficient way to produce this wind (García-Segura et al. 2018).

In this project, by setting up common envelope simulations for a model with a  $2.5 M_{\odot}$  primary star during its pre-main sequence (pre-MS) phase and a  $0.36 M_{\odot}$  white dwarf (WD), we produce 2 kinds of progenitor system for planetary nebulae. One enters common envelope evolution with a  $2.49 M_{\odot}$  red giant (RG) plus a  $0.36 M_{\odot}$  white dwarf; the other enters common envelope evolution with a  $2.48 M_{\odot}$  early-AGB star (EAGB) plus a  $0.36 M_{\odot}$  white dwarf.

### 2. MODELS

To produce the progenitor systems for planetary nebulae after common envelope evolution, we start from stellar evolution models using MESA (version 15140; Paxton et al. 2011, 2013, 2015, 2018, 2019; Jermyn et al. 2023), and perform 3D hydrodynamic simulations using FLASH4 (Fryxell et al. 2000; Dubey et al. 2008). Since the 1D MESA single star model is spherically symmetric but the binary system is not, we also use SPHARG (Ricker et al., in

<sup>1</sup>Department of Astronomy, University of Illinois, 1002 W. Green St. Urbana, IL 61801, USA

TABLE 1  
MODELS WE CONSIDERED

Model	2.5RG+0.36WD	2.5EAGB+0.36WD
$M_{\text{WD}}$	$0.36M_{\odot}$	$0.36M_{\odot}$
$M_{\text{p},0}$	$2.50M_{\odot}$	$2.50M_{\odot}$
$M_{\text{p,CE}}$	$2.49M_{\odot}$	$2.48M_{\odot}$
$a_{\text{init}}$	$64.2R_{\odot}$	$67.7R_{\odot}$
$M_{\text{c,He}}$	$0.344M_{\odot}$	$0.501M_{\odot}$
$M_{\text{c,C/O}}$	—	$0.354M_{\odot}$

$M_{\text{WD}}$ : secondary white dwarf star mass;  $M_{\text{p},0}$ : pre-main sequence mass for the primary star;  $M_{\text{p,CE}}$ : primary star mass when entering common envelope evolution;  $a_{\text{init}}$ : initial separation;  $M_{\text{c,He}}$ : helium core mass;  $M_{\text{c,C/O}}$ : carbon/oxygen core mass.

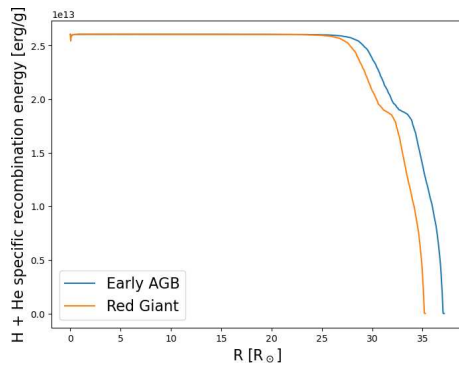


Fig. 1. Hydrogen and helium recombination energy for the initial models.

prep; Faber et al. 2010), a Smoothed Particle Hydrodynamics (SPH) code, to relax the single star model into a non-spherically symmetric binary star potential.

The two models we consider both start with a  $2.5 M_{\odot}$  single pre-main sequence star. We choose different stages for it to enter common envelope evolution. One enters the common envelope stage when it is a red giant (model 2.5RG+0.36WD), and the other enters common envelope evolution when it is an early-AGB star (model 2.5EAGB+0.36WD). The detailed properties for these two models are shown in Table 1. We terminate these simulations when we can no longer resolve the motions of the stellar cores.

Fig. 1 shows the initial recombination energy ( $E_{\text{rec}}$ ) profile for the two donor stars. We can see that the RG and EAGB donor stars contain different recombination energies, and the 2.5EAGB+0.36WD case initially carries more since the EAGB donor star has a higher envelope temperature compared to the RG donor. Since recombination energy could be released during the common envelope phase, we expect it will affect the system evolution.

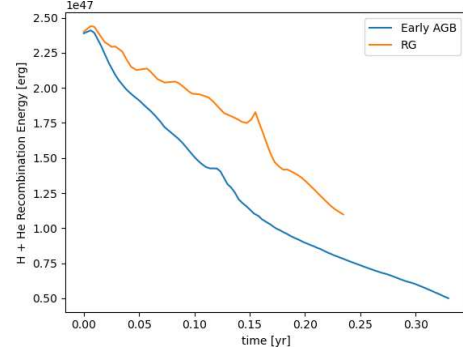


Fig. 2. Hydrogen and helium recombination energy evolution of the two models.

### 3. RESULTS

From Fig. 2 we can see that the EAGB case releases the recombination energy faster than the RG case. The EAGB donor has a lower envelope density; thus its envelope gas is more ready to be ejected. As the envelope is ejected more rapidly, the temperature also drops more quickly, so the EAGB recombination energy is released more quickly than for the RG. Comparing Fig. 3 and Fig. 4, we can see that the EAGB case shows a faster ejection of its envelope. Fig. 5, which displays the final azimuthally averaged density, shows that in the RG case, the envelope is also more equatorially concentrated than for the EAGB case.

### 4. DISCUSSION

Our simulations show that the donor star's evolutionary stage when the binary system enters common envelope evolution will cause different density distributions around the cores. These differences will potentially affect how the gas ejects during the planetary nebula phase, then lead to different shapes of planetary nebula. Although detailed post-processing hydrodynamics simulations focusing on planetary nebula phase expansion are needed to study the final morphology, our current results already show some differences. Previous studies (García-Segura et al. 2018, 2021, 2022) have shown that common envelope evolution plays an important role in the geometry of planetary nebula. Our results could provide a more robust initial condition for similar simulations.

### 5. CONCLUSIONS AND FUTURE WORKS

Based on our current models, we could investigate the influence of different common envelope evolution tracks on shaping planetary nebulae. To understand this process better, a post-common envelope evolution simulation that can trace that outflowing gas to a distance of a few parsecs is

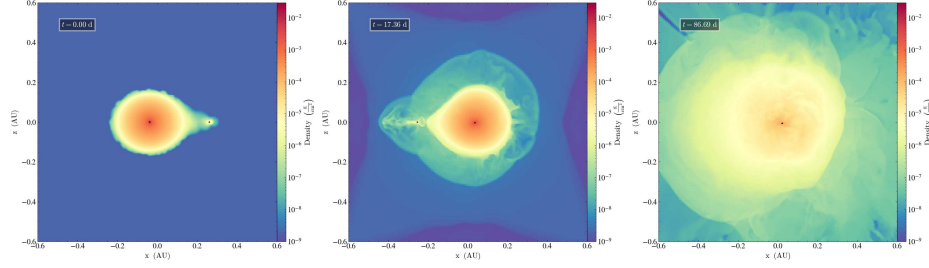


Fig. 3. Model 2.5RG+0.36WD density slice perpendicular to the orbital plane.

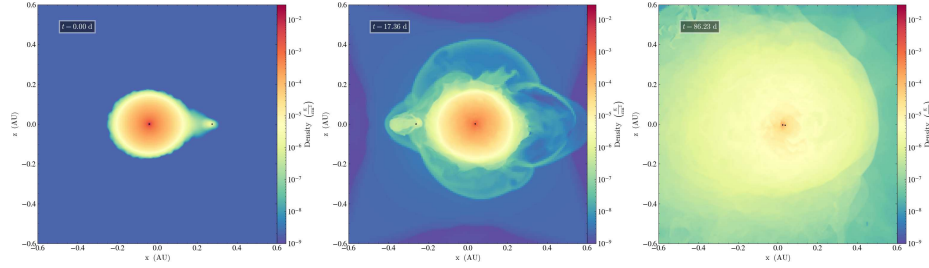


Fig. 4. Model 2.5EAGB+0.36WD density slice perpendicular to the orbital plane.

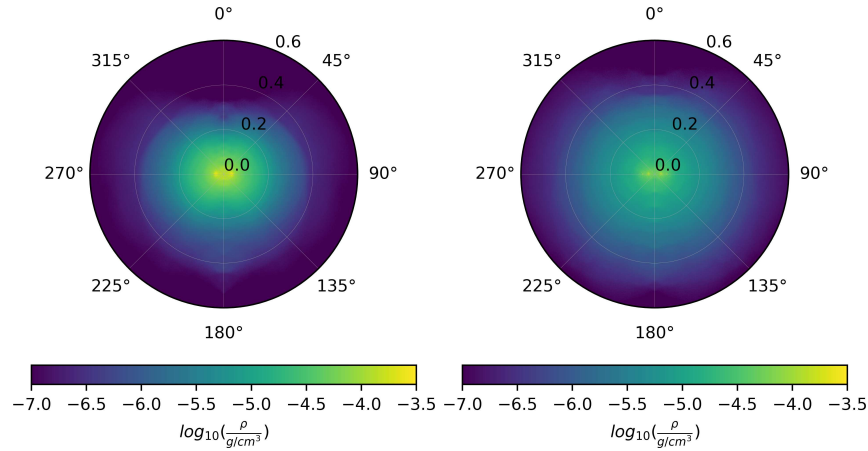


Fig. 5. Azimuthally averaged density distribution. Left panel: 2.5RG+0.36WD; Right panel: 2.5EAGB+0.36WD.

needed. Including magnetic field and radiation diffusion could also be important.

## REFERENCES

- Ivanova, N., Justham, S., & Ricker, P. 2020, AAS-IOP Astronomy Book Series, IOP Publishing, Online ISBN: 978-0-7503-1563-0 Print ISBN: 978-0-7503-1561-6. doi:10.1088/2514-3433/abb6f0
- García-Segura, G., Ricker, P. M., & Taam, R. E. 2018, *ApJ*, 860, 19. doi:10.3847/1538-4357/aac08c
- García-Segura, G., Taam, R. E., & Ricker, P. M. 2021, *ApJ*, 914, 111, doi:10.3847/1538-4357/abfc4e
- García-Segura, G., Taam, R. E., & Ricker, P. M. 2022, *MNRAS*, 517, 3822, doi:10.1093/mnras/stac2824
- Paxton, B., Bildsten, L., Dotter, A., et al. 2011, *ApJS*, 192, 3, doi:10.1088/0067-0049/192/1/3
- Paxton, B., Cantiello, M., Arras, P., et al. 2013, *ApJS*, 208, 4, doi:10.1088/0067-0049/208/1/4
- Paxton, B., Marchant, P., Schwab, J., et al. 2015, *ApJS*, 220, 15, doi:10.1088/0067-0049/220/1/15
- Paxton, B., Schwab, J., Bauer, E. B., et al. 2018, *ApJS*, 234, 34, doi:10.3847/1538-4365/aaa5a8
- Paxton, B., Smolec, R., Schwab, J., et al. 2019, *ApJS*, 243, 10, doi:10.3847/1538-4365/ab2241
- Jermyn, A. S., Bauer, E. B., Schwab, J., et al. 2023, *ApJS*, 265, 15, doi:10.3847/1538-4365/acaed8
- Fryxell, B., Olson, K., Ricker, P., et al. 2000, *ApJS*, 131, 273, doi:10.1086/317361
- Dubey, A., Reid, L. B., & Fisher, R. 2008, *Physica Scripta Volume T*, 132, 014046, doi:10.1088/0031-8949/2008/T132/014046
- Faber, J., Lombardi, J., & Rasio, F. 2010, *Astrophysics Source Code Library*. ascl:1010.074

## THE EXTREMELY YOUNG PLANETARY NEBULA M 3-27

Francisco Ruiz-Escobedo<sup>1</sup>, Miriam Peña<sup>1</sup>, and Ana Valeria Beltrán-Sánchez<sup>1</sup>

### RESUMEN

En esta memoria presentamos resultados parciales del análisis espectrofotométrico de la joven nebulosa planetaria M 3-27. Las líneas de H<sup>+</sup> tienen perfiles y velocidades radiales diferentes a las líneas de los demás iones, lo cual sugiere que son emitidas por la estrella central; debido a esto, la corrección por enrojecimiento se determinó utilizando las líneas de He<sup>+</sup>. Encontramos la presencia de una zona interna de alta densidad electrónica (10<sup>7</sup> cm<sup>-3</sup>) que dificulta el cálculo de la temperatura electrónica. Calculamos las abundancias iónicas relativas a He<sup>+</sup>, que se escalaron para obtener las abundancias iónicas relativas a H<sup>+</sup>, así como las abundancias totales.

### ABSTRACT

In this proceeding we present partial results of the spectrophotometric analysis of the young planetary nebula M 3-27. The H<sup>+</sup> lines have different profiles and radial velocities than the lines of the other ions, suggesting that they are emitted from the central star. Therefore, the correction for reddening was determined using the He<sup>+</sup> lines. We find the presence of an internal zone with a high electron density (10<sup>7</sup> cm<sup>-3</sup>), which complicates the calculation of the electron temperature. We calculated ionic abundances relative to He<sup>+</sup>, which were then escalated to obtain ionic abundances relative to H<sup>+</sup>, as well as total abundances.

*Key Words:* ISM: abundances — ISM: kinematics and dynamics — planetary nebulae: individual: M 3-27

### 1. INTRODUCTION

Planetary nebulae (PNe) represent one of the last evolutionary stages of low-intermediate initial mass stars ( $\sim 1 - 8 M_{\odot}$ ). These objects are constituted by shells of gas expanding around a central star, which emits UV photons that ionize the gas. Emission lines of different ions, produced by various mechanisms, are detected in PNe spectra, such as collisionally excited lines (CELs) and optical recombination lines (ORLs).

Physical conditions of PNe, electronic temperature ( $T_e$ ) and electronic density ( $n_e$ ), can be inferred from different CELs and ORLs ratios, e.g.,  $n_e$  from [S II]  $\lambda\lambda 6731/6716$  and O II  $\lambda\lambda 4649/4661$ ,  $T_e$  from [O III]  $\lambda\lambda(5007 + 4959)/4363$  and He I  $\lambda\lambda 7281/6678$ . Once physical condition are determined, ionic abundances ( $X^{+i}/H^{+}$ ) and total abundances of an element ( $X/H$ ) are calculated.

M 3-27 is a young and compact PN, whose behaviour has been analysed since the late 1960s. Kohoutek (1968), Adams (1975), Ahern (1978) and Barker (1978) found that M 3-27 exhibits a density gradient, with an outer zone where  $n_e \sim 10^3 - 10^4$  cm<sup>-3</sup>, an inner zone where  $n_e \geq 10^6$  cm<sup>-3</sup>, and H I Balmer lines are affected by self-absorption. Wes-

son et al. (2005) estimated a  $T_e = 13,000$  K and determined ionic and total abundances. Miranda et al. (1997) reported that H $\alpha$  has different profile and velocity than CELs: H $\alpha$  exhibits a P-Cygni profile, attributed to a strong stellar wind, and broad and extended wings up to 1500 km s<sup>-1</sup>, attributed to Rayleigh-Raman photon scattering (Arrieta & Torres-Peimbert 2003).

In this proceeding, we present partial results of our analysis of M 3-27, complete results are presented and discussed in detail in the published paper Ruiz-Escobedo et al. (2024).

### 2. OBSERVATIONS

For this work, we analysed a set of optical spectra of M 3-27 obtained using Boller & Chivens and REOSC-Echelle spectrographs, which were attached to the 2.1-m telescope at Observatorio Astronómico Nacional San Pedro Mártir (OAN-SPM), Mexico, from 2004 to 2022. Boller & Chivens (B&Ch) spectra (2004 and 2021) provide a spectral resolution of  $R = 685$  at 5000 Å. REOSC-Echelle spectra (2004, 2019, 2021 and 2022), provide spectral resolutions between  $R \sim 16,000 - 18,000$  at 5000 Å. These spectra were reduced following the standard routines in IRAF<sup>2</sup> and were calibrated in wavelength and flux.

<sup>1</sup>Instituto de Astronomía, Universidad Nacional Autónoma de México, Apdo. Postal 70264, Ciudad Universitaria, 04510, Ciudad de México, México (fdruiz, miriam, avbeltran@astro.unam.mx).

<sup>2</sup>IRAF is distributed by the National Optical Observatory, which is operated by the Associated Universities for Research in Astronomy, Inc., under contract to the National Science Foundation.

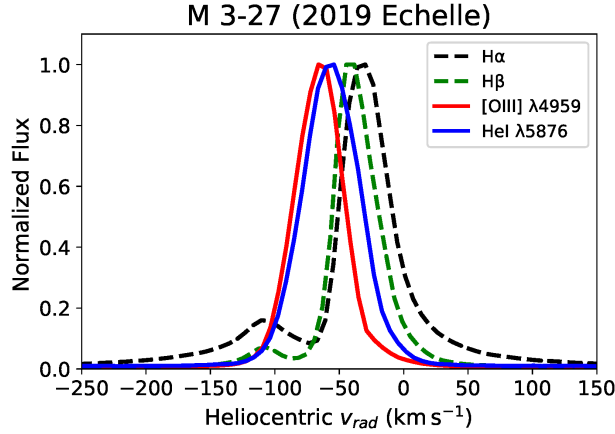


Fig. 1. Profiles and  $v_{\text{rad}}$  of important lines. (Reproduced from Figure 4 in Ruiz-Escobedo et al. (2024)).

### 3. ANALYSIS

#### 3.1. Line profiles

We were able to analyse the line profiles from our REOSC-Echelle spectra due to their high-resolution. In Figure 1, we present the heliocentric radial velocities ( $v_{\text{rad}}$ ) of  $\text{H}\alpha$ ,  $\text{H}\beta$ ,  $\text{He I } \lambda 5876$ , and  $[\text{O III}] \lambda 4959$  lines as observed in REOSC-Echelle 2019 spectrum. We found that  $\text{He I } \lambda 5876$  and  $[\text{O III}] \lambda 4959$  lines have a  $v_{\text{rad}} \sim -70 \text{ km s}^{-1}$  and show a single profile, however,  $\text{H}\alpha$  and  $\text{H}\beta$  lines exhibits a P-Cygni profile with two emission peaks, one blue at  $-84 \text{ km s}^{-1}$  and another red at  $-7 \text{ km s}^{-1}$ . Both H I lines also show an absorption that fits in velocity with He I and  $[\text{O III}]$  line profiles.  $\text{H}\alpha$  profile exhibits wide wings that extends up to  $1,500 \text{ km s}^{-1}$  attributed to Raman scattering. These characteristics were found in all the REOSC-Echelle spectra, indicating that H I lines are affected by stellar emission, which cannot be subtracted, whereas the lines of other ions are emitted by the nebula.

#### 3.2. Reddening correction

Because of the stellar contribution to H I lines, the extinction correction of M 3-27 was performed using He I lines. For this purpose, we used the methodology proposed by Zamora et al. (2022) based on the observed fluxes and theoretical intensities of  $\lambda\lambda 7281, 6678, 5875$  and  $4922$  lines relative to  $\lambda 6678$ , which serves as the reference wavelength ( $f(\lambda_{\text{ref}})$ ). These lines, which are unaffected by effects of  $n_e$ , are plotted as points in the plane  $\log(F_\lambda/F_\lambda^{\text{ref}}) - \log(I_\lambda/I_\lambda^{\text{ref}}) = f(\lambda) - f(\lambda_{\text{ref}})$  and a linear regression is applied, the slope of the regression represents the value of  $c(\text{H}\beta)$ . We obtained values of  $c(\text{H}\beta)$  ranging from 0.39 to 0.63 for OAN-SPM observations, which were then used to correct the line intensities for effects of reddening.

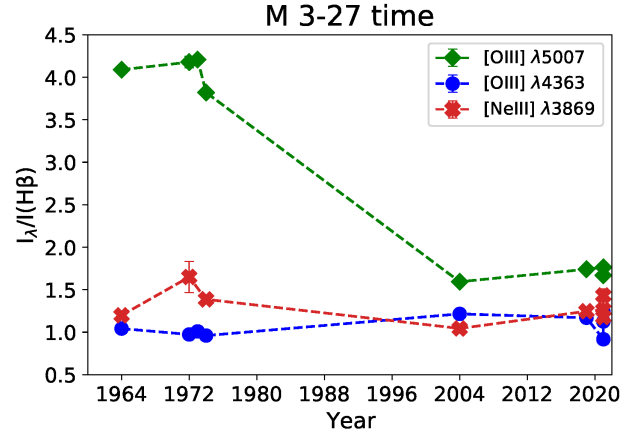


Fig. 2. Line evolution of important lines. (Reproduced from Figure 3 in Ruiz-Escobedo et al. (2024)).

#### 3.3. Temporal evolution of line intensities

In Figure 2, we present the temporal evolution of the intensities relative to  $\text{H}\beta$  of some important lines of M 3-27 in a period between 1968 to 2021. Data from the 1970s are taken from the previous studies in literature, while data from the 2000s are from OAN-SPM observations. The  $[\text{O III}]$  nebular line  $\lambda 5007$  shows a decrement in its intensity, from  $\sim 4 \text{ H}\beta$  in the 1970s to  $\sim 1.7 \text{ H}\beta$  in the 2000s. In contrast,  $[\text{O III}]$  auroral line  $\lambda 4363$  remaining at  $\sim 1 \text{ H}\beta$  during all the period. A similar effect is also observed in the nebular and auroral lines of  $[\text{O II}]$ ,  $[\text{N II}]$  and  $[\text{S II}]$ .  $[\text{Ne III}] \lambda 3869$  does not show either important changes in its intensity, remaining at  $\sim 1.5 \text{ H}\beta$ .

This effect is attributed to an increase in the plasma  $n_e$ , which suppresses the emission of nebular lines because these lines have lower critical densities ( $n_{\text{crit}}$ ) than the auroral lines. An increase in the plasma  $n_e$  throughout the period has been found and will be discussed in the next sections.

We also found a significant increase in  $\text{H}\alpha$  intensity, from  $\sim 4 \text{ H}\beta$  to  $\sim 12 \text{ H}\beta$  in 2021. This confirms that  $\text{H}\alpha$  emission is affected by stellar emission and suggests substantial changes in stellar emission over a short period of time.

#### 3.4. Physical conditions

Physical conditions and abundances were calculated using PyNeb (Luridiana et al. 2015). From OAN-SPM data, we also found the presence of a density gradient in M 3-27, an outer zone where  $n_e \sim 10^3 \text{ cm}^{-3}$  and an inner zone where  $n_e = 10^7 \text{ cm}^{-3}$ ; besides, most of the line diagnostic ratios used for  $T_e$  determination are showed more sensitive to  $n_e$ , therefore, the estimation of a  $T_e$  becomes difficult.

TABLE 1  
REPRESENTATIVE ABUNDANCES OF M3-27

	Echelle 2019	B&Ch 2021
CELs		
O <sup>+</sup> /H <sup>+</sup> ( $\times 10^{-7}$ ) Neb.	0.63 <sup>+0.31</sup> <sub>-0.24</sub>	—
O <sup>+</sup> /H <sup>+</sup> ( $\times 10^{-5}$ ) Aur.	—	1.60 <sup>+0.78</sup> <sub>-0.49</sub>
O <sup>+2</sup> /H <sup>+</sup> ( $\times 10^{-4}$ )	1.68 <sup>+0.31</sup> <sub>-0.32</sub>	1.86 <sup>+0.28</sup> <sub>-0.25</sub>
N <sup>+</sup> /H <sup>+</sup> ( $\times 10^{-6}$ ) Neb.	2.29 $\pm$ 0.31	2.20 <sup>+0.28</sup> <sub>-0.26</sub>
ORLs		
O <sup>+2</sup> /H <sup>+</sup> ( $\times 10^{-4}$ )	5.50 <sup>+0.50</sup> <sub>-0.55</sub>	—
ADF(O <sup>+2</sup> )	3.26 <sup>+0.81</sup> <sub>-0.61</sub>	—
12+log(O/H)	8.22 <sup>+0.07</sup> <sub>-0.09</sub>	8.30 $\pm$ 0.06
log(N/O)	1.55::	-0.87 $\pm$ 0.17

:: Very uncertain value.

By an assuming a  $n_e = 10^7 \text{ cm}^{-3}$ , a  $T_e \sim 17,000 \text{ K}$  is determined from the [O III]  $\lambda\lambda(5007 + 4959)/4363$  line ratio for REOSC-Echelle 2019 and B&Ch 2021 spectra. From REOSC-Echelle 2019 spectrum,  $n_e$  and  $T_e$  from ORLs were determined:  $n_e \sim 10^4 \text{ cm}^{-3}$  from O II  $\lambda\lambda 4661/4649$  and a  $T_e = 8,000 \text{ K}$  from He I  $\lambda\lambda 7281/6678$  (by using Zhang et al. 2005 formula).

### 3.5. Ionic and total abundances

For ionic abundances calculations, two  $n_e$  zones and a single  $T_e$  were assumed for CELs, while a single  $n_e$  and  $T_e$  zone were assumed for ORLs. Since HI lines are affected by stellar emission, we determined ionic abundances relative to He I  $\lambda 5876$  line ( $\frac{X^{+i}}{He^{+}}$ ) using the following formula:

$$\frac{X^{+i}}{He^{+}} = \frac{I_\lambda}{I_{HeI5876}} \times \frac{\epsilon_{HeI5876}}{\epsilon_\lambda} \quad (1)$$

Where  $I_\lambda/I_{HeI5876}$  is the line intensity relative to He I  $\lambda 5876$  and  $\epsilon_{HeI5876}/\epsilon_\lambda$  is the ratio of He I and the line emissivities. These values were escalated to obtain the ionic abundances relative to H<sup>+</sup> by assuming that  $He^{+}/H^{+} = He/H = 0.11$ , the mean He/H for Galactic disc PNe (Kingsburgh & Barlow 1994). Therefore, ionic abundances relative to H<sup>+</sup> were calculated as:  $\frac{X^{+i}}{H^{+}}(He^{+}) = 0.11 \times \frac{X^{+i}}{He^{+}}$ . Abundance discrepancy factor, ADF(O<sup>+2</sup>), was also calculated.

Total abundances were determined from the ionic abundances and corrected using ionization correction factors (ICFs) by Kingsburgh & Barlow (1994). Representative abundances are presented in Table 1.

## 4. DISCUSSION

We found that the inner  $n_e$  has changed from  $10^6 \text{ cm}^{-3}$ , in the 1970s, to  $10^7 \text{ cm}^{-3}$  in the 2000's.

This increment suppresses the emission of nebular lines with low  $n_{crit}$ . Additionally, we identified significant changes in H $\alpha$ /H $\beta$  intensity, which we attribute to important variations in central star emission.

Our results show that almost all O in M3-27 is present in the form of O<sup>+2</sup> and O<sup>+</sup> has a minimal contribution to O/H total abundance. We derived a sub-solar 12+log(O/H) value, ranging from 8.22 to 8.30, which is lower than the 8.60 value reported by Wesson et al. (2005). The O<sup>+</sup> abundance has implications on the determination of total abundances of other elements, such as N, due the construction of their ICFs. As is shown in Table 1, if O<sup>+</sup> abundance is determined using the nebular line [O II]  $\lambda 3727$ , which is suppressed by effects of  $n_e$ , the total N abundance will be overestimated and highly uncertain. However, this is no the case if O<sup>+</sup> abundance is determined from the auroral line [O II]  $\lambda 7325$ , in which case the N abundance behaves accordingly to values of disc PNe. Therefore, we adopted the total abundances derived from B&Ch data. We also derived a ADF(O<sup>+2</sup>) = 3.26 lower than the value of 5.48 reported by Wesson et al. (2005).

M3-27 is a challenging PN for its analysis, due to its high density and its important changes in short periods of time. Further observations and analysis of M3-27 are needed.

**Acknowledgements:** This work has received financial support from grant UNAM-PAPIIT IN111423.

## REFERENCES

- Adams, T. F. 1975, ApJ, 202, 114  
 Ahern, F. J. 1978, ApJ, 223, 901  
 Arrieta, A., & Torres-Peimbert, S. 2003, ApJS, 147, 97  
 Barker, T. 1978, ApJ, 219, 914  
 Kingsburgh, R. L., & Barlow, M. J. 1994, MNRAS, 271, 257  
 Kohoutek, L. 1968, Bulletin of the Astronomical Institutes of Czechoslovakia, 19, 371  
 Luridiana, V., Morisset, C., & Shaw, R. A. 2015, A&A, 573, A42  
 Miranda, L. F., Vazquez, R., Torrelles, J. M., Eiroa, C., & Lopez, J. A. 1997, MNRAS, 288, 777  
 Ruiz-Escobedo, F., Peña, M., & Beltrán-Sánchez, A. V. 2024, MNRAS, 528, 4228  
 Wesson R., Liu, X.-W., & Barlow, M. J., 2005, MNRAS, 362, 424  
 Zamora, S., Díaz, A. I., Terlevich, E., & Fernández, V. 2022, MNRAS, 516, 749  
 Zhang, Y., Liu, X. W., Liu, Y., & Rubin, R. H. 2005, MNRAS, 358, 457

## THE DECAM MAGELLANIC CLOUDS EMISSION-LINE SURVEYS

S. D. Points<sup>1</sup>, K. S. Long<sup>2,3</sup>, W. P. Blair<sup>4</sup>, P. F. Winkler<sup>5</sup>, R. M. Williams<sup>6</sup>, and Y.-H. Chu<sup>7</sup>

### RESUMEN

Hemos utilizado la Cámara de Energía Oscura (DECAM) en el telescopio CTIO Blanco de 4 metros para realizar un nuevo estudio de líneas de emisión de las Nubes Grande y Pequeña de Magallanes (LMC y SMC, respectivamente) con una resolución espacial sin precedentes, utilizando filtros  $H\alpha$  de banda estrecha y [S II], además de una banda de continuo para sustracción. Estos datos son comparables en profundidad a los estudios de líneas de emisión existentes de las Nubes de Magallanes (por ejemplo, MCELS), pero con una mayor resolución angular. Hemos creado una pipeline personalizada basada en Python para reducir estos datos y presentar ejemplos de nuestros primeros resultados.

### ABSTRACT

We have used the Dark Energy Camera (DECAM) on the CTIO Blanco 4-m telescope to perform a new emission-line survey of the Large and Small Magellanic Clouds (LMC and SMC, respectively) with unprecedented spatial resolution, using narrow-band  $H\alpha$  and [S II] filters in addition to a continuum band for use in subtraction. These data are comparable in depth to extant emission-line surveys of the Magellanic Clouds (e.g., MCELS), but with higher angular resolution. We have created a custom Python-based pipeline to reduce these data and present examples of our first results.

*Key Words:* H II regions — ISM: supernova remnants — Magellanic Clouds

### 1. INTRODUCTION

The Large and Small Magellanic Clouds (LMC & SMC) are the two most significant satellite galaxies of the Milky Way, at distances of 50 and 60 kpc (Pietrzyński et al. 2019; Graczyk et al. 2020), and experience low galactic foreground extinction. They are the best laboratories to investigate a wide variety of astrophysical phenomena, including the life cycle of stars and the interplay between stars and the interstellar medium (ISM).

High-quality optical emission line imagery is key for such investigations, showing both the morphology and ionization structure of nebular emission on all scales and permitting meaningful comparisons with multi-wavelength data sets. For the Magellanic

Clouds (MCs), the most widely used optical survey has been the Magellanic Cloud Emission-Line Survey (MCELS, Smith & MCELS Team 1999), which provided imagery with  $\sim 5''$  resolution. Recently, higher resolution emission-line data for much of the MCs has been obtained with the Dark Energy Camera (DECAM, Honscheid & DePoy 2008; Flaughner et al. 2015) on the CTIO Blanco 4 m telescope.

In §2, we describe the DECAM observations of the MCs. We discuss the data reduction in §3 and present our results in §4. We summarize our work in §5.

### 2. OBSERVATIONS

The DECAM images were obtained using the N662 ( $H\alpha$  + [N II] $\lambda\lambda 6548, 6583$ ) and N673 ([S II] $\lambda\lambda 6716, 6731$ ) filters in addition to the DES  $r'$  for continuum-subtraction. The narrow band filters are hereafter referred to as the  $H\alpha$  and [S II] filters. DECAM is a wide-field CCD imager with 62 science detectors that images 3 square degrees ( $2.2^\circ$  wide) at  $0.263''$  resolution (although the images are seeing limited).

The inner  $54 \text{ deg}^2$  of the LMC was covered by 20 DECAM fields and the inner  $18.2 \text{ deg}^2$  of the SMC was covered by 5 DECAM fields. Each field was observed with short and long exposures, with dithers between each exposure to fill in the detector gaps.

<sup>1</sup>NSF's NOIRLab, CTIO, Casilla 603, La Serena, Chile.

<sup>2</sup>Space Telescope Science Institute, 3700 San Martin Dr, Baltimore MD, 21218, USA.

<sup>3</sup>Eureka Scientific, Inc., 2452 Delmer Street, Suite 100, Oakland, CA 94602-3017, USA.

<sup>4</sup>The William H. Miller III Department of Physics and Astronomy, Johns Hopkins University, 3400 N. Charles Street, Baltimore, MD, 21218, USA.

<sup>5</sup>Department of Physics, Middlebury College, Middlebury, VT, 05753, USA.

<sup>6</sup>Department of Earth and Space Sciences, Columbus State University, 4225 University Avenue, Columbus, Georgia 31907, USA.

<sup>7</sup>Academia Sinica, 11F of AS/NTU Astronomy-Mathematics Building, No.1, Sec. 4, Roosevelt Rd, Taipei 10617, Taiwan, R.O.C.

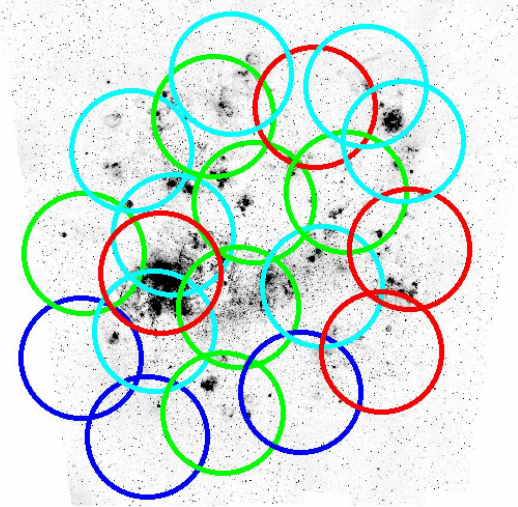


Fig. 1. MCELS  $H\alpha$  mosaic of the LMC with  $2^\circ$  diameter circles representing the approximate DECcam footprint overlaid for all narrow band data. The colors of the circles represent the completeness of the long observations compared to the desired uniform depth:  $\geq 2/3$  complete in  $H\alpha$  and [S II] (green);  $\geq 2/3$  complete in  $H\alpha$  and  $\leq 2/3$  complete in [S II] (blue);  $\leq 2/3$  complete in  $H\alpha$  and  $\geq 2/3$  complete in [S II] (cyan); and  $\leq 2/3$  complete in both  $H\alpha$  and [S II] (red).

For the long exposures, a total of  $6 \times 800s$  were obtained in  $H\alpha$  and  $12 \times 800s$  in [S II]<sup>8</sup>. We present the MCELS  $H\alpha$  images of the LMC and SMC with the DECcam fields marked in Fig. 1 and 2, respectively.

### 3. DATA REDUCTION

The data contained in the survey were obtained over a number of nights and under varying conditions. Our goal in reducing these data was to produce mosaicked versions of these images and to accurately represent diffuse emission (on large and small scales) at brightness levels that are significantly lower than those observed from the night sky. This is further complicated because the broad band  $r'$  filter contains emission from both  $H\alpha$  and [S II], making continuum-subtraction difficult.

To reduce these data, we begin with data processed by the DECcam Community Pipeline (DCP, Valdes et al. 2014). After a data quality assessment to remove observations with seeing values  $\geq 1.5''$ , we used custom Python-based programs<sup>9</sup> that make

<sup>8</sup>As shown in Fig. 1 and 2, neither the LMC nor the SMC were completely covered to the desired extent and depth by our observations. Some fields were either missed, under-observed, or affected by poor seeing, creating significant ‘holes’ in the survey data

<sup>9</sup>The current version of the reduction pipeline, referred to as KRED, can be found on github at <https://github.com/>

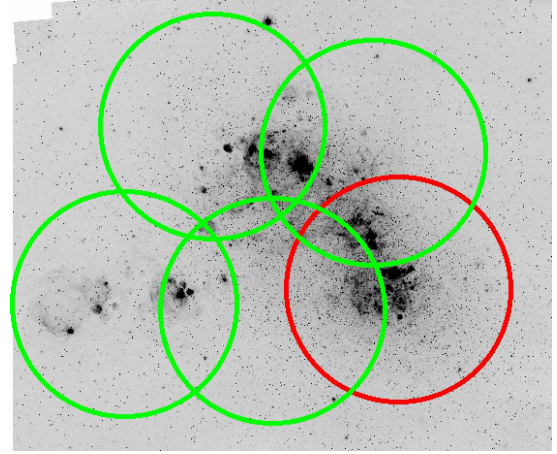


Fig. 2. MCELS  $H\alpha$  mosaic of the SMC with the same labeling scheme as Fig 1.

extensive use of SWarp (Bertin et al. 2002) to produce our final continuum-subtracted images. The primary steps of the KRED package are described below:

- Re-scale all data to a common magnitude scale to facilitate image subtraction and remove a single background value from all CCDs.
- Create a  $4 \times 4$  grid of overlapping tiles for each field as a convenience to allow for producing uniform data products.
- Sort the observations by exposure times and filters and measure the difference in flux levels of overlapping detectors. These differences are used place exposures of a given exposure time and filter a common background level.
- Use SWarp to combine images in each filter based on exposure time to place the stacked images on a common world coordinate system.
- Create a “line-free” continuum image using data from all observations and subtract these continuum images from the emission-line images.

## 4. RESULTS

Although we consider the currently available data products to be preliminary, the superior resolution and overall depth and quality of the DECcam images is apparent. Below we show examples of these data toward different types of interstellar structures and compare them to the MCELS data.

### 4.1. Small H II Regions

Isolated massive stars produce small H II regions through their ionizing radiation and wind-blown

[kslong/kred](https://github.com/kslong/kred). We would be pleased to have others make use of it, and/or to help improve it further.

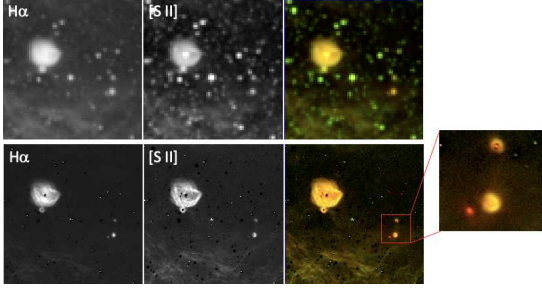


Fig. 3. A comparison of MCELS and DECam data for a small region from a field that contains several small to very small star forming regions. The top row shows MCELS H $\alpha$  and [S II] images in black and white with a color combination at right (red: H $\alpha$ ; green: [S II]). Yellow indicates that both ions are strong. The bottom row shows the same sequence, but for our DECam data. For scale, the box at right is 30". These small emission nebulae are completely unresolved in the MCELS data.

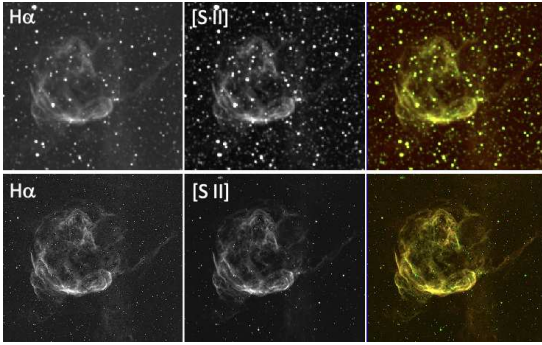


Fig. 4. A comparison of MCELS and DECam data for the faint SNR 0527–6549. Presentation is the same as in Fig. 3. This is a low surface brightness SNR. For scale, the SNR is about 250" in diameter.

bubbles through the action of their stellar winds. As shown in Fig. 3, these small nebulae are unresolved in MCELS, but are readily apparent in our DECam data.

#### 4.2. Supernova Remnants (SNRs)

One of the main science goals of the DECam survey was to obtain higher resolution images of the known SNR population and to search for fainter, larger, and presumably older SNRs that are beginning to merge back into the ISM (cf, Yew et al. 2021). Fig. 4 shows a comparison between the MCELS and DECam data for a faint, isolated SNR in the LMC. Williams et al. (2024, this volume) discuss the MC SNR population as seen by DECam in more detail.

#### 4.3. Bubbles and Superbubbles

Fig. 5 shows the region surrounding N70 (Henize 1956), an isolated nebular superbubble in the eastern

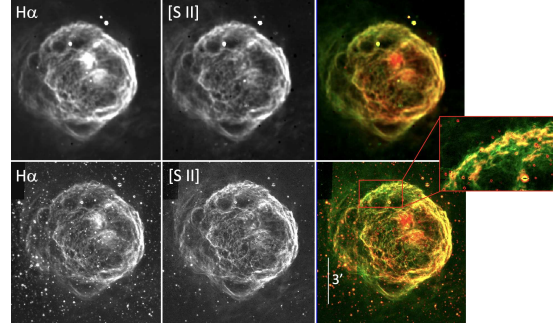


Fig. 5. A comparison of MCELS and DECam data for the N70, a superbubble  $\sim 7.8'$  in diameter and located in an isolated region in the eastern LMC. The presentation is the same as Fig 3 and the scale is shown in the lower right color panel. The inset at right shows detail of the northern rim.

LMC, also known as DEM L301 (Davies et al. 1976). N70 has a diameter of 7.8' ( $\sim 105$  pc) and surrounds the stellar association LH 114 (Lucke & Hodge 1970).

### 5. SUMMARY

We have conducted a recent H $\alpha$  and [S II] emission-line survey of the MCs using DECam. The data have been reduced using our pipeline to produce a uniform set of flux-calibrated, continuum-subtracted images that show a remarkable improvement in angular resolution when compared to the MCELS survey. These data will enable a broad-range of ISM science and provide a legacy resource for many future research programs.

### REFERENCES

Bertin, E., Mellier, Y., Radovich, M., et al. 2002, *Astronomical Data Analysis Software and Systems XI*, 281, 228

Davies, R. D., Elliott, K. H., & Meaburn, J. 1976, *MNRAS*, 81, 89

Flaugher, B., Diehl, H. T., Honscheid, K., et al. 2015, *AJ*, 150, 150. doi:10.1088/0004-6256/150/5/150

Graczyk, D., Pietrzyński, G., Thompson, I. B., et al. 2020, *ApJ*, 904, 13. doi:10.3847/1538-4357/abbb2b

Henize, K. G. 1956, *ApJS*, 2, 315. doi:10.1086/190025

Honscheid, K. & DePoy, D. L. 2008, arXiv:0810.3600. doi:10.48550/arXiv.0810.3600

Lucke, P. B. & Hodge, P. W. 1970, *AJ*, 75, 171. doi:10.1086/110959

Pietrzyński, G., Graczyk, D., Gallette, A., et al. 2019, *Nature*, 567, 200. doi:10.1038/s41586-019-0999-4

Smith, R. C. & MCELS Team 1999, *New Views of the Magellanic Clouds*, 190, 28

Valdes, F., Gruendl, R., & DES Project 2014, *Astronomical Data Analysis Software and Systems XXIII*, 485, 379

Yew, M., Filipović, M. D., Stupar, M., et al. 2021, *MNRAS*, 500, 2336. doi:10.1093/mnras/staa3382

## SUPERNOVA REMNANT SIGNATURES IN EMISSION-LINE SURVEYS OF THE MAGELLANIC CLOUDS WITH NOIRLAB'S DECam

R. N. M. Williams<sup>1</sup>, S. D. Points<sup>2</sup>, K. S. Long<sup>3,4</sup>, W. P. Blair<sup>5</sup>, and P. F. Winkler<sup>6</sup>

### RESUMEN

Describimos el uso de datos obtenidos con el sondeo DECam de  $H\alpha$  y  $[S II]$  de la Gran Nube de Magallanes (LMC), para estudiar su población de remanentes de supernovas (SNR). Revisamos las firmas observacionales de SNR, incluyendo los cocientes elevados de  $[S II]/H\alpha$ , que se utilizan para identificar y caracterizar estos objetos. Esto incluye recuperar SNR conocidos en los datos, corroborar candidatos a SNR sugeridos por otros instrumentos y buscar candidatos a SNR no identificados previamente. Destacamos ejemplos específicos de este sondeo, incluido el análisis de la estructura óptica de SNR confirmados y candidatos.

### ABSTRACT

We describe our use of newly obtained DECam  $H\alpha$  and  $[S II]$  surveys of the Large Magellanic Cloud (LMC), to study its supernova remnant (SNR) population. We review the SNR signatures, including elevated  $[S II]/H\alpha$  ratios, used to identify and characterize these objects. This includes recovering known SNRs in the data, verifying SNR candidates suggested by other instruments, and searching for previously unidentified SNR candidates. We highlight specific examples from this survey, including examination of the detailed optical structure of confirmed and candidate SNRs.

*Key Words:* ISM: supernova remnants

### 1. INTRODUCTION

The Large Magellanic Cloud (LMC) sample of supernova remnants (SNRs) has many advantageous qualities for the study of energy input to the interstellar medium (ISM) of a galaxy. As noted by Y.-H. Chu (this volume) the LMC is at high Galactic latitude, less affected by obscuration, and is seen nearly face-on. There have been extensive multi-wavelength surveys and object studies in the LMC, leading to a well-studied group of confirmed SNRs and a significant number of SNR candidates. Also, these SNRs are at a common, known distance of 50 kpc, so that  $1'' \approx 0.24$  pc. Thus, observations can be directly converted to physical properties in the SNRs.

Dense clumps cooling behind a SNR shock front produce a range of optical emission lines. Notably, a  $S II / H\alpha$  ratio  $\geq 0.4$  (Long 2017) is only found in a

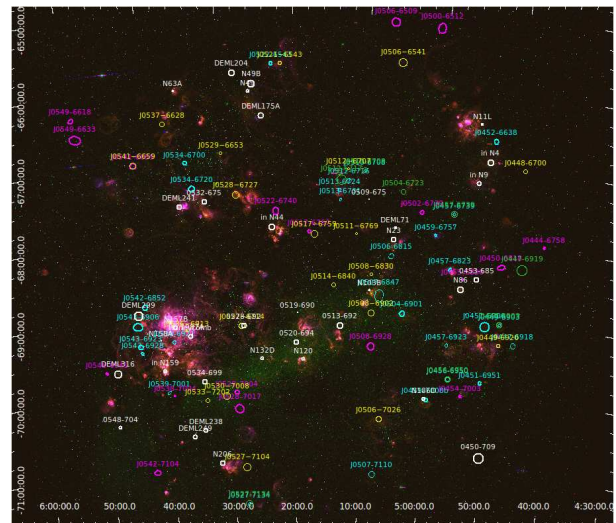


Fig. 1. MCELS image of the LMC in  $H\alpha$  (red),  $S II$  (green), and  $O III$  (blue). Superposed are identified SNRs and SNR candidates.

narrow temperature and density range often indicative of shocked gas. This, thermal X-ray, and non-thermal radio emission are the most common criteria for classifying an object as an SNR, *e.g.* Long (2017). Much of the optical SNR identification in the LMC was based on the Magellanic Clouds Emission-Line

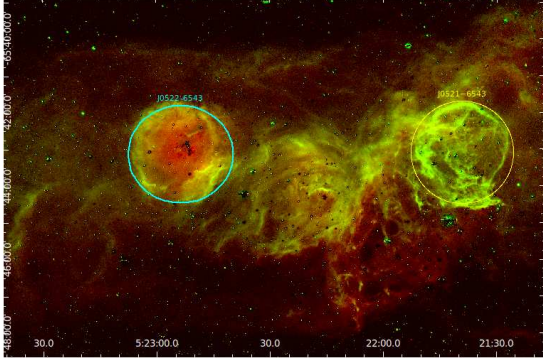


Fig. 2. DECcam data for SNR J0521–6543 and surrounding regions. H $\alpha$  emission is shown in red and S II in green.

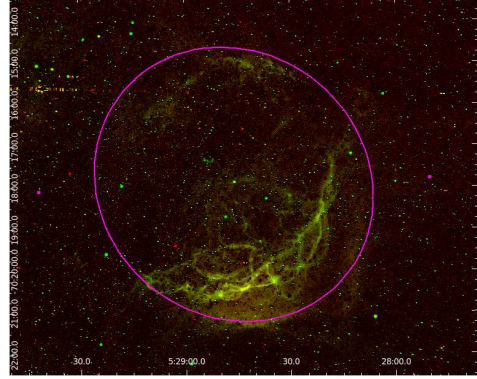


Fig. 3. DECcam data with H $\alpha$  emission shown in red and S II in green. SNR candidate Yew 12 (SNR J0528–7017) is marked in magenta.

Survey (MCELS, Smith et al. 1999); *e.g.* Yew et al. (2021) identified three SNRs and sixteen candidates in MCELS and supplementary data.

2. OBSERVATIONS

An opportunity to significantly improve on the MCELS 5'' resolution was presented by the Dark Energy Camera (DECam) on the Blanco 4-meter telescope at CTIO. Using the N662 (H $\alpha$ ) and N673 (S II) filters, and red-band for continuum subtraction, observers were able to obtain seeing-limited images (S. D. Points, this volume). This provided high-resolution, continuum- and star-subtracted H $\alpha$  and S II images covering the LMC. One objective of this dataset was to provide optical images of SNRs that had not previously been examined at high optical resolution, which notably includes most of the larger, fainter SNRs that roughly correlate with late-stage SNR evolution prior to merging with the ISM.

Our interests are primarily associated with studies of SNRs, so we compiled lists of LMC SNRs and SNR candidates from the literature, shown in Fig. 1. These include X-ray identified SNRs from Williams et al. (1999, white), Maggi et al. (2016, yellow), and Kavanagh et al. (2022, green; follow-ups on ROSAT sources matching radio candidates); optical candidates from Yew et al. (2021, magenta); and radio candidates suggested by Bozzetto et al. (2017, 2023, cyan). We displayed the H $\alpha$  and S II images at matching scales, on which we superposed SNRs and candidates with their coordinates from the literature. We then examined these regions for optical signatures of shocked gas, such as S II /H $\alpha$  ratio enhancements typical of shocked gas and narrow filamentary structures within the region.

A challenge to optical SNR studies is to distinguish signatures of SNRs from those of other sources. H II regions with low surface brightness can show

strong S II lines. However, the interiors of such regions often show bright H $\alpha$  from photoionized gas; and their morphology tends to be less shell-like or filamentary. Similarly, superbubbles (SBs) can show enhanced S II /H $\alpha$  ratios. While SBs are statistically larger than SNRs, there is no clear size boundary between the two, as SNRs can grow large in low-density surroundings. Indeed, several SBs are thought to be enhanced by shocks from internal SNRs, *e.g.* Chu & Mac Low (1990). To an extent, one can use the local massive star population to identify SBs, *e.g.* Chu & Kennicutt (1988), and eliminate some SBs from our sample. But areas with massive star populations are also likely sites for SNRs!

An example near SNR J0521–6543 can be seen in Fig. 2. The yellow outline indicates thermal X-ray emission (Maggi et al. 2016), matching the bright ring of high S II /H $\alpha$  in the DECcam image. The narrow, curved filaments in both emission lines are similar to those frequently seen in SNRs. In contrast, the cyan outline was identified by Bozzetto et al. (2023) as a confirmed SNR from its radio emission. The optical extent matches the listed dimensions at radio wavelengths. However, the object has bright central H $\alpha$  and the S II emission surrounding it is graduated and diffuse, lacking filamentary structure. In the images before star subtraction, the region also shows a central star cluster; and in the MCELS data, the region has bright central O III as well. These characteristics are more typical of the outer rims of photoionized regions, *e.g.* Pelligrini et al. (2012).

The resolution of the DECcam data allows us to better discern the details of emission-line morphology. Fig. 3 shows candidate SNR J0528–7017, first identified in MCELS data. In the DECcam data,

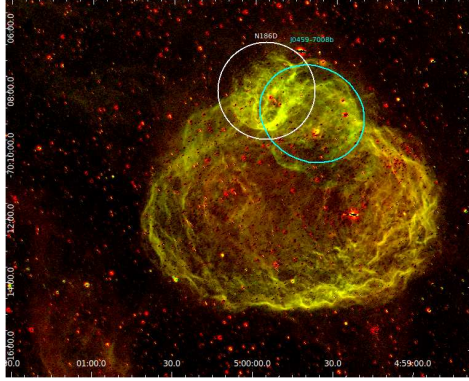


Fig. 4. DECAM data with  $H\alpha$  emission shown in red and S II in green, showing the complex region LHA 120-N 186.

its fine filamentary structure can be seen. Fig. 4 shows the complex N186 region. SNR J0459–7008 (N186D) is a known SNR in this region, but in the DECAM emission-line images we can see more S II filamentary structures nearby, including another shell-like structure with a high S II /  $H\alpha$  ratio. The second S II shell corresponds to radio SNR candidate J0459-7008b of Bozzetto et al. (2023).

We also searched for new promising SNR candidates in the DECAM data. Fig. 5 shows one such object at the location of DEM L 81, near stellar cluster KHMx 565. It is noticeably bright in S II compared to  $H\alpha$ , and has a roughly circular structure (radius  $2.5' \approx 36$  pc) with multiple narrow filaments.

### 3. SUMMARY AND FUTURE WORK

The new DECAM optical emission-line survey of the LMC (and its counterpart for the Small Magellanic Cloud) presents a fantastic opportunity to develop a much more complete inventory of SNRs and SNR candidates. We have already found optical counterparts for a number of SNR candidates suggested from X-ray or radio data. We expect more detailed analysis will confirm the identification of some objects, adding to the catalog of confirmed SNRs in the LMC. In other cases, optical structures may suggest alternate explanations for objects that have been suggested as SNR candidates. We have also been able to identify several new SNR candidates from their high S II /  $H\alpha$  ratios and filamentary morphologies. We intend to follow up with archival data and new observations at other wavelengths to confirm their SNR nature. For the resulting confirmed SNRs, we can then compare their optical structure to that in X-ray and radio. While X-ray studies allow physical properties of the diffuse hot gas to be inferred, the optical emission-line fluxes will allow us

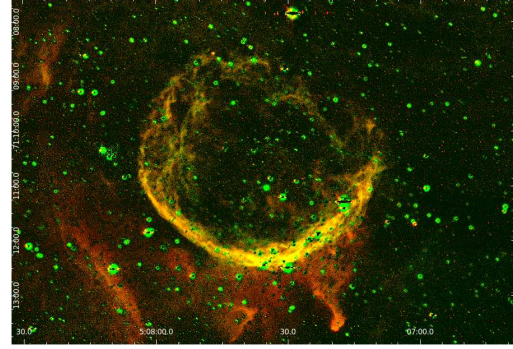


Fig. 5. DECAM data showing an area near DEM L 81.  $H\alpha$  emission is shown in red and S II in green.

to do the same for the denser material in clumps and filaments. Together, these should provide powerful tools to determine physical properties in these objects. It will also identify the most promising objects for follow-up studies *e.g.*, of velocity distributions.

We expect to use the DECAM MC survey to search for additional SNR candidates, particular for larger, more evolved SNRs. This is a significant step toward extending our census of SNRs in a galaxy to include later stages of SNR evolution and their merging with the ISM - an important input parameter to the stellar feedback history of a galaxy. More generally, we will use the emission line ratios to study other types of shocks in the MCs, extending our studies to larger-scale interactions that will provide insight to the shaping of the ISM in those galaxies.

### REFERENCES

- Bozzetto, L. M., Filipović, M. D., Vukotić, B. et al. 2017, *ApJS*, 230, 2
- Bozzetto, L. M., Filipović, M. D., Sano, H., et al. 2023, *MNRAS*, 518, 2574
- Chu, Y.-H. & Kennicutt, R. C. 1988, *AJ*, 96, 1874
- Chu, Y.-H. & Mac Low, M.-M. 1990, *ApJ*, 365, 510
- Kavanagh, P. J., Sasaki, M., Filipović, M. D., et al. 2022, *MNRAS*, 515, 4099
- Long, K. S. 2017, in *Handbook of Supernovae*, ed. A. Alsabti, & P. Murdin, Springer, Cham
- Maggi, P., Haberl, F., Kavanagh, P. J., et al. 2016, *A&A*, 585, 162
- Pelligrini, E. W., Oey, M. S., Winkler, P. F., et al. 2012, *ApJ*, 755, 40
- Smith, R. C., & MCELS Team, 1999, in *IAU Symposium Vol. 190, New Views of the Magellanic Clouds*, ed. Y.-H. Chu, N. Suntzeff, J. Hesser, & D. Bohlender, 28
- Williams, R. N. M., Chu, Y.-H., Dickel, J. R. et al. 1999, *ApJS*, 123, 467
- Yew, M., Filipović, M. D., Stupar, M., et al. 2021, *MNRAS*, 500, 2336

## DETECTING $\gamma$ -RAYS FROM THE ANCORA SUPERNOVA REMNANT

Christopher Burger-Scheidlin<sup>1,2</sup>, Robert Brose<sup>1,3</sup>, Jonathan Mackey<sup>1,2</sup>, Miroslav D. Filipović<sup>4</sup>,  
Pranjupriya Goswami<sup>5,6</sup>, Enrique Mestre Guillen<sup>7</sup>, Emma de Oña Wilhelmi<sup>8</sup>, and Iurii Sushch<sup>6,9,10</sup>

### RESUMEN

Recientemente, se descubrió un nuevo remanente de supernova (SNR), G288.8–6.3, en longitudes de onda de radio como una cáscara débil con el Australian Square Kilometer Array Pathfinder (ASKAP) en el estudio del Mapa Evolutivo del Universo (EMU). Esto provocó una investigación detallada de los rayos  $\gamma$  de la región que nos gustaría describir aquí. Para esta tarea, se analizaron quince años de datos del *Fermi*–Large Area Telescope (LAT) entre 400 MeV y 1 TeV. Detectamos emisiones de rayos  $\gamma$  espacialmente extendidas que se superponen con el SNR de radio con una significancia de detección de hasta  $8.8\sigma$ . El modelo preferido era un modelo espacial de disco combinado con un modelo espectral de ley potencial, produciendo un flujo de energía de  $(4.80 \pm 0.91) \times 10^{-6} \text{ MeV cm}^{-2} \text{ s}^{-1}$ , con el espectro que se extiende hasta 5 GeV. Dadas las estimaciones de densidad, edad y distancia del gas, es más probable que la emisión sea de origen leptónico.

### ABSTRACT

Recently, a new supernova remnant (SNR), G288.8–6.3, was discovered at radio wavelengths as a faint shell with the Australian Square Kilometre Array Pathfinder (ASKAP) in the Evolutionary Map of the Universe (EMU) survey. This prompted a detailed investigation of  $\gamma$ -rays from the region that we would like to describe here. For this task, fifteen years of *Fermi*–Large Area Telescope (LAT) data were analysed between 400 MeV and 1 TeV. We detected spatially extended  $\gamma$ -ray emission overlapping with the radio SNR with a detection significance of up to  $8.8\sigma$ . The favoured model was a disk spatial model combined with a power-law spectral model, yielding an energy flux of  $(4.80 \pm 0.91) \times 10^{-6} \text{ MeV cm}^{-2} \text{ s}^{-1}$ , with the spectrum extending up to 5 GeV. Given the estimates for the gas density, age and distance, the emission is more likely to be of leptonic origin.

*Key Words:* cosmic rays — ISM: gamma-rays — ISM: radio continuum — ISM: supernova remnants — ISM: individual objects: G288.8–6.3 (SNR)

### 1. INTRODUCTION

Since the discovery of cosmic rays (CRs) by Victor Hess there has been speculation on their origin. The current consensus is that cosmic protons

with energies up to  $3 \times 10^{15} \text{ eV}$  originate from within our Galaxy (Aloisio et al. 2012). Supernova Remnants (SNRs) were first suggested as CR sources by Baade and Zwicky. Currently, around three hundred SNRs have been detected (Green 2019) at radio wavelengths, with around 10% also being detected in  $\gamma$ -rays (Acero et al. 2016).

In the last few years, supernova remnants at high Galactic latitudes have received some attention, with the detection of a few previously unknown sources at  $\gamma$ -ray energies (e.g. Ackermann et al. 2018, Araya 2013).

We detected extended  $\gamma$ -ray emission from the G288.8–6.3 region, spatially coincident with a low-surface-brightness shell-like SNR first discovered by Filipovic et al. (2023) using *Australian Square Kilometre Array Pathfinder (ASKAP)* data. The authors reported an estimated distance of  $\sim 1.3 \text{ kpc}$ , with a distance of about 140 pc above the Galactic plane, and, based on the surface brightness, an age of  $> 13 \text{ kyr}$ .

<sup>1</sup>Dublin Institute for Advanced Studies, Astronomy & Astrophysics Section, DIAS Dunsink Observatory, Dublin, D15 XR2R, Ireland (cburger@cp.dias.ie).

<sup>2</sup>School of Physics, University College Dublin, Belfield, Dublin, D04 V1W8, Ireland.

<sup>3</sup>School of Physical Sciences and Centre for Astrophysics & Relativity, Dublin City University, D09 W6Y4 Glasnevin, Ireland.

<sup>4</sup>Western Sydney University, Locked Bag 1797, Penrith South DC, NSW 2751, Australia.

<sup>5</sup>Université Paris Cité, CNRS, Astroparticule et Cosmologie, F-75013 Paris, France.

<sup>6</sup>Centre for Space Research, North-West University, 2520 Potchefstroom, South Africa.

<sup>7</sup>Institute of Space Sciences (ICE, CSIC), Campus UAB, Carrer de Can Magrans s/n, 08193 Barcelona, Spain.

<sup>8</sup>Deutsches Elektronen-Synchrotron DESY, Plataneallee 6, 15738 Zeuthen, Germany.

<sup>9</sup>Astronomical Observatory of Ivan Franko National University of Lviv, Kyryla i Methodia 8, 79005 Lviv, Ukraine.

<sup>10</sup>Gran Sasso Science Institute, Via F. Crispi 7, 67100 L'Aquila, Italy.

TABLE 1  
BEST-FIT PARAMETERS OF THE RADIAL  
DISK MODEL WITH THE POWER-LAW  
SPECTRAL MODEL FOR ANCORA SNR

Parameter	Unit	Value
Position		
R.A. / Dec	deg / deg	157.488 / $-65.214$
GLON / GLAT	deg / deg	288.8 / $-6.3$
Spatial model		<i>RadialDisk</i>
Spectral model		<i>PowerLaw</i>
TS	—	77.14
N° of predicted photons	—	1331
Photon flux	ph cm <sup>-2</sup> s <sup>-1</sup>	$(3.14 \pm 0.41) \times 10^{-9}$
Energy flux	MeV cm <sup>-2</sup> s <sup>-1</sup>	$(4.80 \pm 0.91) \times 10^{-6}$
> 1 GeV (to 316 GeV)	MeV cm <sup>-2</sup> s <sup>-1</sup>	$(3.29 \pm 0.78) \times 10^{-6}$
Spectral parameters		
N <sub>0</sub>	MeV <sup>-1</sup> cm <sup>-2</sup> s <sup>-1</sup>	$(1.23 \pm 0.16) \times 10^{-12}$
Γ	—	2.32 ± 0.11
E <sub>0</sub>	MeV	1000*
Spatial parameters		
Extension	deg	0.92 ± 0.06
TS <sub>ext</sub> <sup>†</sup>	—	52.56

\*Parameter fixed

<sup>†</sup>Test statistic for the extension hypothesis against the null hypothesis of a point-like source.

## 2. DATA ANALYSIS

The analysis was conducted using fifteen years of *Fermi*–Large Area Telescope (LAT) Pass 8 data (Aug 2008 – July 2023), and the P8R3\_SOURCE class (Atwood et al. 2013) was applied. Data were selected within a radius of 12° in the region of interest (ROI) around the centre of the detected radio SNR at Galactic position GLON/GLAT = 288.8°/−6.3° in an energy range of 400 MeV – 1 TeV. We also made cuts on the PSF (point-spread function) class (evtype = 56), discarding low-quality (PSF0) class events.

The analysis was executed using the Python package *Fermipy* (v1.1.6, Wood et al. 2017) and *Fermitools* software (v2.2.0<sup>11</sup>) by employing the standard procedure of the binned maximum-likelihood analysis technique. The fourth Fermi catalogue (Abdollahi et al. 2020), 4FGL-DR3 (Abdollahi et al. 2022), with source modelling up to 3° outside the ROI, was used.

The models used to fit the source extension were a radial disk model, and a radial, symmetric two-dimensional (2D) Gaussian, and smoothed radio template, as well as using a power-law and a log-parabola spectral model.

## 3. RESULTS

Different spatial and spectral models were tested for in the course of the study, and their their rela-

tive log-likelihood values were compared, as well as the value of the Akaike information criterion (AIC; Akaike 1974)<sup>12</sup> We modelled the region with and without taking into account the 4FGL-DR3 catalogue source 4FGL J1028.7-6431c (abbreviated as J1028), which was positioned about 0.7*circ* from the centre of the remnant, which has not been confirmed to be associated with any known source.

The best-fit models, taking into account the AIC criterion, were a radial disk spatial model combined with a power-law spectral model, both with and without modelling J1028. In this work we show the results where the excess for J1028 is not separately modelled. Some excess remains around the position of J1028 – it is thus not entirely clear if this excess is associated with Ancora SNR or part of an unrelated source overlapping in this region. The best-fit parameters can be found in Table 1. The significance map of the region is shown in Fig 1 (left) in a field-of-view of approximately 4.0° × 4.5°, and the extracted spectral energy distribution (SED) from the source (marked with a white circle) is shown in Fig. 1 (right). More details of the modelling and results can be found in C.B.S. et al. (2024).

Overall, the  $\gamma$ -ray emission seems to be more extended than the radio signal, and there is no clear shell-like morphology seen in  $\gamma$ -rays. The SED extends up to 5 GeV and the fit power-law spectrum shows an energy flux of  $(4.8 \pm 0.91) \times 10^{-6}$  MeV cm<sup>-1</sup> s<sup>-1</sup> with a spectral index of  $\Gamma = 2.32 \pm 0.11$ , with a total source significance of  $\sim 8.8\sigma$ .

Multiwavelength modelling using both radio and  $\gamma$ -ray flux points to investigate a leptonic inverse Compton scenario and a hadronic pion decay scenario was performed using *Naima* modelling (Zabalza 2015) assuming a power-law distribution of electrons with an exponential cutoff, and a power-law distribution of protons in the hadronic case. The results show that the energy in electrons are about 0.25% (assuming an explosion energy of 10<sup>51</sup> erg) – typical values for such a source – and a spectral index of  $s = 2$ , matching canonical expectations. Due to the low gas density expected from observations by Filipovic et al. (2023), around 30% of the explosion energy would have to go into hadrons to explain the emission, making this scenario less likely than the leptonic one.

<sup>11</sup><https://github.com/fermi-lat/Fermitools-conda>.

<sup>12</sup>AIC is a qualitative measure indicating which of a number of different models is preferred over the others, taking into account the difference in free parameters.

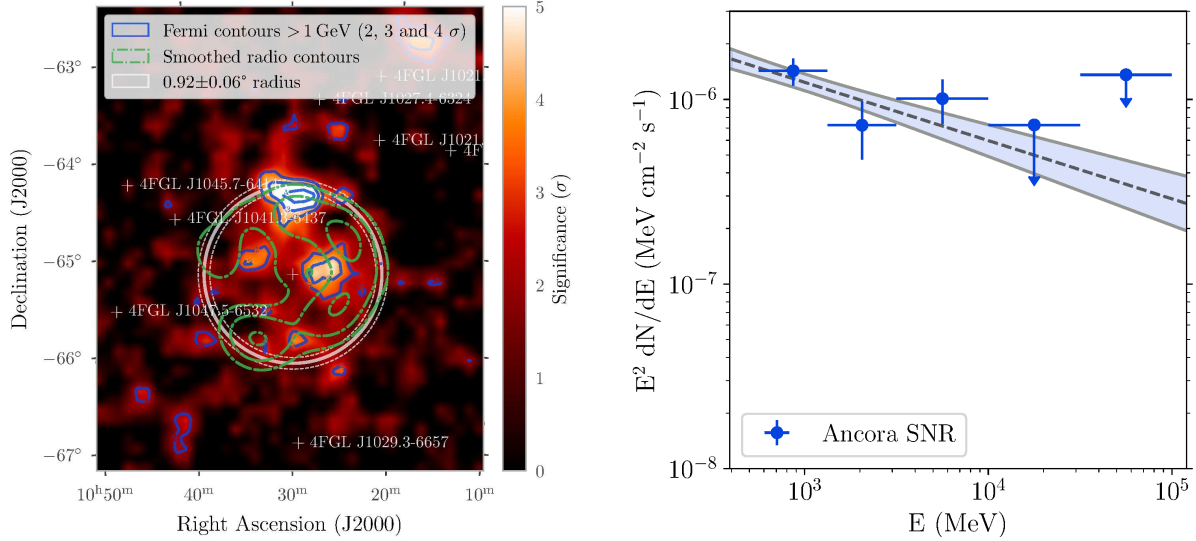


Fig. 1. Significance map of the G288.8–6.3 region, as seen with *Fermi*-LAT, after fitting with a radial disk and power-law model in the energy range of 400 MeV – 1 TeV. The white circle with radius  $0.92\circ$  shows the radius of the disk obtained from the extension fitting. The violet contours highlight areas with signal above 1 GeV. The green contours overlaid show the smoothed radio contours from Filipovic et al. (2023).

#### 4. DISCUSSION AND CONCLUSION

When comparing with other SNRs located at high latitudes detected at very high energies, it seems that Ancora SNR lies between values found for other sources, both in terms of flux, as well as considering the spectral index. The location of SNRs far from the Galactic plane and thus the potentially much lower gas densities increases the likelihood of the emission being of leptonic origin.

The authors also looked at possible interaction with molecular clouds along the line of sight by inspecting thermal dust emission maps from the *Planck* mission (Planck Collaboration 2016). While a gradient towards the Galactic plane can be observed and there is significant dust emission in the G288.8–6.3 region, the lack of correlation disfavours a sizeable hadronic contribution. Based on the gas map, leptonic emission would seem to be the more likely scenario.

With Ancora, we have detected the only seventh off-plane supernova remnant emitting at  $\gamma$ -ray wavelengths, with its spectrum extending up to 5 GeV, and morphological hotspots coinciding well with the radio shell. Further observations with upcoming Imaging Atmospheric Cherenkov Telescopes (IACTs), such as the Cherenkov Telescope Array (CTA) could give more insight into the existence of a cut-off in the spectrum and possibly deeper morphological studies at very high energies.

**Acknowledgements:** C.B.S. acknowledges support from a Royal Society-Science Foundation Ire-

land Research Fellows Enhancement Award 2021 (22/RS-EA/3810). This work was supported by an Irish Research Council (IRC) Starting Laureate Award (IRCLA/2017/83). R.B. acknowledges funding from the Irish Research Council under the Government of Ireland Postdoctoral Fellowship program. J.M. acknowledges support from a Royal Society – Science Foundation Ireland University Research Fellowship (20/RS-URF-R/3712) M.D.F., G.R. and S.L. acknowledge Australian Research Council funding through grant DP200100784. I.S. acknowledges support by the National Research Foundation of South Africa (Grant Number 132276).

#### REFERENCES

Abdollahi, S. et al. 2020, *ApJS*, 247, 33  
 Abdollahi, S. et al. 2022, *ApJS*, 260, 53  
 Acero, F. et al. 2016, *ApJS*, 224, 8  
 Ackermann, M. et al. 2018, *ApJS*, 237, 32  
 Akaike, H. 1974, *IEEE Transactions on Automatic Control*, 19, 716  
 Aloisio, R. et al. 2012, *Astrop. Phys.*, 39-40, 129  
 Araya, M. 2013, *MNRAS*, 434, 2202  
 Atwood, W. et al. 2013, *Fermi Symposium Proc.*  
 Burger-Scheidlin C., et al. 2024, *A&A*, 684, A150  
 Filipovic, M. D. et al. 2023, *Astron. J.*, 166, 4  
 Green, D. A. 2019, *A&A*, 40, 36  
 Planck Collaboration, Adam, R., Ade, P. A. R., et al. 2016, *A&A*, 594, A10  
 Wood, M. et al. 2017, 35th ICRC Proc., Vol. 301, 824  
 Zabalza, V. 2015, 34th ICRC Proc., 922

## ACROSS THE TYPE IA SUPERNOVA-VERSE: FROM TYPE IA SUPERNOVA REMNANTS TO BINARY LOVE STORIES IN THEIR PREVIOUS LIFE

Chuan-Jui Li<sup>1</sup>(李傳睿) and You-Hua Chu<sup>1,2</sup>(朱有花)

### RESUMEN

Las supernovas de tipo Ia (SNe Ia) se han utilizado como candelas estándar para descubrir la expansión acelerada del universo, lo que llevó a la revelación de la energía oscura y a la concesión del Premio Nobel de Física de 2011 a los astrónomos. Por importantes que sean, las SNe Ia no se comprenden completamente. Todavía discutimos sobre cómo explotan. No está claro si se originan a partir de: (1) un origen degenerado simple (SD) en el que las enanas blancas acretan de estrellas binarias compañeras o (2) un origen degenerado doble (DD) que resulta de la fusión de dos enanas blancas. Para investigar la naturaleza de SNe Ia, buscamos pistas sobre su vida anterior en los restos de explosiones, llamados remanentes de supernova (SNR). Si se detecta un compañero superviviente o un medio circumestelar denso debido a la pérdida de masa del progenitor, se puede afirmar el origen de la SD. Durante las últimas décadas, no se ha encontrado de manera inequívoca en la Vía Láctea ningún compañero superviviente dentro de las SNR Ia. Por lo tanto, decidimos ampliar los límites hacia otras galaxias. Utilizando imágenes y espectros de estrellas y gas ionizado, encontramos que el origen SD de SNe Ia podría ser más frecuente de lo que se pensaba anteriormente.

### ABSTRACT

Type Ia supernovae (SNe Ia) have been used as standard candles to discover the accelerating expansion of the universe, leading to the revelation of dark energy and the award of 2011 Nobel Prize in Physics to astronomers. Important as they are, SNe Ia are not fully understood. We still argue about how they explode. It is not clear whether they originate from (1) a single-degenerate (SD) origin in which white dwarfs accreting from binary companion stars or (2) a double-degenerate (DD) origin results from mergers of two white dwarfs. To probe the nature of SNe Ia, we search for clues to their previous life in the remains of explosions, called supernova remnants (SNRs). If a surviving companion or a dense circumstellar medium from the progenitor's mass loss is detected, the SD origin can be affirmed. Over the past decades, no surviving companions within SNRs Ia have been unambiguously found in the Milky Way. We thus decided to push the envelope to other galaxies. Using images and spectra of stars and ionized gas, we find that the SD origin for SNe Ia could be more prevalent than people previously thought.

*Key Words:* ISM: individual objects (SNR 0509–67.5, SNR 0519–69.0, SNR 0509–68.7, SNR DEM L71, SNR 0548–70.4)  
— ISM: supernova remnants — Magellanic Clouds

### 1. INTRODUCTION

Type Ia supernovae (SNe Ia) have been used as standardizable candles to discover the accelerated expansion of the universe, leading to the revelation of dark energy and the award of 2011 Nobel Prize in Physics to Saul Perlmutter, Brian Schmidt, and Adam Riess. Important as they are, SNe Ia are not fully understood. People still argue about how they explode.

Generally speaking, two contrasting origins of SNe Ia have been suggested: a *single degenerate (SD)* origin in which a white dwarf accretes material from a non-degenerate normal star companion until its mass nears the Chandrasekhar limit (Whelan & Iben 1973; Nomoto 1982), and a *double degenerate (DD)* origin that results from the merger of two white dwarfs (Iben & Tutukov 1984; Webbink 1984).

It is still debated whether the SD or DD origin is prevalent among SNe Ia. In the SD scenario, the interaction between the white dwarf and the normal star companion strips the mass of the companion to form a circumstellar medium (CSM; Hachisu et al. 2008), and the companion can survive the SN explosion and be detected (Marietta et al. 2000; Pan et

<sup>1</sup>Institute of Astronomy and Astrophysics, Academia Sinica, P.O. Box 23-141, Taipei 10617, Taiwan.

<sup>2</sup>Department of Astronomy, University of Illinois at Urbana-Champaign, 1002 West Green Street, Urbana, IL 61801, U.S.A.

al. 2014). In the DD scenario, both white dwarfs are destroyed and no dense CSM or detectable stellar remnant is expected. Therefore, if a surviving companion or a dense CSM is detected near the explosion center of a Type Ia SN remnant (SNR Ia), the SD origin of this SN can be affirmed (Ruiz-Lapuente 1997; Canal et al. 2001); however, to date, no surviving companion has been unambiguously identified near explosion centers of SNRs Ia, although dense CSM has been detected in some SNRs Ia (see Wang & Han 2012; Maoz et al. 2014; Ruiz-Lapuente 2014; Wang 2018; Ruiz-Lapuente 2019 for reviews).

To probe the nature of SNe Ia’s progenitors, we have chosen the young SNRs Ia in the Large Magellanic Cloud (LMC) because of the known distance, low extinction, and minimal line-of-sight confusion. The young SNRs Ia exhibit shell structures whose optical spectra are dominated by Balmer lines with no or weak forbidden lines, as a result of collisionless shocks advancing into a partially neutral interstellar medium (ISM; Chevalier et al. 1980). The LMC hosts five SNRs Ia containing Balmer-dominated shells: 0509–67.5, 0519–69.0, N103B, DEM L71, and 0548–70.4, as shown in Figure 1. We have been studying these SNRs’ structure and environments and searching for their SN progenitors’ companion stars and the circumstellar medium, as summarized below.

## 2. SEARCH FOR SURVIVING COMPANIONS OF PROGENITORS OF YOUNG LMC SNRS IA

We used two different methods to conduct an extensive search for surviving companions of SN progenitors in all 5 SNRs Ia in the LMC. In the first method, we used the HST photometric measurements of stars to construct color–magnitude diagrams and compared positions of stars in the color–magnitude diagrams with those expected from theoretical post-impact evolution of surviving companions (e.g., Pan et al. 2014). In the second method, we used the Very Large Telescope (VLT) Multi Unit Spectroscopic Explorer (MUSE) observations to carry out spectroscopic analyses of stars in order to use large peculiar radial velocities as diagnostics of surviving companions.

In the SNR 0509–67.5, we found that no stars are near the explosion center and confirmed the absence of a surviving companion (Litke et al. 2017). In the other 4 SNRs Ia, N103B, DEM L71, 0519–69.0, and 0548–70.4, we carried out the photometric and spectroscopic analyses and searched for surviving companions. In addition to the candidate we found in

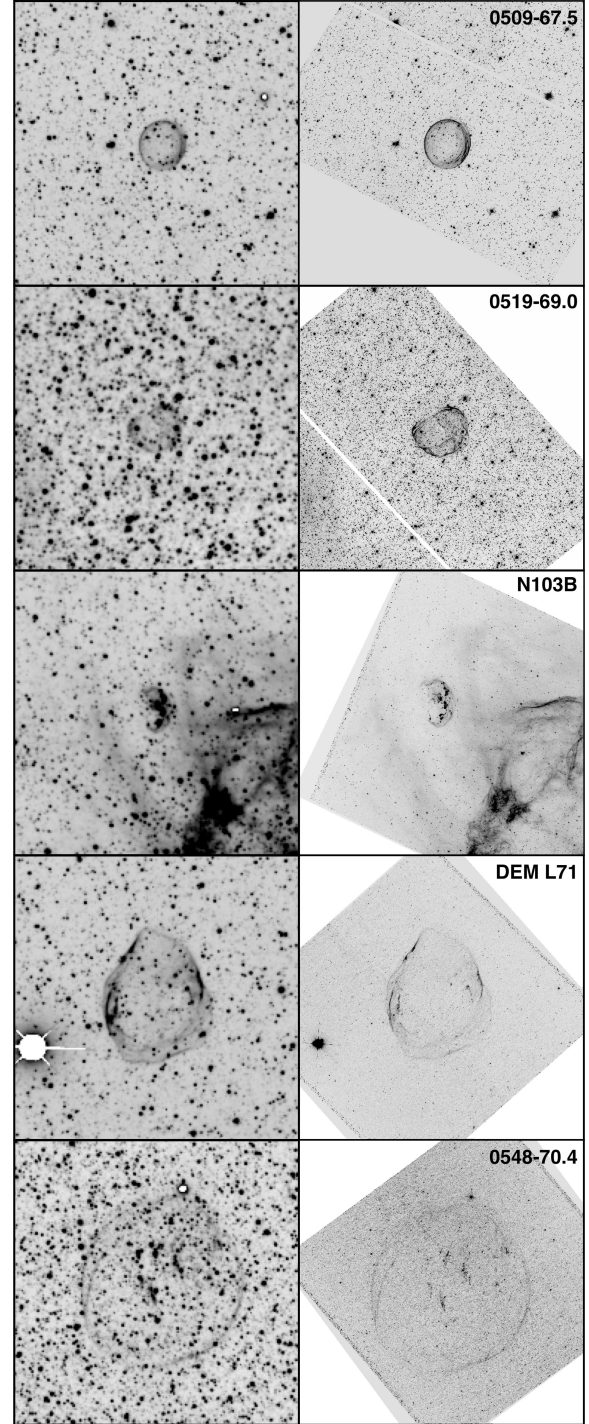


Fig. 1.  $H\alpha$  images of the five LMC SNRs Ia with Balmer-dominated shells (from Li et al. 2021). Left Images were obtained with the MOSAIC II camera on the Blanco 4 m Telescope at Cerro Tololo Inter-American Observatory and right images were taken with the Hubble Space Telescope. The field of view of each panel is  $3' \times 3'$ . North is up and east is left.

N103B (Li et al. 2017), we found a star in 0519–69.0 and a star in DEM L71 with large peculiar radial velocities, making them possible candidates of surviving companions of the SN progenitors (Li et al. 2019). In this work, *we find that 20%–60% of these five young SNRs Ia may originate from SD progenitors, significantly higher than the 20% previously suggested by González Hernández et al. (2012).*

### 2.1. Search for Circumstellar Medium within Young LMC SNRs Ia

SNRs are generally diagnosed by strong [S II]  $\lambda\lambda 6716, 6731$  lines, nonthermal radio emission, and diffuse X-ray emission, which are characteristics produced by fast shocks. However, young SNRs Ia show filamentary shells with optical spectra dominated by Balmer lines without forbidden-line counterparts. The weakness or absence of forbidden lines can be explained by collisionless shocks advancing into a partially neutral medium (Chevalier et al. 1980). In the case of N103B, bright forbidden lines are detected from dense knots that represent the CSM ejected by the progenitor before the SN explosion, implying that the SN progenitor must be of SD origin (Li et al. 2017).

Intrigued by the CSM in N103B, we used VLT MUSE and Advanced Technology Telescope (ATT) Wide Field Integral Spectrograph (WiFeS) observations to search for forbidden-line emission from all five SNRs Ia containing Balmer-dominated shells in the LMC: 0509–67.5, 0519–69.0, N103B, DEM L71 and 0548–70.4. We was pleasantly surprised to find bright forbidden line emission from small dense knots in 4 out of these 5 SNRs. *Dense nebular knots were discovered in 0519–69.0, DEM L71, and 0548–70.4 for the first time!* The electron densities of the dense knots are as high as  $10,000 \text{ H cm}^{-3}$ , suggesting that they originate from a CSM. Thus the presence of CSM in SNRs Ia seems prevalent, and *the physical properties of the CSM evolve along the SNR.*

From this work, we find that 80% of these five young SNRs Ia contain dense CSM and may originate from SD progenitors, consistent with my previous finding based on the search for surviving companions (Li et al. 2019). *These studies indicate that the SD origin for SNe Ia could be more prevalent than people previously thought (Li et al. 2021).*

### 3. SUMMARY

SNe Ia may originate from (1) a SD origin, in which white dwarfs accreting from binary companion stars or (2) a DD origin, that results from mergers of two white dwarfs. If a surviving companion or

a dense circumstellar medium (CSM) from the progenitor’s mass loss is detected, the origin of SD can be affirmed.

To date, no surviving companion has been unambiguously confirmed in the Milky Way. We have thus turned to the five young SNRs Ia in the Large Magellanic Cloud (LMC). We have used HST images to search for surviving companions in these SNRs. We have also used archival VLT MUSE spectra to search for stars with high radial velocities.

From these analyses, we found possible surviving companion candidates of SN progenitors within SNRs Ia outside the Milky Way. We have further used VLT MUSE spectra and HST  $H\alpha$  images of these SNRs to discover forbidden-line-emitting nebular knots with high density that most likely belong to a CSM. We was pleasantly surprised to find that bright forbidden line emission from dense CSM in four of five Type Ia LMC SNRs. The existence of CSM makes physical structures and environments of these SNRs appearing to be complex. The SD origin for SNe Ia could be more prevalent than previously thought.

### REFERENCES

- Canal, R., Méndez, J., & Ruiz-Lapuente, P. 2001, *ApJL*, 550, L53
- Chevalier, R. A., Kirshner, R. P., & Raymond, J. C. 1980, *ApJ*, 235, 186
- Iben, I., Jr., & Tutukov, A. V. 1984
- González Hernández, J. I., Ruiz-Lapuente, P., Tabernero, H. M., et al. 2012, *Nature*, 489, 533
- Hachisu, I., Kato, M., & Nomoto, K. 2008, *ApJ*, 679, 1390-1404
- Li, C.-J., Chu, Y.-H., Gruendl, R. A., et al. 2017, *ApJ*, 836, 85
- Li, C.-J., Kerzendorf, W. E., Chu, Y.-H., et al. 2019, *ApJ*, 886, 99
- Li, C.-J., Chu, Y.-H., Raymond, J. C., et al. 2021, *ApJ*, 923, 141
- Litke, K. C., Chu, Y.-H., Holmes, A., et al. 2017, *ApJ*, 837, 111
- Maoz, D., Mannucci, F., & Nelemans, G. 2014, *ARAA*, 52, 107
- Marietta, E., Burrows, A., & Fryxell, B. 2000, *ApJS*, 128, 615
- Nomoto, K. 1982, *ApJ*, 257, 780
- Pan, K.-C., Ricker, P. M., & Taam, R. E. 2014, *ApJ*, 792, 71
- Ruiz-Lapuente, P. 1997, *Science*, 276, 1813
- Ruiz-Lapuente, P. 2014, *New A Rev*, 62, 15
- Ruiz-Lapuente, P. 2019, *Nature*, 85, 101523
- Wang, B., & Han, Z. 2012, *New A Rev.*, 56, 122
- Wang, B. 2018, *RAA*, 18, 049
- Webbink, R. F. 1984, *ApJ*, 277, 355
- Whelan, J., & Iben, I., Jr. 1973, *ApJ*, 186, 1007

## CONFERENCE SUMMARY: STELLAR FEEDBACK IN THE ISM: CELEBRATING THE LIFE AND WORK OF YOU-HUA CHU(朱有花)

Mordecai-Mark Mac Low<sup>1</sup>

### RESUMEN

En este resumen de la conferencia, primero ofrezco algunas notas históricas sobre mi propia colaboración con You-Hua Chu y sobre el descubrimiento de rayos X de superburbujas por Margarita Rosado S. Luego considero el tema central de la conferencia, la retroalimentación estelar, y cómo las interacciones entre los vientos estelares y el medio interestelar pueden limitar o mejorar los efectos de la retroalimentación en comparación con modelos que incluyen solo explosiones de supernovas. Finalmente, reviso los resultados en otras áreas cubiertas por la conferencia, incluidos los planetas y su formación, los remanentes de novae y supernovas, diferentes temas en la evolución estelar y la interacción con el medio interestelar, los cúmulos estelares, los estudios observacionales y las técnicas numéricas y de observación.

### ABSTRACT

In this conference summary I first provide some historical notes on my own collaboration with You-Hua Chu and on the discovery of X-rays from superbubbles by Margarita Rosado S. I then consider the central subject of the conference, stellar feedback, and how interactions between stellar winds and the interstellar medium can limit or enhance the effects of feedback compared to models including only supernova explosions. Finally, I review results in other areas covered by the conference, including planet and formation, nova and supernova remnants, different topics in stellar evolution and interaction with the interstellar medium, star clusters, observational surveys, and observational and numerical techniques.

*Key Words:* HII regions — ISM: jets and outflows — stars: mass-loss — stars: pre-main-sequence

### 1. HISTORICAL

#### 1.1. *Personal*

I first met You-Hua Chu while I was a graduate student visiting Michael Norman at the National Center for Supercomputing Applications (NCSA) at the University of Illinois in 1987. I listened in to You-Hua and Mike in his office as they considered the consequences of a blast wave running through a clumpy interstellar medium (Norman et al. 1988). I explained to her that I was working on a thesis on the theory of superbubbles. Shortly afterwards, she emailed a series of cogent questions about X-ray emission from superbubbles, which my thesis advisor Dick McCray strongly suggested I engage with. That was excellent advice that led to our description of X-ray emission from superbubbles in the Large Milky (Oey and others' suggested decolonial renaming from Magellanic) Cloud (LMC; Chu & Mac Low 1990) using the *Einstein* data taken by Rosado and described in the next section. Our collaboration was a major factor in my early career, leading to seven papers together.

We also collaborated in advising students, all of whom have contributed to this conference. The first was Guillermo Garcia-Segura, who after an initial observational paper, turned out to be a theorist whose work on the structure of bubbles in time-varying stellar winds has stood the test of time. The second was Sean Points, who was most certainly not a theorist, but has had a distinguished career supporting CTIO and surveying the Magellanic Clouds. Finally came Chao-Chin Yang, who led our demonstration that Toomre gravitational instability of stars and gas can explain the locations of star formation in the LMC (Yang et al. 2007). He then joined my group and moved from working on galactic disks to working on protostellar disks and planet formation, where he continues to have a substantial impact.

#### 1.2. *X-ray Observations of Superbubbles*

Margarita Rosado Solís contributed a history of how the first X-ray observations of superbubbles came to be, which I include here.

Most of you do not know but I have the honor of having contributed with my

<sup>1</sup>Department of Astrophysics, American Museum of Natural History, 200 Central Park West, New York, NY 10024, USA (mordecai@amnh.org).

small grain of sand to the discovery of X-ray emission from superbubbles. I was a PhD student when my observing proposal with the Einstein Satellite of deep exposures of several superbubbles in the LMC including the superbubbles N70 and N185 was accepted. Indeed, at that time I have just measured the high expansion velocities of N7 and N185 by means of Fabry-Perot interferometry (about 70 km/s) and I have computed the X-ray luminosities submitting a proposal to the Einstein Observatory together with my adviser Guy Monnet. The Rosado & Monnet proposal was accepted by Einstein Observatory board and the observations carried out giving the result of the detection, for the first time, of X-ray emission from the superbubbles N70 and N185, among other superbubbles.

We submitted an article reporting those successful results that was rejected by an anonymous referee that argued that it was only noise (at that time the Einstein Observatory instrumental function was concealed for alien users as me, so that it was really hard to answer to the aggressive referee). Years after, our observations were used by You-Hua Chu and Mordecai Mac Low showing that indeed there was X-ray emission from those superbubbles. In fact, bubbles and superbubbles were unexpected objects that successfully emit in X-rays besides the binary compact X-ray sources. Thanks to that observing proposal the X-ray emission from superbubbles started to be studied from the X-ray observatories.

## 2. STELLAR FEEDBACK

Stellar feedback is required to understand galaxy evolution, as Pittard summarized in his talk (i.e. Dalla Vecchia & Schaye 2008). Without including effective stellar feedback, galaxy models form objects far smaller and denser than observed. In this section I summarize how our understanding of this process was advanced during the conference.

The initial focus of stellar feedback modeling was momentum and energy transfer from supernovae (SNe). The momentum injection from SNe in a uniform medium is well understood (e.g. Pittard 2019). However, the consequences of an inhomogeneous medium remain controversial, with Martizzi et al. (2015) and Zhang & Chevalier (2019) finding a 30% reduction in momentum injection, while Kim &

Ostriker (2015) and Walch et al. (2015) find no reduction. Numerical algorithms for adding SN feedback have tended to fail at the numerical resolutions practical for whole galaxy or cosmological models. Only recently have examples been described of apparently resolution-independent algorithms such as FIRE-2 (Hopkins et al. 2018).

However, the story is likely to be more complicated than that for several reasons. First, Pittard noted that it is likely that not all massive stars explode as SNe. Smartt (2015) found that no star with an initial mass exceeding  $20 M_{\odot}$  has been observed to explode. Models by Sukhbold et al. (2016) indeed suggest that direct collapse dominates the outcomes for stars greater than that mass, and even isolated masses down to as low as  $15 M_{\odot}$ . Oey noted that several groups have found that low-metallicity stars have a lower threshold for direct collapse (Heger et al. 2003; Zhang et al. 2008; O'Connor & Ott 2011; Sukhbold et al. 2016). Second, Oey also noted that there can be a several megayear delay before SNe begin. At high densities, neglecting other forms of stellar feedback such as stellar winds can lead to dramatically higher star formation efficiency (SFE). However, stellar winds can be an order of magnitude weaker for substantially subsolar luminosities (Jecmen & Oey 2023).

A further puzzle is that observed stellar wind bubbles often appear to expand too slowly and have too little X-ray emission compared to what would be expected from the Weaver et al. (1977) dynamical model. Chu gave an example from Nazé et al. (2001), showing a 15 pc bubble expanding at only  $15\text{--}20 \text{ km s}^{-1}$ . Oey reviewed the idea that catastrophic cooling of the hot shocked wind region in the interior can shift the solution from the energy conserving solution (Pikel'Ner 1968; Avedisova 1972; Castor et al. 1975; Dyson 1975; Weaver et al. 1977) to the momentum-conserving solution (Steigman et al. 1975). This likely happens in superbubbles as well. The example of N79 in the LMC was described by Rodriguez, presenting results in preparation by Webb & Rodriguez. They find that the diffuse X-ray emission from this super star cluster is an order of magnitude below that predicted by Weaver et al. (1977) or Chu & Mac Low (1990). Further examples of this phenomenon given by Oey include Saken et al. (1992); Brown et al. (1995); Oey (1996); Oey & Kennicutt (1998); Cooper et al. (2004); Smith et al. (2005) and Oey et al. (2009). Pittard summarized models of efficiently cooling bubbles, primarily due to turbulent mixing at the interface between hot and cold gas (Rogers & Pittard 2013; Geen et al. 2015;

Haid et al. 2018; Lancaster et al. 2021). An analytical model of a leaky bubble is an alternative (Harper-Clark & Murray 2009), although that presupposes a lower-density region to leak into, which isn't necessarily available.

Oey argued that at low metallicity, super star clusters fail to effectively drive winds at early times because of the reduced stellar wind strengths expected. This leads to high-density gas being retained near the clusters (Jecmen & Oey 2023), catastrophic cooling (Silich et al. 2004; Wünsch et al. 2007), and thus insufficient time to launch a superwind (Danekhar et al. 2021). Feedback during this period is then radiation dominated (Freyer et al. 2003; Krumholz et al. 2009; Komarova et al. 2021), leading to higher SFE (Krause et al. 2012; Silich & Tenorio-Tagle 2018), greater gas clumpiness allowing Lyman continuum to escape (Jaskot et al. 2019), and smaller superbubbles. The discovery by a group including You-Hua of diffuse nebular C IV emission around the slowly expanding superbubble Mrk 71 supports this scenario (Oey et al. 2023). Even at solar metallicity, models by Polak et al. (2023) find that centrally-concentrated gas clouds with masses approaching  $10^6 M_{\odot}$  have high SFE and do not effectively drive superwinds for several megayears.

The same physics that is important in determining stellar wind bubble dynamics may also act in planetary nebulae, as reviewed by Guerrero. In a series of papers Toalá & Arthur (2014, 2016, 2018) showed that thin-shell and Rayleigh-Taylor instabilities, along with shadowing of ionizing radiation, would mix the contact discontinuity between hot and cold gas in these systems as well, reducing X-ray emission compared to pure thermal conduction. This has been associated with an observed increase in intermediate ions such as NV at the discontinuity (Fang et al. 2016), and, as Richer pointed out, in broadening of UV lines reaching 5–20 km s<sup>-1</sup>.

Wang noted that observational constraint of these mixing models can be achieved using thermal plasma models of X-ray spectra that include charge exchange (Zhang et al. 2014). Because charge exchange is proportional to the ion flux into the contact discontinuity, it can constrain the product of the flow speed and the effective interface area produced by mixing.

### 3. COFFEE BREAK

Coffee breaks at the IA-UNAM in Ensenada had a spectacular view, as shown in Figure 1.

## 4. SHINY RESULTS

In this section I pick out results reported at the conference that I judged to be of particular interest, but do not follow a single theme.

### 4.1. Planet Formation

Recent observations with the Atacama Large Millimeter/submillimeter Array (ALMA) have dramatically sharpened our view of the early stages of disk formation. This period increasingly looks likely to be the crucial period for planet formation. Two major surveys have shown stark differences in the appearance that disks show over the first few megayears of their lives. The eDISK survey (Ohashi et al. 2023) focused on class 0 disks shows rather uniform disks, while the DSHARP survey (Andrews et al. 2018) focused on class I and II disks famously shows a wide variety of rings, spirals, gaps, and other structures. The jury is still out on whether the lack of structure at early times is an optical depth effect—earlier, more massive disks might be too optically thick to show midplane structure—or whether the development of disk structure correlates with the growth of gas giant planets. This is, of course, complicated by the argument on whether disk structures are actually caused by planet formation or other mechanisms, as only two planets, PDS 70b and PDS 70c, have actually been observed in a disk with a gap (e.g. Benisty et al. 2021).

An alternative proposal for producing structure in observed dust disks is the impact of non-uniform accretion onto disks. Segura-Cox reviewed observational evidence for streamers of gas accreting onto protoplanetary disks (ALMA Partnership et al. 2015; Segura-Cox et al. 2020; Garufi et al. 2022; Flores et al. 2023). Kuznetsova et al. (2022) has made the argument that the impact of streamers on disks forms pressure bumps that can trap gas, providing both a promising site for rapid planet formation and an alternative explanation for the formation of the observed ring structures.

Once disks form, dust settles to the midplane, where it begins to coagulate into grains that can grow large enough to start decoupling from the gas. When stopping times grow towards orbital time scales (Stokes number approaches unity), streaming instability sets in, gathering particles into dense clumps that can become self-gravitating. Yang reviewed high-resolution models (Yang & Johansen 2014; Schäfer et al. 2017) of the streaming instability that show a remarkable resemblance to the size distribution of the cold, classical Kuiper Belt observed by Kavelaars et al. (2021). This region of the Kuiper



Fig. 1. View from coffee break at IA-UNAM Ensenada.

Belt is sufficiently low density that the objects are expected to retain their primordial size distribution, making it an excellent laboratory for study of planetesimal formation.

#### 4.2. Star Formation

Two models for star cluster formation were discussed. Grebel reviewed simulations showing that collisions of discrete spherical clouds with different masses in the interstellar medium produce characteristic U-shaped clouds with cavities morphologically similar to observed H II regions such as RCW 120, S44, or S36. However, Arthur's talk showed that the champagne flow morphology characteristic of massive star formation in a region with a density gradient equally well describes these regions. Vázquez-Semadeni argued that global hierarchical collapse in a turbulent interstellar medium better describes the star formation process. Turbulent flows produce a continuous density distribution poorly described by isolated, discrete clouds, but easily leading to the

density gradients needed to produce U-shaped bubbles.

Another issue discussed was the structure of the magnetic fields that can prevent or allow gravitational collapse and star formation. On the scale of a filament dozens of parsecs long, Stephens showed a magnetic polarization map revealing that although the field lies predominantly perpendicular to the filament, there are also multiple regions where it is parallel. This suggests that although the field is important to shaping the flow, it does not always dominate. Looney used ALMA 870  $\mu\text{m}$  polarization to demonstrate grain alignment in the disk of HL Tau (Stephens et al. 2023), presumably by the local field in the disk. Sharma compared polarization measurements towards the outflow and envelope around HD 200775 taken with Planck and AIMPOL in India, showing how the low-resolution, large-scale Planck results average over the small-scale structure in the region.

### 4.3. *Nova and Supernova Remnants*

Orozco-Duarte reviewed the varied morphology of SN remnants, and compared them to simulations of three typical scenarios: an explosion within a bow shock produced by a star moving supersonically with respect to the surrounding medium, a explosion within a star's (spherically symmetric) birth cloud, and an explosion near the edge of a filament an order of magnitude denser than the surrounding medium, which allow reproduction of many observed SN morphologies. Orozco-Duarte et al. (2023) showed that a superbubble in the filament scenario will have off-center SN explosions that cleanly explain the observed soft X-ray luminosity, supporting the hypothesis originally proposed by Chu & Mac Low (1990).

Santamaria and collaborators had a poster showing a morphological catalog of nova remnants. The frequent occurrence of fragmented shells is striking. Toraskar et al. (2013) used simulations to demonstrate that this is exactly the morphology expected from repeating nova explosions separated by periods of hibernation.

A three-dimensional model of the Gemini-Monoceros X-ray enhancement using eROSITA data (Knies et al. 2024) was reviewed by Sasaki. Rather than the usual conclusion that there are two overlapping remnants in the region, they found a total of four objects overlapping in various ways.

The magnetic field in the region behind a SN blast wave was also reviewed by Sasaki. Evolving small scale structure oriented perpendicularly to the blast wave was identified by Matsuda et al. (2020).

Type Ia remnants were considered by several speakers. Pan showed the effects of Type Ia ejecta hitting companion stars (Pan et al. 2012), while Chuan-Jui Li showed the effect of circumstellar medium around Type Ia SNe on their remnants. Li et al. (2021) showed evidence that the presence of circumstellar medium could be more common than expected, and derived an evolutionary sequence for these remnants.

## 4.4. *Stars in all their variety*

### 4.4.1. *Moving Stars*

Arthur and Mackey both emphasized that stars with strong stellar winds moving through the ISM produce distinctive bow shocks (van Buren & Mac Low 1992) and bow waves (Henney & Arthur 2019a,b,c). These can include wind bow shocks such as NGC 7635 (Green et al. 2019) or  $\zeta$  Oph (Toalá & Arthur 2016; Green et al. 2019), bow waves such as the boundary of the heliosphere, dust waves, and radiation bow shocks. Wind bow shocks around stars

with fast enough winds can even be detected in the X-ray (Toalá & Arthur 2016; Green et al. 2022). Orozco-Duarte showed the consequences of an SN explosion within a bow shock (Orozco-Duarte et al. 2023).

### 4.4.2. *Very Massive Stars*

The hunt for very massive stars with masses well above  $100 M_{\odot}$  has extended for decades. The bright spot R136 at the center of You-Hua's favorite H II region, 30 Doradus, was already hypothesized to be a single  $1000 M_{\odot}$  object in the early 1980s. One of her early scientific successes was splitting that spot into multiple components, demonstrating that it is a cluster and not a single star (Chu et al. 1984). However, Smith reviewed the evidence for very massive stars with masses far in excess of  $100 M_{\odot}$  dominating the core of that cluster, most importantly the strong He II emission lines observed there (Crowther et al. 2016). Other super star clusters also show similar emission, arguing that very massive stars are quite generally present in these exceptional objects, even out to high redshift. Wofford also reviewed this evidence in other objects, such as NGC 3125-A1 (Martins & Palacios 2022).

### 4.4.3. *Close Binary Evolution*

There was, of course, extensive discussion of the evolution of close binaries, which can lead to anything from a planetary nebula to a kilonova produced by a neutron star merger. Ricker showed the results of the evolution of a tight binary where mass transfer from the more massive primary to the secondary prior to the SN explosion of the primary results in the secondary evolving faster than it would otherwise, allowing a common envelope to form in the envelope of the secondary encompassing the neutron star remnant of the primary. The end result is a neutron star binary that can merge in a kilonova. Estrada showed that mass transfer from a low mass star onto a compact companion can strip enough mass away to leave a planetary-mass object, which he dubbed a "Chupiter".

Garcia-Segura showed his increasingly detailed models of common envelope evolution that now couple one-dimensional MESA models of post-main sequence stellar evolution to three-dimensional Flash models (begun by Ricker & Taam 2012) and aspherical two-dimensional ZEUS models (Garcia-Segura et al. 2018, 2020, 2021, 2022). The broad variety of planetary nebula morphologies can be captured by this technique to a surprising extent.

Richer studied the velocity gradients and line broadening in planetary nebula shells, showing that

the ordered velocity gradient can not explain the full line widths observed. This suggests that turbulent energy in the shell could be as much as 25% of the thermal energy of the plasma, something not accounted for in previous studies. Weis used similar line observations of AG Carinae to demonstrate that it is not elliptical, but instead bipolar, a morphology that is obscured by its pole-on orientation towards the Earth.

Haberl showed observational evidence that the population of high-mass X-ray binaries correlates well with the star formation rate 25–60 Myr prior in the Small Milky Cloud (Antoniou et al. 2010), but in the LMC correlates with the rate 6–25 Myr prior, and with a formation efficiency 17 times lower in the higher metallicity region (Antoniou & Zezas 2016).

#### 4.5. *Star Clusters*

Stars clearly form in a non-uniform manner. This was classically thought of as occurring in two modes of star formation: clustered and isolated. Grebel emphasized in her review, however, the result of Bressert et al. (2010) that young stellar objects show a continuous Gaussian distribution of surface densities with a peak in the region within 500 pc of the Sun of  $22 \text{ pc}^{-2}$  and a dispersion in the log of the surface density of 0.85. Regions at the high end of this distribution get identified as clusters, but the choice of a cutoff between clustered and isolated star formation is arbitrary.

Similarly, the mass-radius relation of observed clusters appears to show a continuous distribution from open clusters through globular clusters, if one takes into account that young massive clusters can have masses and radii intermediate between open clusters and old globular clusters (Portegies Zwart et al. 2010). The evolution of clusters in the mass-radius plane can be seen in action as recent observations (e.g. Drew et al. 2019; Meingast et al. 2021) show that open clusters are often accompanied by enormous halos of unbound stars of the same age occupying a region as much as an order of magnitude larger than the tidal radius of the central cluster.

#### 4.6. *Surveys*

Multiple observational surveys were reviewed. Rodriguez described the addition of *James Webb Space Telescope* data on 19 spiral galaxies to the PHANGS survey of nearby galaxies at high resolution. Eight infrared bands were imaged with the MIRI and NIRCAM instruments, providing access

to stellar photospheric emission with low obscuration, polycyclic aromatic hydrocarbons, dust continuum, and silicate absorption. Dale showed how the combination of the LEGUS (Calzetti et al. 2015), PHANGS (Lee et al. 2022; Leroy et al. 2021; Emsellem et al. 2022) and GOALS (Armus et al. 2009) surveys shows a relationship between stellar mass and star formation rate spanning five orders of magnitude.

Maschmann used the PHANGS-HST data to study the ages of clusters across the mass-star formation rate plane. Galaxies with high star formation rates compared to the typical value (the so-called main sequence) have plenty of middle-aged clusters, while galaxies with low rates tend to be missing them. (The figure showing this effect was a contender for the most data presented in one figure, as color-color diagrams for every galaxy were presented in a single mass-star formation rate plot.)

Points described the Milky Clouds Emission Line Survey in its most recent version using the Dark Energy Camera. Williams used the Survey to identify a large number of SN remnants across the LMC. Sánchez reviewed the Local Volume Mapper, which uses integral field units the size of the full moon to take spectra at  $30''$  resolution sampling the full sky and densely covering the plane of the Milky Way disk, as well as Orion and the Milky Clouds.

Haberl reviewed the eROSITA all-sky X-ray surveys, the first four of which have been completed, and the fifth of which was truncated by unfortunate geopolitical events, but not before covering the northern half of the LMC. Altogether, some LMC sources have as much as three weeks of observation time. Grishunin reviewed the APEX Legacy LMC CO-line Survey, which gives 5 pc resolution across 85% of the LMC, resolving clouds with masses as low as  $300 M_{\odot}$ .

#### 4.7. *Numerical Techniques*

Several talks emphasized the need to pay close attention to numerical issues to ensure that the physics is being captured. Resolution of physical length scales is a near universal issue. Pittard showed a quantitative criterion for how well the source region for a stellar wind bubble must be resolved to ensure that a bubble forms at all, and further with the correct radial momentum. Mackey showed that increasing the resolution of a bow shock by a factor of four dramatically increases the amount of mass entrained from the contact discontinuity between shocked wind and swept-up ISM by Kelvin-Helmholtz instabilities in the tail of the structure. Mathew checked the

ionization structure of an adiabatic shock across a factor of 10 in linear resolution, finding that 1024 grid points does a very good job.

4.8. *Observational Techniques*

The past and the future of the observation of bubbles and SN remnants was discussed. Toalá reminded us of the dramatic advance in imaging capability represented by the transition from the *Einstein Observatory* to *XMM-Newton* using the example of images of the stellar wind bubble S308. He brought us up to the present day with an infrared spectrum of extraordinary resolution of WR124, taken with the *James Webb Space Telescope* MIRI integral field unit. Then, he compared the *XMM* spectrum of S308 to simulated spectra expected from *XRISM*, *AXIS*, and finally, and most extraordinarily, the exquisite spectrum out to 3 keV expected from the *Athena* WFI.

Long emphasized that *XRISM* will be able to take high-resolution spectra of Galactic SN remnants, while *Athena* will extend that capability to nearby galaxies. These spectra will allow measurement of rarer elements than possible to date, constraining explosion mechanisms. *IXPE* will measure the polarization of Galactic SN remnants, constraining their field structures and thus their particle acceleration properties. Meerkat and upcoming radio telescopes can now image remnants at radio wavelengths with the angular resolution we are accustomed to from optical observatories. This will allow discovery and characterization of remnants in other galaxies.

5. RECOGNITION

The scientific organizing committee of this conference felt that the best recognition we could make of You-Hua Chu’s scientific career was to include her in Wikipedia. The stringent standards currently applied for notability of entries allowed into this encyclopedia indeed show the importance of her career. See [en.wikipedia.org/wiki/You-Hua\\_Chu](https://en.wikipedia.org/wiki/You-Hua_Chu) for the current version of this page. A page has since also been added in simplified Chinese ([zh.wikipedia.org/wiki/%E6%9C%B1%E6%9C%89%E8%8A%B1](https://zh.wikipedia.org/wiki/%E6%9C%B1%E6%9C%89%E8%8A%B1)).

REFERENCES

ALMA Partnership, Brogan, C. L., Pérez, L. M., et al. 2015, *ApJ*, 808, 3  
 Andrews, S. M., Huang, J., Pérez, L. M., et al. 2018, *ApJL*, 869, 41, <https://doi.org/10.3847/2041-8213/aaf741>  
 Antoniou, V. & Zezas, A. 2016, *MNRAS*, 459, 528

Antoniou, V., Zezas, A., Hatzidimitriou, D., & Kalogera, V. 2010, *ApJ*, 716, 140  
 Armus, L., Mazzarella, J. M., Evans, A. S., et al. 2009, *PASP*, 121, 559  
 Avedisova, V. S. 1972, *Soviet Ast.*, 15, 708  
 Benisty, M., Bae, J., Facchini, S., et al. 2021, *ApJ*, 916, 2  
 Bressert, E., Bastian, N., Gutermuth, R., et al. 2010, *MNRAS*, 409, 54  
 Brown, A. G. A., Hartmann, D., & Burton, W. B. 1995, *A&A*, 300, 903  
 Calzetti, D., Lee, J. C., Sabbi, E., et al. 2015, *AJ*, 149, 51  
 Castor, J., McCray, R., & Weaver, R. 1975, *ApJ*, 200, 107  
 Chu, Y. H., Cassinelli, J. P., & Wolfire, M. G. 1984, *ApJ*, 283, 560  
 Chu, Y.-H. & Mac Low, M.-M. 1990, *ApJ*, 365, 510  
 Cooper, R. L., Guerrero, M. A., Chu, Y.-H., Chen, C. H. R., & Dunne, B. C. 2004, *ApJ*, 605, 751  
 Crowther, P. A., Caballero-Nieves, S. M., Bostroem, K. A., et al. 2016, *MNRAS*, 458, 624  
 Dalla Vecchia, C. & Schaye, J. 2008, *MNRAS*, 387, 1431  
 Danehkar, A., Oey, M. S., & Gray, W. J. 2021, *ApJ*, 921, 91  
 Drew, J. E., Monguió, M., & Wright, N. J. 2019, *MNRAS*, 486, 1034  
 Dyson, J. E. 1975, *Ap&SS*, 35, 299  
 Emsellem, E., Schinnerer, E., Santoro, F., et al. 2022, *A&A*, 659, 191  
 Fang, X., Guerrero, M. A., Toalá, J. A., Chu, Y.-H., & Gruendl, R. A. 2016, *ApJ*, 822, 19  
 Flores, C., Ohashi, N., Tobin, J. J., et al. 2023, *ApJ*, 958, 98  
 Freyer, T., Hensler, G., & Yorke, H. W. 2003, *ApJ*, 594, 888  
 Garcia-Segura, G., Ricker, P. M., & Taam, R. E. 2018, *ApJ*, 860, 19  
 Garcia-Segura, G., Taam, R. E., & Ricker, P. M. 2020, *ApJ*, 893, 150  
 \_\_\_\_\_. 2021, *ApJ*, 914, 111  
 \_\_\_\_\_. 2022, *MNRAS*, 517, 3822  
 Garufi, A., Podio, L., Codella, C., et al. 2022, *A&A*, 658, 104  
 Geen, S., Rosdahl, J., Blaizot, J., Devriendt, J., & Slyz, A. 2015, *MNRAS*, 448, 3248  
 Green, S., Mackey, J., Haworth, T. J., Gvaramadze, V. V., & Duffy, P. 2019, *A&A*, 625, 4  
 Green, S., Mackey, J., Kavanagh, P., et al. 2022, *A&A*, 665, 35  
 Haid, S., Walch, S., Seifried, D., Wunsch, R., Dinnbier, F., & Naab, T. 2018, *MNRAS*, 478, 4799  
 Harper-Clark, E. & Murray, N. 2009, *ApJ*, 693, 1696  
 Heger, A., Fryer, C. L., Woosley, S. E., Langer, N., & Hartmann, D. H. 2003, *ApJ*, 591, 288  
 Henney, W. J. & Arthur, S. J. 2019a, *MNRAS*, 486, 3423  
 \_\_\_\_\_. 2019b, *MNRAS*, 486, 4423  
 \_\_\_\_\_. 2019c, *MNRAS*, 489, 2142

- Hopkins, P. F., Wetzell, A., Kereš, D., et al. 2018, *MNRAS*, 480, 800
- Jaskot, A. E., Dowd, T., Oey, M. S., Scarlata, C., & McKinney, J. 2019, *ApJ*, 885, 96
- Jecmen, M. C. & Oey, M. S. 2023, *ApJ*, 958, 149
- Kavalaars, J. J., Petit, J.-M., Gladman, B., et al. 2021, *ApJ*, 920, 28
- Kim, C.-G. & Ostriker, E. C. 2015, *ApJ*, 802, 99
- Knies, J. R., Sasaki, M., Becker, W., et al. 2024, *A&A*, 688, 90
- Komarova, L., Oey, M. S., Krumholz, M. R., et al. 2021, *ApJ*, 920, 46
- Krause, M., Charbonnel, C., Decressin, T., et al. 2012, *A&A*, 546, 5
- Krumholz, M. R., McKee, C. F., & Tumlinson, J. 2009, *ApJ*, 699, 850
- Kuznetsova, A., Bae, J., Hartmann, L., & Low, M.-M. M. 2022, *ApJ*, 928, 92
- Lancaster, L., Ostriker, E. C., Kim, J.-G., & Kim, C.-G. 2021, *ApJ*, 914, 90
- Lee, J. C., Whitmore, B. C., Thilker, D. A., et al. 2022, *ApJS*, 258, 10
- Leroy, A. K., Schinnerer, E., Hughes, A., et al. 2021, *ApJS*, 257, 43
- Li, C.-J., Chu, Y.-H., Raymond, J. C., et al. 2021, *ApJ*, 923, 141
- Martins, F. & Palacios, A. 2022, *A&A*, 659, 163
- Martizzi, D., Faucher-Giguère, C.-A., & Quataert, E. 2015, *MNRAS*, 450, 504
- Matsuda, M., Tanaka, T., Uchida, H., Amano, Y., & Tsuru, T. G. 2020, *PASJ*, 72, 85
- Meingast, S., Alves, J., & Rottensteiner, A. 2021, *A&A*, 645, 84
- Nazé, Y., Chu, Y.-H., Points, S. D., et al. 2001, *AJ*, 122, 921
- Norman, M. L., Dickel, J. R., Livio, M., & Chu, Y. H. 1988, in *Supernova Remnants and the Interstellar Medium: IAU Colloquium 101*, ed. R. S. Roger & T. L. Landecker, (Cambridge: Cambridge U. Press), 222
- O'Connor, E. & Ott, C. D. 2011, *ApJ*, 730, 70
- Oey, M. S. 1996, *ApJ*, 467, 666
- Oey, M. S. & Kennicutt, R. C., J. 1998, *PASA*, 15, 141
- Oey, M. S., Meurer, G. R., Yelda, S., & Furst, E. J. 2009, *Ap&SS*, 324, 205
- Oey, M. S., Sawant, A. N., Danekhar, A., et al. 2023, *ApJ*, 958, 10
- Ohashi, N., Tobin, J. J., Jørgensen, J. K., et al. 2023, *ApJ*, 951, 8, <https://doi.org/10.3847/1538-4357/acd384>
- Orozco-Duarte, R., Garcia-Segura, G., Wofford, A., & Toalá, J. A. 2023, *MNRAS*, 526, 5919
- Pan, K.-C., Ricker, P. M., & Taam, R. E. 2012, *ApJ*, 760, 21
- Pikel'Ner, S. B. 1968, *Astrophys. Lett.*, 2, 97
- Pittard, J. M. 2019, *MNRAS*, 488, 3376
- Polak, B., Mac Low, M.-M., Klessen, R. S., et al. 2023, *arXiv e-prints*, arXiv:2312.06509
- Portegies Zwart, S. F., McMillan, S. L. W., & Gieles, M. 2010, *ARA&A*, 48, 431
- Ricker, P. M. & Taam, R. E. 2012, *ApJ*, 746, 74
- Rogers, H. & Pittard, J. M. 2013, *MNRAS*, 431, 1337
- Saken, J. M., Shull, J. M., Garmany, C. D., Nichols-Bohlin, J., & Fesen, R. A. 1992, *ApJ*, 397, 537
- Schäfer, U., Yang, C.-C., & Johansen, A. 2017, *A&A*, 597, 69
- Segura-Cox, D. M., Schmiedeke, A., Pineda, J. E., et al. 2020, *Natur*, 586, 228
- Silich, S. & Tenorio-Tagle, G. 2018, *MNRAS*, 478, 5112
- Silich, S., Tenorio-Tagle, G., & Rodríguez-González, A. 2004, *ApJ*, 610, 226
- Smartt, S. J. 2015, *PASA*, 32, e016
- Smith, R. K., Edgar, R. J., Plucinsky, P. P., et al. 2005, *ApJ*, 623, 225
- Steigman, G., Strittmatter, P. A., & Williams, R. E. 1975, *ApJ*, 198, 575
- Stephens, I. W., Lin, Z.-Y. D., Fernández-López, M., et al. 2023, *Natur*, 623, 705
- Sukhbold, T., Ertl, T., Woosley, S. E., Brown, J. M., & Janka, H. T. 2016, *ApJ*, 821, 38
- Toalá, J. A. & Arthur, S. J. 2014, *MNRAS*, 443, 3486
- \_\_\_\_\_. 2016, *MNRAS*, 463, 4438
- Toalá, J. A. & Arthur, S. J. 2018, *Galaxies*, 6, 80
- Toraskar, J., Mac Low, M.-M., Shara, M. M., & Zurek, D. R. 2013, *ApJ*, 768, 48
- van Buren, D. & Mac Low, M.-M. 1992, *ApJ*, 394, 534
- Walch, S., Girichidis, P., Naab, T., et al. 2015, *MNRAS*, 454, 238
- Weaver, R., McCray, R., Castor, J., Shapiro, P., & Moore, R. 1977, *ApJ*, 218, 377
- Wünsch, R., Silich, S., Palouš, J., & Tenorio-Tagle, G. 2007, *A&A*, 471, 579
- Yang, C.-C., Gruendl, R. A., Chu, Y.-H., Mac Low, M.-M., & Fukui, Y. 2007, *ApJ*, 671, 374
- Yang, C.-C. & Johansen, A. 2014, *ApJ*, 792, 86
- Zhang, D. & Chevalier, R. A. 2019, *MNRAS*, 482, 1602
- Zhang, S., Wang, Q. D., Ji, L., et al. 2014, *ApJ*, 794, 61
- Zhang, W., Woosley, S. E., & Heger, A. 2008, *ApJ*, 679, 639

## AUTHOR INDEX

- Ambrocio-Cruz, P.** Mixed Morphology Supernova Remnants and the Contribution of Margarita Rosado to the Detection of Extended X-ray Emission from Superbubbles. *M. Rosado, J. Reyes-Iturbide, P. Ambrocio-Cruz, et al.*, 25
- Arias-Montaño, L.** Mixed Morphology Supernova Remnants and the Contribution of Margarita Rosado to the Detection of Extended X-ray Emission from Superbubbles. *M. Rosado, J. Reyes-Iturbide, P. Ambrocio-Cruz, et al.*, 25
- Arthur, S. J.** Stellar Winds from Massive Stars. *S. J. Arthur*, 8
- Beltrán-Sánchez, A. V.** The Extremely Young Planetary Nebula M 3-27. *F. Ruiz-Escobedo, M. Peña, & A. V. Beltrán-Sánchez*, 42
- Blair, W. P.** Supernova Remnant Signatures in Emission-Line Surveys of the Magellanic Clouds with NOIRLab’s DECam. *R. N. M. Williams, S. D. Points, K. S. Long, W. P. Blair, & P. F. Winkler*, 48
- Blair, W. P.** The DECam Magellanic Clouds Emission-Line Surveys. *S. D. Points, K. S. Long, W. P. Blair, et al.*, 45
- Bomans, D. J.** Multi-Wavelength Observations of Galactic Winds. *D. J. Bomans*, 30
- Brose, R.** Detecting  $\gamma$ -Rays from the Ancora Supernova Remnant. *C. Burger-Scheidlin, R. Brose, J. Mackey, et al.*, 51
- Bruzual, G.** Very Massive Stars in NGC 3125-A1 ( $z \sim 0$ ) and CDFS131717 ( $z \sim 3$ ). *A. Wofford, A. Sixtos, G. Bruzual, et al.*, 4
- Burger-Scheidlin, C.** Detecting  $\gamma$ -Rays from the Ancora Supernova Remnant. *C. Burger-Scheidlin, R. Brose, J. Mackey, et al.*, 51
- Charlot, S.** Very Massive Stars in NGC 3125-A1 ( $z \sim 0$ ) and CDFS131717 ( $z \sim 3$ ). *A. Wofford, A. Sixtos, G. Bruzual, et al.*, 4
- Chu, Y.-H.** Across the Type Ia Supernova-Verse: From Type Ia Supernova Remnants to Binary Love Stories in Their Previous Life. *C.-J. Li & Y.-H. Chu*, 54
- Chu, Y.-H.** The DECam Magellanic Clouds Emission-Line Surveys. *S. D. Points, K. S. Long, W. P. Blair, et al.*, 45
- Cullen, F.** Very Massive Stars in NGC 3125-A1 ( $z \sim 0$ ) and CDFS131717 ( $z \sim 3$ ). *A. Wofford, A. Sixtos, G. Bruzual, et al.*, 4
- Dale, D. A.** The Influence of Stellar Clusters on PAHs: The Power of Joint HST/JWST Observations in Nearby Galaxies. *D. A. Dale & PHANGS Team*, 33
- de Oña Wilhelmi, E.** Detecting  $\gamma$ -Rays from the Ancora Supernova Remnant. *C. Burger-Scheidlin, R. Brose, J. Mackey, et al.*, 51
- Falle, S. A. E. G.** Feedback from Massive Star Winds. *J. M. Pittard, M. M. Kupilas, C. J. Wareing, & S. A. E. G. Falle*, 27
- Filipović, M. D.** Detecting  $\gamma$ -Rays from the Ancora Supernova Remnant. *C. Burger-Scheidlin, R. Brose, J. Mackey, et al.*, 51
- Gabbasov, R.** Mixed Morphology Supernova Remnants and the Contribution of Margarita Rosado to the Detection of Extended X-ray Emission from Superbubbles. *M. Rosado, J. Reyes-Iturbide, P. Ambrocio-Cruz, et al.*, 25
- Garcia-Segura, G.** Planetary Nebula in the Binary Era. *G. Garcia-Segura, R. E. Taam, & P. M. Ricker*, 36
- Garcia-Segura, G. M.** Preface. *Jesús Alberto Toalá Sanz, Martín Antonio Guerrero Roncel, and Guillermo Miguel Garcia-Segura*, v
- Goswami, P.** Detecting  $\gamma$ -Rays from the Ancora Supernova Remnant. *C. Burger-Scheidlin, R. Brose, J. Mackey, et al.*, 51
- Guerrero Roncel, M. A.** Preface. *Jesús Alberto Toalá Sanz, Martín Antonio Guerrero Roncel, and Guillermo Miguel Garcia-Segura*, v
- Hernández, S.** Very Massive Stars in NGC 3125-A1 ( $z \sim 0$ ) and CDFS131717 ( $z \sim 3$ ). *A. Wofford, A. Sixtos, G. Bruzual, et al.*, 4
- Kupilas, M. M.** Feedback from Massive Star Winds. *J. M. Pittard, M. M. Kupilas, C. J. Wareing, & S. A. E. G. Falle*, 27
- Li, C.-J.** Across the Type Ia Supernova-Verse: From Type Ia Supernova Remnants to Binary Love Stories in Their Previous Life. *C.-J. Li & Y.-H. Chu*, 54
- Lim, B.** Massive Stars Here and There, Always with Some Impact. *Y. Nazé, B. Lim, & G. Rauw*, 13
- Llamas-Bugarin, A.** Mixed Morphology Supernova Remnants and the Contribution of Margarita Rosado to the Detection of Extended X-ray Emission from Superbubbles. *M. Rosado, J. Reyes-Iturbide, P. Ambrocio-Cruz, et al.*, 25

- Long, K. S.** Supernova Remnant Signatures in Emission-Line Surveys of the Magellanic Clouds with NOIRLab's DECam. *R. N. M. Williams, S. D. Points, K. S. Long, W. P. Blair, & P. F. Winkler*, 48
- Long, K. S.** The DECam Magellanic Clouds Emission-Line Surveys. *S. D. Points, K. S. Long, W. P. Blair, et al.*, 45
- Mac Low, M.-M.** Conference Summary: Stellar Feedback in the ISM: Celebrating the Life and Work of You-Hua Chu. *M.-M. Mac Low*, 57
- Mackey, J.** Detecting  $\gamma$ -Rays from the Ancora Supernova Remnant. *C. Burger-Scheidlin, R. Brose, J. Mackey, et al.*, 51
- Mackey, J.** Implementation of Multi-Ion Chemical Kinetics for Circumstellar Nebulae. *A. Mathew & J. Mackey*, 19
- Mackey, J.** Wind-Blown Nebulae from Massive Stars. *J. Mackey*, 16
- Mathew, A.** Implementation of Multi-Ion Chemical Kinetics for Circumstellar Nebulae. *A. Mathew & J. Mackey*, 19
- Mestre Guillen, E.** Detecting  $\gamma$ -Rays from the Ancora Supernova Remnant. *C. Burger-Scheidlin, R. Brose, J. Mackey, et al.*, 51
- Nazé, Y.** Massive Stars Here and There, Always with Some Impact. *Y. Nazé, B. Lim, & G. Rauw*, 13
- Peña, M.** The Extremely Young Planetary Nebula M3-27. *F. Ruiz-Escobedo, M. Peña, & A. V. Beltrán-Sánchez*, 42
- PHANGS Team** The Influence of Stellar Clusters on PAHs: The Power of Joint HST/JWST Observations in Nearby Galaxies. *D. A. Dale & PHANGS Team*, 33
- Pittard, J. M.** Feedback from Massive Star Winds. *J. M. Pittard, M. M. Kupilas, C. J. Wareing, & S. A. E. G. Falle*, 27
- Points, S. D.** Supernova Remnant Signatures in Emission-Line Surveys of the Magellanic Clouds with NOIRLab's DECam. *R. N. M. Williams, S. D. Points, K. S. Long, W. P. Blair, & P. F. Winkler*, 48
- Points, S. D.** The DECam Magellanic Clouds Emission-Line Surveys. *S. D. Points, K. S. Long, W. P. Blair, et al.*, 45
- Ramirez-Ballinas, I.** Mixed Morphology Supernova Remnants and the Contribution of Margarita Rosado to the Detection of Extended X-ray Emission from Superbubbles. *M. Rosado, J. Reyes-Iturbide, P. Ambrocio-Cruz, et al.*, 25
- Rau, S.-J.** Common Envelope Shaping of Planetary Nebulae. *S.-J. Rau & P. M. Ricker*, 39
- Rauw, G.** Massive Stars Here and There, Always with Some Impact. *Y. Nazé, B. Lim, & G. Rauw*, 13
- Reyes-Iturbide, J.** Mixed Morphology Supernova Remnants and the Contribution of Margarita Rosado to the Detection of Extended X-ray Emission from Superbubbles. *M. Rosado, J. Reyes-Iturbide, P. Ambrocio-Cruz, et al.*, 25
- Ricker, P. M.** Common Envelope Shaping of Planetary Nebulae. *S.-J. Rau & P. M. Ricker*, 39
- Ricker, P. M.** Planetary Nebula in the Binary Era. *G. Garcia-Segura, R. E. Taam, & P. M. Ricker*, 36
- Rosado, M.** Mixed Morphology Supernova Remnants and the Contribution of Margarita Rosado to the Detection of Extended X-ray Emission from Superbubbles. *M. Rosado, J. Reyes-Iturbide, P. Ambrocio-Cruz, et al.*, 25
- Ruiz-Escobedo, F.** The Extremely Young Planetary Nebula M3-27. *F. Ruiz-Escobedo, M. Peña, & A. V. Beltrán-Sánchez*, 42
- Sixtos, A.** Very Massive Stars in NGC 3125-A1 ( $z \sim 0$ ) and CDFS131717 ( $z \sim 3$ ). *A. Wofford, A. Sixtos, G. Bruzual, et al.*, 4
- Smith, L.** Very Massive Stars in NGC 3125-A1 ( $z \sim 0$ ) and CDFS131717 ( $z \sim 3$ ). *A. Wofford, A. Sixtos, G. Bruzual, et al.*, 4
- Sushch, I.** Detecting  $\gamma$ -Rays from the Ancora Supernova Remnant. *C. Burger-Scheidlin, R. Brose, J. Mackey, et al.*, 51
- Taam, R. E.** Planetary Nebula in the Binary Era. *G. Garcia-Segura, R. E. Taam, & P. M. Ricker*, 36
- Toalá Sanz, J. A.** Preface. *Jesús Alberto Toalá Sanz, Martín Antonio Guerrero Roncel, and Guillermo Miguel Garcia-Segura*, v
- Wareing, C. J.** Feedback from Massive Star Winds. *J. M. Pittard, M. M. Kupilas, C. J. Wareing, & S. A. E. G. Falle*, 27
- Weis, K.** Small Bubbles Around Big Stars. *K. Weis*, 22
- Williams, R. M.** The DECam Magellanic Clouds Emission-Line Surveys. *S. D. Points, K. S. Long, W. P. Blair, et al.*, 45
- Williams, R. N. M.** Supernova Remnant Signatures in Emission-Line Surveys of the Magellanic Clouds with NOIRLab's DECam. *R. N. M. Williams, S. D. Points, K. S. Long, W. P. Blair, & P. F. Winkler*, 48
- Winkler, P. F.** Supernova Remnant Signatures in Emission-Line Surveys of the Magellanic Clouds with NOIRLab's DECam. *R. N. M. Williams, S. D. Points, K. S. Long, W. P. Blair, & P. F. Winkler*, 48
- Winkler, P. F.** The DECam Magellanic Clouds Emission-Line Surveys. *S. D. Points, K. S. Long, W. P. Blair, et al.*, 45
- Wofford, A.** Very Massive Stars in NGC 3125-A1 ( $z \sim 0$ ) and CDFS131717 ( $z \sim 3$ ). *A. Wofford, A. Sixtos, G. Bruzual, et al.*, 4
- Yang, C.-C.** Dust-gas Dynamics and Planetesimal Formation in Protoplanetary Disks. *C.-C. Yang*, 1